

FULL-WAVEFORM
INVERSION IN
2D VTI MEDIA

by
Nishant Kamath

© Copyright by Nishant Kamath, 2016

All Rights Reserved

A thesis submitted to the Faculty and the Board of Trustees of the Colorado School of Mines
in partial fulfillment of the requirements for the degree of Doctor of Philosophy (Geophysics).

Golden, Colorado

Date _____

Signed: _____

Nishant Kamath

Signed: _____

Dr. Ilya Tsvankin

Thesis Advisor

Golden, Colorado

Date _____

Signed: _____

Dr. Terence K. Young
Professor and Head
Department of Geophysics

ABSTRACT

Full-waveform inversion (FWI) is a technique designed to produce a high-resolution model of the subsurface by using information contained in entire seismic waveforms. This thesis presents a methodology for FWI in elastic VTI (transversely isotropic with a vertical axis of symmetry) media and discusses synthetic results for heterogeneous VTI models.

First, I develop FWI for multicomponent data from a horizontally layered VTI model. The reflectivity method, which permits computation of only PP reflections or a combination of PP and PSV events, is employed to model the data. The Gauss-Newton technique is used to invert for the interval Thomsen parameters, while keeping the densities fixed at the correct values. Eigenvalue/eigenvector decomposition of the Hessian matrix helps analyze the sensitivity of the objective function to the model parameters. Whereas PP data alone are generally sufficient to constrain all four Thomsen parameters even for conventional spreads, including PS reflections provides better constraints, especially for the deeper part of the model.

Next, I derive the gradients of the FWI objective function with respect to the stiffness coefficients of arbitrarily anisotropic media by employing the adjoint-state method. From these expressions, it is straightforward to compute the gradients for parameters of 2D heterogeneous VTI media. FWI is implemented in the time domain with the steepest-descent method used to iteratively update the model. The algorithm is tested on transmitted multicomponent data generated for Gaussian anomalies in Thomsen parameters embedded in homogeneous VTI media.

To test the sensitivity of the objective function to different model parameters, I derive an analytic expression for the Fréchet kernel of FWI for arbitrary anisotropic symmetry by using the Born approximation and asymptotic Green's functions. The amplitude of the kernel, which represents the radiation pattern of a secondary source (that source describes a perturbation in a model parameter), yields the angle-dependent energy scattered by the perturbation. Then the radiation patterns are obtained for anomalies in VTI parameters embedded in isotropic homogeneous media

and employed to analyze the inversion results for the transmission FWI experiments.

To understand some of the challenges posed by data recorded in surface surveys, I generate the multicomponent wavefield for a model based on a geologic section of the Valhall Field in the North Sea. A multiscale approach is adopted to perform FWI in the time domain. For the available offset range, diving-wave energy illuminates the top 1.5 km of the section, with the updates in the deeper regions due primarily to the reflections. FWI is tested for three model parameterizations and the results are explained in terms of the P- and SV-radiation patterns described above. These parameterizations lead to different trade-offs, and the choice of parameterization for a given data set depends on the recorded offset range, the quality of the initial model, and the parameter that needs to be recovered most accurately.

TABLE OF CONTENTS

ABSTRACT	iii
LIST OF FIGURES	viii
ACKNOWLEDGMENTS	xiv
CHAPTER 1 INTRODUCTION	1
CHAPTER 2 FULL-WAVEFORM INVERSION OF MULTICOMPONENT DATA FOR HORIZONTALLY LAYERED VTI MEDIA	4
2.1 Introduction	5
2.2 Methodology	7
2.2.1 Building the initial model	7
2.2.2 Inversion algorithm	9
2.3 Inversion results	10
2.3.1 Model 1	10
2.3.2 Model 2	18
2.4 Conclusions	22
2.5 Acknowledgments	26
CHAPTER 3 ELASTIC FULL-WAVEFORM INVERSION FOR VTI MEDIA: METHODOLOGY AND SENSITIVITY ANALYSIS	27
3.1 Introduction	27
3.2 Methodology	30
3.2.1 Full-waveform inversion for VTI media	30
3.2.2 Application of the adjoint-state method	30

3.2.3	Radiation patterns for elastic FWI	32
3.3	Analysis of FWI of transmission data	39
3.4	Conclusions	53
3.5	Acknowledgments	57
CHAPTER 4 ELASTIC FULL-WAVEFORM INVERSION FOR A SYNTHETIC VTI MODEL FROM VALHALL FIELD		58
4.1	Introduction	58
4.2	Methodology	60
4.2.1	Inversion methodology	60
4.2.2	Synthetic model and data processing	62
4.3	Numerical tests	66
4.3.1	Parameterization I	66
4.3.2	Parameterization II	72
4.3.3	Parameterization III	75
4.4	Conclusions	80
4.5	Acknowledgments	84
CHAPTER 5 SUMMARY AND FUTURE RECOMMENDATIONS		85
5.1	Summary	85
5.2	Recommendations for future work	86
REFERENCES CITED		89
APPENDIX A - GRADIENT COMPUTATION FOR VTI MEDIA USING THE ADJOINT-STATE METHOD		95
APPENDIX B - SENSITIVITY PATTERNS FOR ELASTIC FWI IN VTI MEDIA		101
APPENDIX C - GRADIENTS FOR DIFFERENT PARAMETERIZATIONS		106

LIST OF FIGURES

Figure 2.1	Three-layer model used in the tests. The parameters of the top isotropic layer are $V_P = 2800$ m/s, $V_S = 1400$ m/s, and $\rho = 1.8$ g/cm ³ . For the VTI layer, $V_{P0} = 3000$ m/s, $V_{S0} = 1632$ m/s, $\epsilon = 0.25$, $\delta = 0.1$, and $\rho = 2.4$ g/cm ³ . For the bottom halfspace, $V_P = 3400$ m/s, $V_S = 1800$ m/s, and $\rho = 3.2$ g/cm ³	10
Figure 2.2	(a) Eigenvalues of the Hessian matrix. (b) Components of the eigenvectors (numbered 1 to 4) associated with the four largest eigenvalues of the Hessian. The input data include PP and PS reflections for the model in Figure 2.1 for $X/Z=1.5$. The superscript (2) denotes the VTI layer and (3) the bottom isotropic halfspace. The thickness of the VTI layer is denoted by D.	12
Figure 2.3	(a) Parameters of the VTI layer (circles) after each iteration of FWI; the actual values are marked by the horizontal dashed lines. The input data include PP reflections for the model in Figure 2.1 for $X/Z=1$. (b) Data misfit computed from equation 2.6 and normalized by the value for the initial model.	14
Figure 2.4	(a) Eigenvalues of the Hessian matrix and (b) the components of the eigenvectors (numbered 1 to 4) associated with the four largest eigenvalues of the Hessian. The input data include PP reflections for the model in Figure 2.1 for $X/Z=1$	16
Figure 2.5	(a) Eigenvalues of the Hessian matrix and (b) the components of the eigenvectors (numbered 1 to 4) associated with the four largest eigenvalues of the Hessian. The input data include PP reflections for the model in Figure 2.1 for $X/Z=2$. The data are contaminated with band-limited (10-25 Hz) random noise; the signal-to-noise ratio is five.	17
Figure 2.6	Parameters of the VTI layer (circles) after each iteration of FWI. The input data include PP reflections for the model in Figure 2.1 for $X/Z=2$. The data are contaminated with band-limited (10-25 Hz) random noise; the signal-to-noise ratio is five.	18
Figure 2.7	Eigenvalues of the Hessian matrices associated with the horizontal displacement component (circles) and the vertical component (diamonds). The input data include PP reflections for the model in Figure 2.1 for $X/Z=1$	19

Figure 2.8	(a) Eigenvalues of the Hessian matrices associated with the horizontal component (circles) and the vertical component (diamonds). (b) Components of the eigenvectors (numbered 1 to 4) associated with the four largest eigenvalues of \mathbf{H}_x . The input data include PP reflections for the model in Figure 2.1 for $X/Z=2$. The data are contaminated with band-limited (10-25 Hz) random noise; the signal-to-noise ratio is five.	20
Figure 2.9	Model with two VTI layers sandwiched between isotropic media. The parameters of layer 1 are $V_P = 2800$ m/s, $V_S = 1400$ m/s, and $\rho = 1.8$ gm/cm ³ ; for layer 2, $V_{P0} = 3000$ m/s, $V_{S0} = 1632$ m/s, $\epsilon = 0.1$, $\delta = -0.05$, and $\rho = 2.1$ gm/cm ³ ; for layer 3, $V_P = 3400$ m/s, $V_S = 1800$ m/s, and $\rho = 2.4$ gm/cm ³ ; for layer 4, $V_{P0} = 3700$ m/s, $V_{S0} = 2000$ m/s, $\epsilon = 0.25$, $\delta = 0.1$, and $\rho = 2.8$ gm/cm ³ ; and for the bottom halfspace, $V_P = 4300$ m/s, $V_S = 2200$ m/s, and $\rho = 3.1$ gm/cm ³	21
Figure 2.10	Parameters of layer 4 from the model in Figure 2.9 after each iteration when inversion is performed using a multiscale approach. The input data include PP and PS reflections; the spreadlength-to-depth ratio for the bottom of the model $X/Z_4 = 1$	21
Figure 2.11	Parameters of (a) layer 2 and (b) layer 4 from the model in Figure 2.9 after each iteration. The input data include PP reflections; the spreadlength-to-depth ratio for the bottom of layer 2 is $X/Z_2 = 2.2$ (for the bottom of the model, $X/Z_4 = 1$). The data are contaminated with band-limited (10-25 Hz) random noise; the signal-to-noise ratio is 14.	23
Figure 2.12	Parameters of (a) layer 2 and (b) layer 4 from the model in Figure 2.9 after each iteration. The input data include PP reflections; the spreadlength-to-depth ratios are $X/Z_2 \approx 4.5$ and $X/Z_4 = 2$. The data are contaminated with band-limited (10-25 Hz) random noise; the signal-to-noise ratio is 14.	24
Figure 3.1	Radiation patterns of the velocities (a) V_{P0} , (b) V_{nmo} , and (c) V_{hor} computed from equations 3.9, 3.11, and 3.12 (respectively) for the P-wavefield. The VTI perturbations are inserted into a homogeneous isotropic background. . . .	35
Figure 3.2	Radiation patterns of the velocities (a) V_{S0} , (b) V_{nmo} , and (c) V_{hor} computed from equations 3.14, 3.15, and 3.16 (respectively) for the S-wavefield. The VTI perturbations are inserted into a homogeneous isotropic background; the ratio $V_{S0}/V_{P0} = 0.5$	35
Figure 3.3	Radiation patterns of the parameters (a) $\ln(1/V_{P0}^2)$, (b) $1 + 2\epsilon$, and (c) $1 + 2\delta$ computed from equations 3.17, 3.19, and 3.20 (respectively) for the P-wavefield.	38

Figure 3.4	Radiation patterns of the parameters (a) $\ln(1/V_{S0}^2)$, (b) $1 + 2\epsilon$, and (c) $1 + 2\delta$ computed from equations 3.22, 3.23, and 3.24 (respectively) for the S-wavefield. The ratio $V_{S0}/V_{P0} = 0.5$	38
Figure 3.5	VTI model with a Gaussian anomaly (standard deviation $\sigma = 300$ m) in the anisotropy parameter ϵ . The background and maximum values of ϵ are 0.1 and 0.142, respectively. The other Thomsen parameters are spatially invariant: $V_{P0} = 3000$ m/s, $V_{S0} = 1500$ m/s, and $\delta = -0.05$. The dots on the left mark the source locations and the vertical line on the right represents an array of receivers placed at each grid point (6.6 m apart). The wavefields are generated by horizontal displacent sources.	39
Figure 3.6	(a) Vertical and (b) horizontal displacements for the model in Figure 3.5 generated by a shot at $z = 1.5$ km.	40
Figure 3.7	Change in the normalized objective function with iterations for the model from Figure 3.5.	40
Figure 3.8	Fractional difference between the estimated and initial (background) parameters (a) V_{P0} and (b) V_{S0} for the model from Figure 3.5. The difference between the estimated and initial parameters (c) ϵ and (d) δ for the same model.	41
Figure 3.9	VTI model with the same parameters as in Figure 3.5, but the source and receiver arrays are extended vertically by 0.6 km and the distance between them is reduced from 3.4 to 1.92 km. The wavefields are generated by horizontal displacment sources.	43
Figure 3.10	Fractional difference between the estimated and initial parameters (a) V_{P0} and (b) V_{S0} for the model from Figure 3.9. The difference between the estimated and initial parameters (c) ϵ and (d) δ for the same model.	44
Figure 3.11	VTI model with a Gaussian anomaly in V_{P0} . The background and maximum values of V_{P0} are 3000 m/s and 3283 m/s, respectively. The other Thomsen parameters are spatially invariant: $V_{S0} = 1500$ m/s, $\delta = -0.05$, and $\epsilon = 0.1$. The wavefields are generated by horizontal displacement sources.	45
Figure 3.12	Fractional difference between the estimated and initial parameters (a) V_{P0} and (b) V_{S0} for the model from Figure 3.11. The difference between the estimated and initial parameters (c) ϵ and (d) δ for the same model.	46
Figure 3.13	VTI model with a Gaussian anomaly in V_{P0} . The source and receiver arrays are horizontal. The wavefields are generated by vertical displacement sources.	47

Figure 3.14	Fractional difference between the estimated and initial parameters (a) V_{P0} and (b) V_{S0} for the model from Figure 3.13. The difference between the estimated and initial parameters (c) ϵ and (d) δ for the same model.	48
Figure 3.15	VTI model with a Gaussian anomaly in V_{S0} . The background and maximum values of V_{S0} are 1500 m/s and 1783 m/s, respectively. The other Thomsen parameters are spatially invariant: $V_{P0} = 3000$ m/s, $\delta = -0.05$, and $\epsilon = 0.1$. The wavefields are generated by vertical displacement sources.	49
Figure 3.16	Fractional difference between the estimated and initial parameters (a) V_{P0} and (b) V_{S0} for the model from Figure 3.15. The difference between the estimated and initial parameters (c) ϵ and (d) δ for the same model.	50
Figure 3.17	Change in the normalized objective function with iterations for the model from Figure 3.11 when the data (a) consist of both the P- and S-wave arrivals and (b) contain only the P-waves.	51
Figure 3.18	Fractional difference between the estimated and initial parameters (a) V_{P0} and (b) V_{S0} for the model from Figure 3.11 when the objective function is calculated using only the P-wave data. The difference between the estimated and initial parameters (c) ϵ and (d) δ for the same model.	52
Figure 3.19	Inversion results obtained with parameterization II. Fractional difference between the estimated and initial parameters (a) V_{P0} and (b) V_{S0} for the model from Figure 3.11. The difference between the estimated and initial parameters (c) ϵ and (d) δ for the same model.	54
Figure 3.20	Change in the normalized objective function with iterations for the model from Figure 3.11. The function is computed using parameterization II.	55
Figure 4.1	Parameters (a) V_{P0} , (b) V_{S0} , (c) ϵ , and (d) δ of a synthetic model based on sections from the Valhall field. The velocities here and in the subsequent plots have units of km/s.	63
Figure 4.2	Fans of rays from sources at (a) $x=0$ km and (b) $x=4.4$ km superimposed on the actual V_{P0} -field.	64
Figure 4.3	Initial model for the velocities (a) V_{P0} , (b) V_{S0} , (c) V_{nmo} , and (d) V_{hor}	65
Figure 4.4	Difference between the actual and initial models: (a) V_{P0} , (b) V_{S0} , (c) V_{nmo} , (d) V_{hor} , (e) ϵ , (f) δ , (g) η	67

Figure 4.5	(a) Horizontal and (b) vertical displacement components of the difference between the observed data and those computed for the initial model in the 0 – 1.5 Hz frequency range. The (c) horizontal and (d) vertical components of the difference between the observed data and those computed for the inverted model. The data are generated by an array of vertical displacement sources.	68
Figure 4.6	(a) Horizontal and (b) vertical displacement components of the difference between the observed data and those computed for the initial model in the 0 – 3 Hz frequency range. The (c) horizontal and (d) vertical components of the difference between the observed data and those computed for the inverted model.	68
Figure 4.7	(a) Horizontal and (b) vertical displacement components of the difference between the observed data and those computed for the initial model in the 0 – 5 Hz frequency range. The (c) horizontal and (d) vertical components of the difference between the observed data and those computed for the inverted model.	68
Figure 4.8	Initial (left column), updated (middle column), and actual (right column) models for FWI performed using parameterization I. (a), (b), (c) correspond to V_{P0} , (d), (e), (f) to V_{S0} , (g), (h), (i) to V_{nmo} and (j), (k), (l) to V_{hor}	69
Figure 4.9	Actual (black), initial (magenta), and inverted (green) velocities for parameterization I: (a) V_{P0} , (b) V_{S0} , (c) V_{nmo} , and (d) V_{hor} . The data were generated by an array of vertical displacement sources. The profiles here and in the subsequent plots are displayed at location $x = 3.5$ km	70
Figure 4.10	(a) P- and (b) SV-wave radiation patterns obtained with parameterization I for reflections from a horizontal interface. The patterns here and in the subsequent plots are computed as functions of the opening angles at the diffractor with the background $V_P/V_S = 2$	70
Figure 4.11	Initial (left column), inverted (middle column), and true (right column) models for FWI performed using parameterization I. (a), (b), (c) correspond to V_{P0} , (d), (e), (f) to V_{S0} , (g), (h), (i) to V_{nmo} and (j), (k), (l) to V_{hor} . The data here and in the subsequent plots are generated by an array of oblique displacement sources.	73
Figure 4.12	Actual (black), initial (magenta), and inverted (green) velocities for parameterization I: (a) V_{P0} , (b) V_{S0} , (c) V_{nmo} , and (d) V_{hor}	74
Figure 4.13	(a) P- and (b) SV-wave radiation patterns obtained with parameterization II for reflections from a horizontal interface.	75

Figure 4.14	Initial (left column), inverted (middle column), and actual (right column) models for FWI performed using parameterization II. (a), (b), (c) correspond to V_{nmo} , (d), (e), (f) to V_{S0} , (g), (h), (i) to η and (j), (k), (l) to δ	76
Figure 4.15	Actual (black), initial (magenta), and inverted (green) parameters for parameterization II: (a) V_{nmo} , (b) V_{S0} , (c) η , and (d) δ	77
Figure 4.16	Actual (black), initial (magenta), and inverted (green) velocities for parameterization II: (a) V_{P0} , (b) V_{S0} , (c) V_{nmo} , and (d) V_{hor}	77
Figure 4.17	Initial (left column), inverted (middle column), and actual (right column) models for FWI performed using parameterization II. (a), (b), (c) correspond to V_{nmo} , (d), (e), (f) to V_{S0} , (g), (h), (i) to η and (j), (k), (l) to δ . The initial δ here is obtained by adding a constant value of 0.1 to the δ -field from Figure 4.14(j).	78
Figure 4.18	Actual (black), initial (magenta), and inverted (green) parameters for parameterization II: (a) V_{nmo} , (b) V_{S0} , (c) η , and (d) δ . Inversion is performed for the distorted initial δ from Figure 4.17(j).	79
Figure 4.19	Actual (black), initial (magenta), and inverted (green) velocities for parameterization II: (a) V_{P0} , (b) V_{S0} , (c) V_{nmo} , and (d) V_{hor} . Inversion is performed for the distorted initial δ from Figure 4.17(j).	79
Figure 4.20	(a) P- and (b) SV-wave radiation patterns obtained with parameterization III for reflections from a horizontal interface.	81
Figure 4.21	Initial (left column), inverted (middle column), and actual (right column) models for FWI performed using parameterization III. (a), (b), (c) correspond to V_{hor} , (d), (e), (f) to V_{S0} , (g), (h), (i) to η and (j), (k), (l) to δ	82
Figure 4.22	Actual (black), initial (magenta), and inverted (green) parameters for parameterization III: (a) V_{hor} , (b) V_{S0} , (c) η , and (d) ϵ	83
Figure 4.23	Actual (black), initial (magenta), and inverted (green) velocities for parameterization III: (a) V_{P0} , (b) V_{S0} , (c) V_{nmo} , and (d) V_{hor}	83
Figure B.1	Geometry of the scattering experiment. The source is located at \mathbf{x}_s , the scatterer at \mathbf{x}' , and the receiver at \mathbf{x}_r	101

ACKNOWLEDGMENTS

I am grateful to my advisor, Dr. Ilya Tsvankin, for giving me the opportunity to pursue graduate studies at Mines, and for guiding me throughout the process. He is extremely meticulous in everything he does – from the classes he teaches, to the edits he makes in the papers – and I hope I have picked up some of it.

While I was mesmerized by evanescent waves in Ilya's *Seismology II* course, I found the enthusiasm with which Dave taught *Digital Signals* quite infectious. In Roel's *Art of Science*, we came closest to discussing philosophy in a non-philosophy course, and never before had I understood *migration* until I took Paul's *Imaging* class. Every one of the mathematics courses I took was fun and enlightening: I wish I had taken a few more. Within CWP, John's the veritable math-wiz, who most often has answers to any question related to mathematics; the fact that he taught himself all the math he knows makes it all the more incredible.

The constant love and support of my folks back home kept me going through tricky times. My junior-high English teacher had told me that serious studies begin at the Doctorate level and I now think he was right. Diane, apart from providing immense help with technical writing, made us, especially the international graduate students, feel welcome (and less homesick) by inviting us numerous times for dinners and get togethers at her place; occasions like Thanksgiving and Christmas were just excuses for a group of graduate students to assemble at the Witters-Hicks home to enjoy their hospitality and generosity. My bread-baking skills, I attribute to Diane. Pam and Shingo work so efficiently in the background that one is almost led to believe that annual meetings and updates to the websites happen spontaneously! Thanks to Pam's cakes, we had something to look forward to on Mondays. Lunchtime, with all the debates and arguments about politics, economics and social issues, couldn't be a tenth as much fun without Shingo. Michelle always had answers to any question I could think of, related to Graduate School, at her fingertips. This always saved me a lot of time and effort navigating my way through tonnes of websites or

trying (in vain) to speak with an American accent to an automated questioner on the phone.

Part of the “American experience” I was hoping for was meeting people from all over the world and that is exactly what I achieved. In addition, I had the privilege of working alongside really intelligent people. I received a lot of academic help and advice from students of CWP, both past and contemporary. From amongst the alumni, I would like to thank Andreas, Jyoti and Tariq, and from those who were in part contemporaneous with my stay here, Bharath, Clement, Francesco, Jeff, Mamoru, Simon and Steve. I would specifically like to thank Esteban and Yuting for their immense help, especially with the coding. Satyan, I must admit, has the patience of a saint for tolerating my idiosyncrasies and OC tendencies as an apartment-mate for three excruciating (for him!) years. I reckon I was very fortunate to find people who shared my interests in hiking, running, skiing, travelling, playing tennis, working out, discussing politics and philosophy, and getting an occasional drink. Being part of a committee of culture-vultures, with whom I could spend a weekend evening exploring the theatres, symphonies and restaurants in the Denver area, brought me great joy. For all these, I cannot thank Andrew, Bananeh, Dayna, Farhad, Jieyi, Kanu, Mathias, Michael, Mitra, Nick, Oscar, Tadesse, Vika and Vova enough. Sharing office space with young guns like Aaron, Chris, and Elias made me feel a few years younger.

Finally, a note of thanks to the American Public Library System which gave me (free) access to a treasure trove of books, those constant companions about which Graucho Marx very aptly commented, “Outside of a dog, a book is a man’s best friend. Inside of a dog it’s too dark to read.”

CHAPTER 1

INTRODUCTION

Full-waveform inversion (FWI) is a technique in which seismic waveforms (rather than just traveltimes or amplitudes) are used to invert for properties of the subsurface. Methods like traveltime or reflection tomography yield earth models whose resolution is limited to the first Fresnel zone (Williamson, 1991), whereas one can obtain much higher resolution (on the order of wavelength) by employing FWI (Pratt, 1999). FWI can be carried out in the time or frequency domain. Chapter 2 contains references to literature that discuss time- and frequency-domain FWI algorithms.

The objective function for FWI is typically defined as the least-squares misfit between the modeled and observed data. It is common practice to compute the gradient of the objective function from the adjoint-state method (Lailly, 1983; Tarantola, 1984a) instead of calculating the Fréchet derivatives explicitly, which considerably reduces the computational cost. Various methods are available to update the model iteratively. In the steepest-descent and conjugate-gradient methods, the gradient is not scaled by an inverse Hessian matrix. However, in techniques like BFGS (Broyden-Fletcher-Goldfarb-Shanno) and truncated Newton, an approximate inverse Hessian matrix is applied to the gradient (Virieux and Operto, 2009). Although the computational cost per update is higher in methods employing the Hessian, the convergence is typically much faster.

FWI requires an accurate and smooth initial model which prevents introducing bias in the inversion. A smooth initial model, however, is unable to produce reflections and hence, FWI originally operates with only the first arrivals typically formed by diving waves (Brenders and Pratt, 2007; Pratt, 1999; Shen, 2012). There have been recent efforts to utilize reflections for model updating at later stages of FWI (Wu and Alkhalifah, 2015; Xu et al., 2012; Zhou et al., 2015).

To ensure that the modeled data are not more than half a cycle out of phase with the observed data (i.e., are not cycle-skipped), a multiscale approach (Bunks et al., 1995) is commonly adopted. This approach relies on the availability of low-frequency data with a high signal-to-noise ratio. Performing FWI in a different domain, such as the Laplace-Fourier domain (Shin and Ho Cha, 2009), boosts the signal at low frequencies, thereby mitigating the problem of cycle-skipping. This, in turn, decreases the dependence on the initial model.

Most FWI algorithms employ the acoustic wave equation to model the data and compute the gradient. Even in the case of anisotropic media the acoustic approximation is often used (Gholami et al., 2013a; Plessix and Cao, 2011; Prieux et al., 2011; Warner et al., 2013). When acoustic inversion is performed for land or OBS (Ocean Bottom Sensor) data, the vertical component of the recorded data is typically included in the objective function (Brenders and Pratt, 2007). Modeling acoustic wavefields yields incorrect amplitudes and, does not allow for the estimation of shear-wave velocity. In contrast, simulating elastic wavefields helps properly model amplitudes, account for mode-converted and shear waves, and takes advantage of multicomponent recording. Detailed review of literature on elastic FWI is presented in subsequent chapters.

When inverting for multiple parameters, choosing an appropriate parameterization is very important. Plessix and Cao (2011) perform eigenvalue-eigenvector decomposition of the Hessian matrix to evaluate sensitivity of the objective function to different model parameters. The energy scattered by a perturbation in a model parameter, referred to as the radiation pattern of a secondary source (Alkhalifah and Plessix, 2014; Eaton and Stewart, 1994; Gholami et al., 2013b), also provides a qualitative measure of the sensitivity. Analysis of radiation patterns helps choose an appropriate parameterization based on the offset range of the data, the parameter that needs to be determined with the highest accuracy, and a priori knowledge of the initial model.

In this thesis, I develop FWI of multicomponent data generated for 1D and 2D VTI media. I operate with different sets of model parameters to invert for Thomsen coefficients and I carry out sensitivity analysis for each parameterization.

In Chapter 2, I perform FWI of multicomponent data generated for a horizontally layered VTI model. First, moveout inversion is carried out to build the initial model. The reflectivity method of Mallick and Frazer (1990), used to generate the wavefield, permits computation of either just P-wave data or a combination of PP and PS reflections. Because the number of model parameters is small, it is possible to compute the Fréchet and the Gauss-Newton Hessian matrices and perform sensitivity analysis. FWI is carried out for just PP reflections, as well as the combination of PP and mode-converted data.

Gradient expressions for FWI in arbitrarily anisotropic media are derived in Chapter 3 by using the adjoint-state method (Lailly, 1983; Liu and Tromp, 2006; Plessix, 2006; Tarantola, 1984a). Also, the Born and WKBJ approximations are employed to obtain analytic expressions for P- and SV-wave radiation patterns of parameter-perturbations inserted in a homogeneous isotropic background. Then, I perform FWI for transmission experiments in which Gaussian anomalies in Thomsen parameters are embedded in a homogeneous VTI model. The inversion results are explained in terms of the radiation patterns.

In Chapter 4, a realistic synthetic model, based on a geologic section of the Valhall field, is used to generate multicomponent data. Because diving waves are limited to the top 1.5–2 km of the model, reflection energy is largely responsible for the updates in the deeper regions. Vertical and oblique displacement sources are employed to generate multicomponent data, and FWI is applied for three different model parameterizations. I analyze the results in terms of radiation patterns calculated for reflections from a horizontal interface. Finally, the stability of the algorithm is tested by introducing a large error in the initial δ -model.

CHAPTER 2

FULL-WAVEFORM INVERSION OF MULTICOMPONENT DATA FOR HORIZONTALLY LAYERED VTI MEDIA

Although full-waveform inversion (FWI) has shown significant promise in reconstructing heterogeneous velocity fields, most existing methodologies are limited to acoustic models. We extend FWI to multicomponent (PP and PS) data from anisotropic media, with the current implementation limited to a stack of horizontal, homogeneous VTI (transversely isotropic with a vertical symmetry axis) layers. The algorithm is designed to estimate the interval vertical P- and S-wave velocities (V_{P0} and V_{S0}) and Thomsen parameters ϵ and δ from long-spread PP and PSV reflections. The forward-modeling operator is based on the anisotropic reflectivity technique, and the inversion is performed in the time domain using the gradient (Gauss-Newton) method. We employ nonhyperbolic semblance analysis and Dix-type equations to build the initial model. To identify the medium parameters constrained by the data, we perform eigenvalue/eigenvector decomposition of the approximate Hessian matrix for a VTI layer embedded between isotropic media. Analysis of the eigenvectors shows that the parameters V_{P0} , V_{S0} , ϵ , and δ (density is assumed to be known) can be resolved not only by joint inversion of PP and PS data, but also with PP reflections alone. Although the inversion becomes more stable with increasing spreadlength-to-depth (X/Z) ratio, the parameters of the three-layer model are constrained even by PP data acquired on conventional spreads ($X/Z=1$). For multilayered VTI media, the sensitivity of the objective function to the interval parameters decreases with depth. Still, it is possible to resolve V_{P0} , V_{S0} , ϵ , and δ for the deeper layers using PP-waves, if the ratio X/Z for the bottom of the layer reaches two. Mode-converted waves provide useful additional constraints for FWI, which become essential for smaller spreads. The insights gained here by examining horizontally layered models should help guide the inversion for heterogeneous TI media.

2.1 Introduction

Transversely isotropic media with a vertical axis of symmetry (VTI) can be described by the vertical P- and S-wave velocities, V_{P0} and V_{S0} , and the Thomsen parameters ϵ , δ , and γ . However, traveltimes analysis of PP-wave reflection data typically yields just the P-wave normal-moveout velocity $V_{\text{nmo},P}$ and anellipticity coefficient η (Alkhalifah and Tsvankin, 1995).

Tsvankin and Thomsen (1995) show that all four parameters of horizontally layered VTI media responsible for propagation of P- and SV-waves (V_{P0} , V_{S0} , ϵ , and δ) can be obtained from long-spread PP- and SS(SVSV)-wave traveltimes. Shear waves, however, are not excited in offshore surveys and their quality on land is often unsatisfactory. Therefore, here we consider joint inversion of PP-waves and converted PSV modes (hereafter, denoted by PS; there is no P-to-SH conversion in laterally homogeneous VTI media). The replacement of pure SS reflections with PS-waves, however, complicates velocity analysis because even long-spread traveltimes of PP- and PS-waves are insufficient for constraining the interval parameters V_{P0} , V_{S0} , ϵ , and δ of layer-cake VTI models (Grechka and Tsvankin, 2002).

Here, we examine the feasibility of reconstructing stratified VTI models in depth using full-waveform inversion (FWI) of PP and PS data. FWI can be performed either in the time domain (Bunks et al., 1995; Gauthier, 1986; Kolb et al., 1986; Mora, 1987) or frequency domain (Pratt, 1999; Pratt and Shipp, 1999; Song and Williamson, 1995; Song et al., 1995). It is typically based on gradient estimation by zero-lag crosscorrelation of the source and residual receiver wavefields, as described in Tarantola (1984a). Most existing algorithms are designed for isotropic, acoustic media, and operate primarily with diving waves. Numerical experiments performed by Lee et al. (2010) show that isotropic FWI applied to anisotropic models gives unsatisfactory results. In order to extend FWI to anisotropic media, it is highly beneficial to combine PP-wave data with PS- or SS-waves, which requires employing elastic models. Taking elasticity into account also makes it possible to properly model reflection amplitudes and take advantage of matching the entire waveform rather than just phase information.

Plessix and Rynja (2010) implement FWI for VTI media in the acoustic approximation to invert for $V_{\text{nmo},P}$, η , and δ . Lee et al. (2010) estimate the stiffness coefficients of 2D VTI media by frequency-domain elastic FWI of multicomponent data and conclude that it is difficult to obtain good estimates of the coefficient C_{13} . Parameterization in terms of the stiffnesses, however, is not optimal for inversion purposes (Tsvankin, 2012) and creates trade-offs that can be avoided by using Thomsen (1986) notation. Single- and multiparameter acoustic FWI for VTI media is performed by Gholami et al. (2011). In the former case, they estimate only one velocity (V_{P0} , $V_{\text{nmo},P}$, or the horizontal velocity $V_{\text{hor},P}$), while the long-wavelength variations of ϵ and δ are fixed at the correct values. They also invert for two velocities ($V_{\text{hor},P}$ and V_{P0}) under the assumption that the long-wavelength spatial variation of δ is known. Gholami et al. (2011) conclude that the single-parameter inversion provides a good estimate of the unknown velocity, while multiparameter inversion suffers from nonuniqueness. Plessix and Cao (2011) implement acoustic FWI for diving waves and near-offset reflections to reconstruct the long-wavelength components of the P-wave NMO and horizontal velocities in VTI media.

Chang and McMechan (2009) present a feasibility study of FWI for a horizontal anisotropic layer sandwiched between isotropic media. In addition to TI layers with a vertical (VTI) and horizontal (HTI) symmetry axis, they also consider a layer of orthorhombic symmetry. They use multicomponent data to invert for the vertical P- and S-wave velocities, anisotropy parameters, and density of the anisotropic layer as well as for the parameters of the underlying isotropic halfspace. They conclude that wide-azimuth reflections from both the top and bottom of the anisotropic layer are needed for stable interval parameter estimation.

Here we develop an FWI algorithm for multicomponent data from horizontally layered VTI media. PP and PS reflections from all interfaces are inverted simultaneously, which mitigates downward error propagation through the model. First, we describe application of moveout inversion to building the initial model from just PP-wave moveout or from the combination of PP and PS reflection traveltimes. Then we analyze the Hessian matrix for layered VTI models to identify the parameters constrained by input data acquired for a realistic range of spreadlength-to-depth

(X/Z) ratios. Finally, the inversion algorithm is applied separately to PP data alone and to the combination of PP and PS reflections to evaluate the feasibility of building VTI depth models from different sets of input data.

2.2 Methodology

We model PP- and PS(PSV)-waves excited by a point explosive source with the anisotropic reflectivity method (Mallick and Frazer, 1990) using a Ricker wavelet with a peak frequency of 15 Hz. The data include free-surface multiples but direct arrivals are not modeled. In practice, reflection data are sorted into common-midpoint (CMP) gathers to minimize reflection-point dispersal. However, here FWI operates on a single shot gather because the medium is horizontally layered. Both the horizontal and vertical displacement components are used for inverting PP-waves and the combination of PP and PS data. The algorithm is tested for different spreadlengths with the receiver spacing kept constant at 25 m. The parameters of the first layer (or the overburden) are assumed to be known and are fixed at the correct values during the inversion.

2.2.1 Building the initial model

To obtain the initial model, we employ widely used moveout-inversion techniques. Time processing of PP reflection data in VTI media is fully controlled by the parameters $V_{\text{nmo},P}$ and η , which can be estimated from PP-wave traveltimes:

$$V_{\text{nmo},P} = V_{P0} \sqrt{1 + 2\delta}, \quad (2.1)$$

$$\eta = \frac{\epsilon - \delta}{1 + 2\delta}. \quad (2.2)$$

The long-spread reflection moveout of PP-waves in a horizontal VTI layer is well described by the nonhyperbolic equation of Alkhalifah and Tsvankin (1995):

$$t^2 = t_{P0}^2 + \frac{x^2}{V_{\text{nmo},P}^2} - \frac{2\eta x^4}{V_{\text{nmo},P}^2 [t_{P0}^2 V_{\text{nmo},P}^2 + (1 + 2\eta)x^2]}, \quad (2.3)$$

where x is the offset and t_{P0} is the two-way zero-offset time. The velocity $V_{\text{nmo},P}$ controls the moveout on conventional spreads, while η is responsible for deviation from hyperbolic moveout in long-spread data. In moveout inversion, the parameter η is often replaced with the P-wave horizontal velocity $V_{\text{hor},P} = V_{\text{nmo},P}\sqrt{1 + 2\eta}$.

Equation 2.3 remains valid for layered VTI media, with $V_{\text{nmo},P}$ and η becoming effective quantities for the stack of layers above the reflector. For spreadlength-to-depth ratios X/Z reaching 1.5-2, equation 2.3 can be used to perform 2D semblance scanning and estimate the effective parameters $V_{\text{nmo},P}$ and η (Grechka and Tsvankin, 1998). Then the interval velocity $V_{\text{nmo},P}$ is found from the conventional Dix equation and the interval η from the Dix-type equation given in Grechka and Tsvankin (1998) and Tsvankin (2012). If the offset range is wide enough to record head waves, the interval $V_{\text{hor},P}$ can be estimated directly from the head-wave moveout (Tsvankin, 2012).

The initial value of δ is set to zero, which allows us to find the parameters V_{P0} and ϵ from $V_{\text{nmo},P}$ and η . The density ρ and shear-wave vertical velocity V_{S0} (if only PP data are available) for the initial model are supposed to be found from well logs. Potentially, the accuracy of the initial model can be improved by employing velocity-independent layer stripping (Wang and Tsvankin, 2009).

For multicomponent data, it is necessary to identify the PP and PS (PSV) reflections from the same interfaces (i.e., perform event registration). The interval values of $V_{\text{nmo},P}$ and η can be calculated from P-wave data as described above. To estimate the effective PS-wave NMO velocity ($V_{\text{nmo},PS}$), we apply a 2D semblance scan based on equation 2.3 to long-spread PS data. In this case, η represents just a fitting parameter, but the equation is sufficiently accurate to constrain $V_{\text{nmo},PS}$, which replaces $V_{\text{nmo},P}$ (Xu and Tsvankin, 2008). Then the effective NMO velocity $V_{\text{nmo},SV}$ of the pure SS reflection can be found from (Seriff and Sriram, 1991):

$$2 t_{PS0} V_{\text{nmo},PS}^2 = t_{P0} V_{\text{nmo},P}^2 + t_{S0} V_{\text{nmo},SV}^2, \quad (2.4)$$

where t_{PS0} and t_{S0} are the zero-offset traveltimes of PS- and SS-waves respectively, so that $t_{S0} = 2t_{PS0} - t_{P0}$. The interval SV-wave NMO velocity, obtained from the Dix equation, is given

by:

$$V_{\text{nmo},SV} = V_{S0} \sqrt{1 + 2\sigma}, \quad (2.5)$$

where $\sigma \equiv \left(\frac{V_{P0}}{V_{S0}}\right)^2 (\epsilon - \delta)$.

In principle, all four parameters (V_{P0} , V_{S0} , ϵ , and δ) can be found from $V_{\text{nmo},P}$, $V_{\text{nmo},SV}$, $V_{P0}/V_{S0} = t_{S0}/t_{P0}$, and η . Although this procedure is known to be unstable (Grechka and Tsvankin, 2002), it provides us with an acceptable initial model for FWI.

2.2.2 Inversion algorithm

We perform time-domain inversion of either PP data alone or the combination of PP and PS reflections. The least-squares objective function is defined as:

$$\mathcal{F}(\mathbf{m}) = \frac{1}{2} \|\mathbf{d}_{\text{obs}} - \mathbf{d}_{\text{cal}}(\mathbf{m})\|^2, \quad (2.6)$$

where \mathbf{d}_{obs} is the observed data and $\mathbf{d}_{\text{cal}}(\mathbf{m})$ is the data calculated for a certain model \mathbf{m} . Model updating is carried out via the Gauss-Newton method,

$$(\Delta \mathbf{m}) = [\mathbf{J}^T \mathbf{J}]^{-1} \mathbf{J}^T \Delta \mathbf{d}, \quad (2.7)$$

where \mathbf{J} is the Fréchet derivative matrix obtained by perturbing each model parameter, $\mathbf{J}^T \mathbf{J}$ is the approximate Hessian, and $\Delta \mathbf{d}$ is the difference between the observed data and those computed for a trial model. Forward modeling is carried out with the anisotropic reflectivity algorithm of Mallick and Frazer (1990) mentioned above, based on the formulation introduced by Fryer and Frazer (1984). The main advantage of that method is that it produces the exact 3D reflected wavefield for horizontally layered media including all multiples and mode conversions. In addition, it is possible to separate the wavefield and model either just PP reflections or both PP and mode-converted PS data.

Since the vertical velocities and anisotropy parameters do not have the same units, it is more convenient to invert PP data for the interval parameters V_{P0} , $V_{\text{nmo},P}$, $V_{\text{hor},P}$, V_{P0}/V_{S0} , and the

density ρ . In the case of joint inversion of PP and PS data, we estimate the interval values of V_{P0} , $V_{nmo,P}$, V_{S0} , $V_{nmo,SV}$, and ρ . The initial values of V_{P0} and V_{S0} obtained from PP and PS data can be used to calculate the initial V_{P0}/V_{S0} ratio for the inversion of PP-waves. If only PP reflections are acquired, the initial V_{P0}/V_{S0} has to be known a priori (e.g., from well logs).

2.3 Inversion results

We discuss results obtained for FWI performed on data generated for two horizontally layered models.

2.3.1 Model 1

First, the FWI algorithm is applied to the simple three-layer model in Figure 2.1. The top layer is isotropic, and its velocities and density are assumed to be known. The bottom halfspace is also known to be isotropic, but its parameters are estimated by FWI.

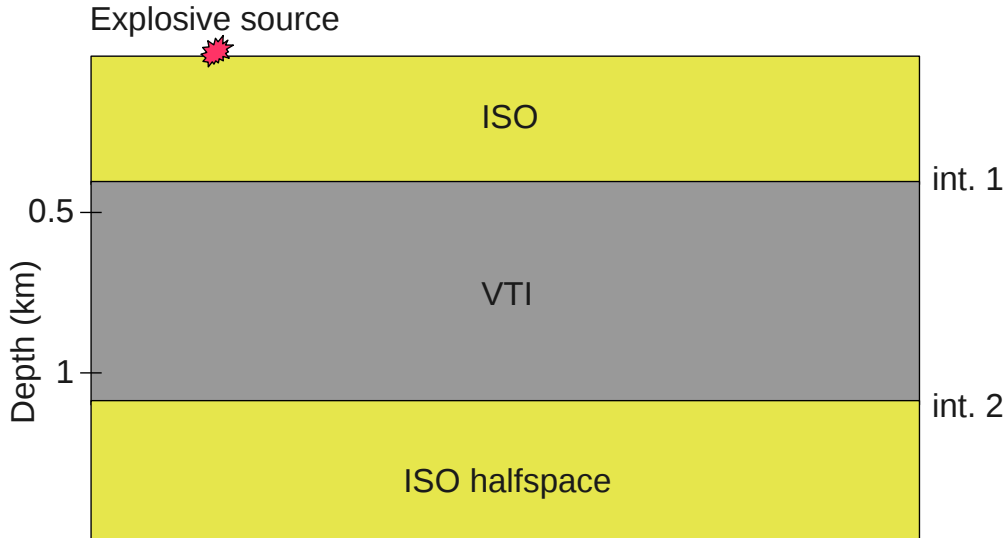


Figure 2.1: Three-layer model used in the tests. The parameters of the top isotropic layer are $V_P = 2800$ m/s, $V_S = 1400$ m/s, and $\rho = 1.8$ g/cm³. For the VTI layer, $V_{P0} = 3000$ m/s, $V_{S0} = 1632$ m/s, $\epsilon = 0.25$, $\delta = 0.1$, and $\rho = 2.4$ g/cm³. For the bottom halfspace, $V_P = 3400$ m/s, $V_S = 1800$ m/s, and $\rho = 3.2$ g/cm³.

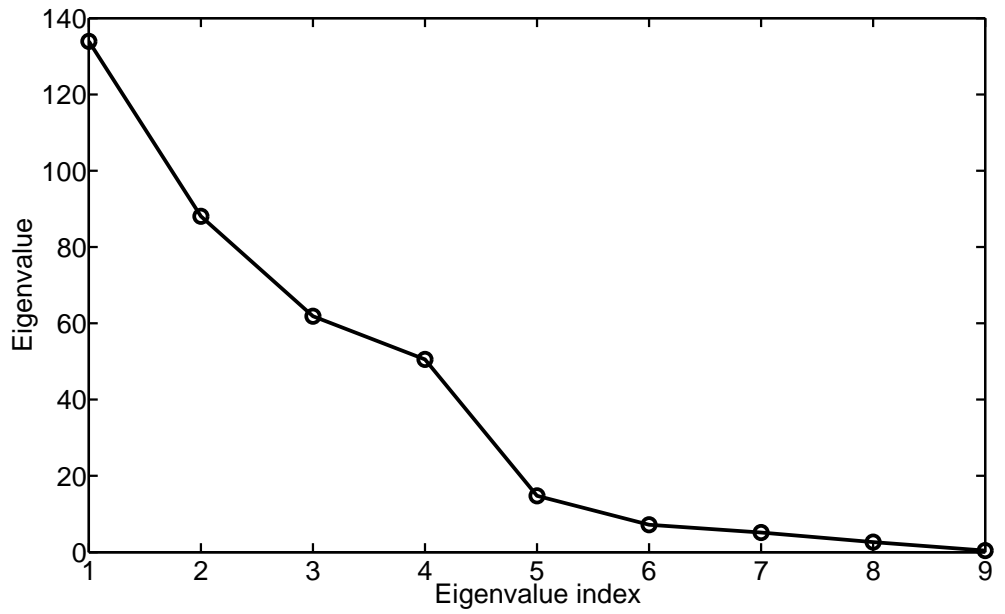
We perform tests for data with the spreadlength-to-depth ratio X/Z ranging from one to three. For $X/Z=1$, the parameter η cannot be constrained by PP reflection traveltimes, so the initial values

of ϵ and δ are set to zero. For larger spreads ($X/Z=1.5, 2, \text{ and } 3$), inversion is performed with the initial parameters computed from moveout inversion as described above.

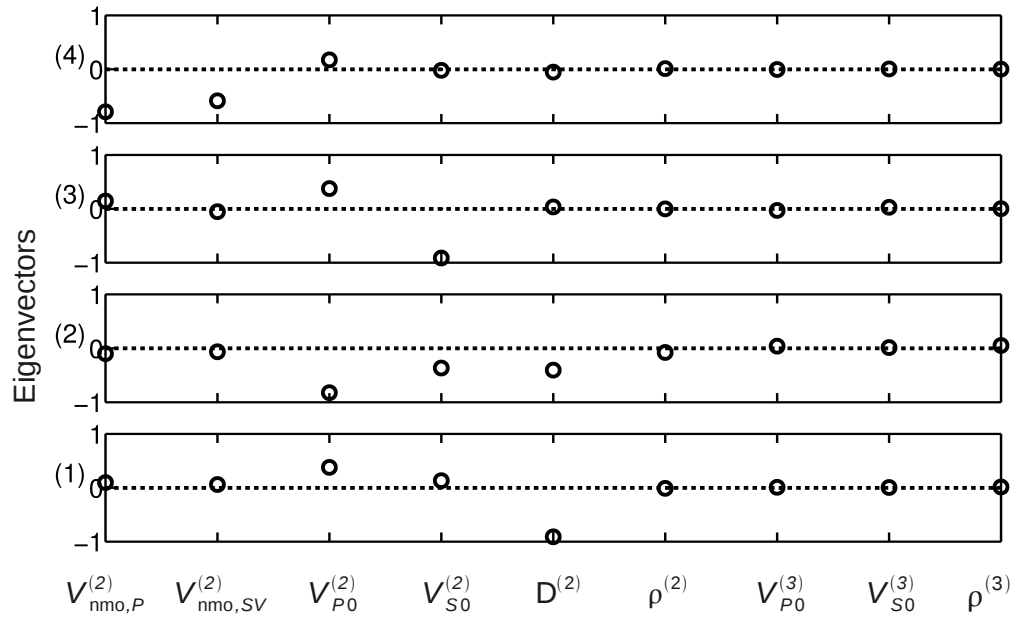
The testing shows that the interval parameters V_{P0} , V_{S0} , ϵ , and δ can be constrained by FWI, but the inversion is highly sensitive to the starting model when the data include both PP and PS reflections. When PP and PS data are inverted jointly with the initial $\delta = 0$, the algorithm converges to the correct values only for $X/Z=1$. For longer spreads, accurate inversion requires calculating the initial δ from moveout inversion, even though errors in δ can reach 0.6. This is likely due to the shape of the objective function, which causes the inversion for the initial $\delta = 0$ to get trapped in local minima. As discussed below, this problem can be mitigated by applying a multiscale approach.

To evaluate the sensitivity of the objective function to the model parameters, we perform the eigenvector/eigenvalue decomposition of the Hessian matrix (Plessix and Cao, 2011) for joint inversion of PP and PS data. Each component of an eigenvector (called the “direction cosine” and represented by the circles in Figure 2.2(b)) indicates the relative sensitivity of the objective function to one of the model parameters. The gradient of the objective function is a linear combination of the eigenvectors weighted by the eigenvalues of the Hessian (Figure 2.2(a)). Figure 2.2(b) displays the eigenvectors associated with the four largest eigenvalues. It shows that the objective function is most sensitive to the layer thickness D (and hence to V_{P0} , since the vertical traveltimes are well constrained), followed by V_{S0} , $V_{\text{mmo},P}$, and $V_{\text{mmo},SV}$.

All our tests demonstrate that the objective function becomes more complicated with the inclusion of density as an unknown parameter, and the search gets trapped in local minima. In spite of the relatively low sensitivity of the objective function to density (Figure 2.2(b)), performing inversion with densities distorted by up to 10% results in unacceptable errors in all inverted parameters. In particular, the velocity V_{P0} and layer thicknesses are off by about 5%. Hence, in all subsequent tests the interval densities are fixed at the correct values. In practice, densities are often estimated from well-log data, whereas in synthetic tests of FWI they are typically fixed at a constant value (e.g., Lee et al., 2010). In principle, density can be better constrained using global optimization



(a)



(b)

Figure 2.2: (a) Eigenvalues of the Hessian matrix. (b) Components of the eigenvectors (numbered 1 to 4) associated with the four largest eigenvalues of the Hessian. The input data include PP and PS reflections for the model in Figure 2.1 for $X/Z=1.5$. The superscript (2) denotes the VTI layer and (3) the bottom isotropic halfspace. The thickness of the VTI layer is denoted by D .

techniques like genetic algorithm (Padhi and Mallick, 2013). For realistic models with a large number of parameters, however, global optimization is extremely expensive.

Next, we generate only PP data for the same model and invert for the parameters V_{P0} , $V_{\text{nmo},P}$, $V_{\text{hor},P}$, and V_{P0}/V_{S0} . For all spreadlengths X/Z , the algorithm converges to the correct parameters, even though the initial value of δ is set to zero. Evidently, the objective function has a simpler shape with fewer local minima, if only PP data are included.

Interestingly, the inversion yields accurate parameter estimates even for $X/Z=1$ despite the absence of PS data (Figure 2.3(a)). This is an unexpected result, especially because such spreadlengths are not sufficient to constrain even the horizontal velocity (or the parameter η) and, therefore, ϵ using reflection traveltimes. The data misfit, normalized by the value at the first iteration, is shown in Figure 2.3(b). Apparently, the success of FWI is ensured by including reflection amplitudes controlled by geometric spreading and reflection coefficient.

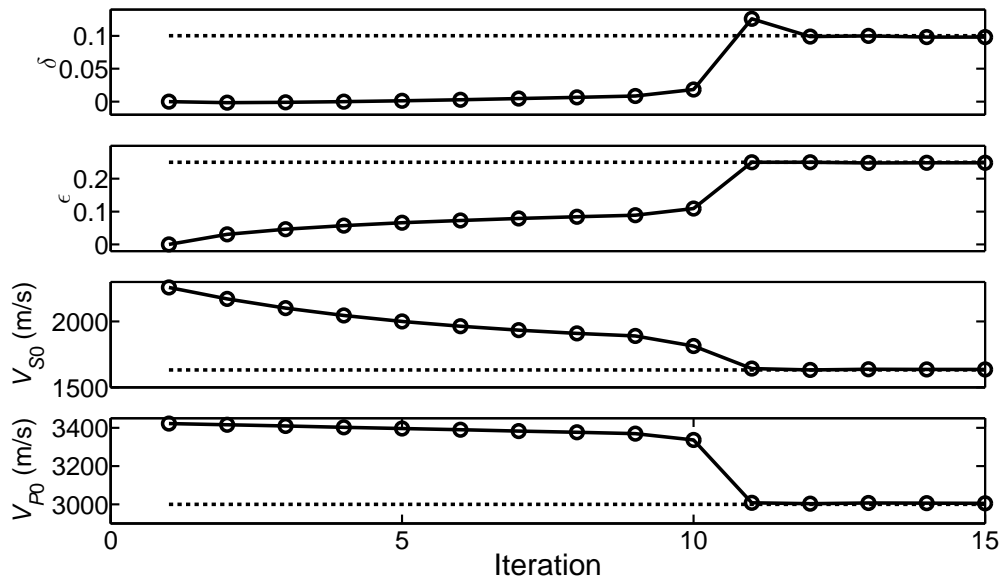
Indeed, angle dependence of the far-field amplitude of P-waves excited by a point explosive source in a homogeneous, weakly anisotropic TI medium is given by (Tsvankin, 1995, 2012; Xu et al., 2005):

$$A_P(\theta) \sim 1 - 2(\epsilon - \delta) \sin^2 2\theta + \delta \sin^2 \theta, \quad (2.8)$$

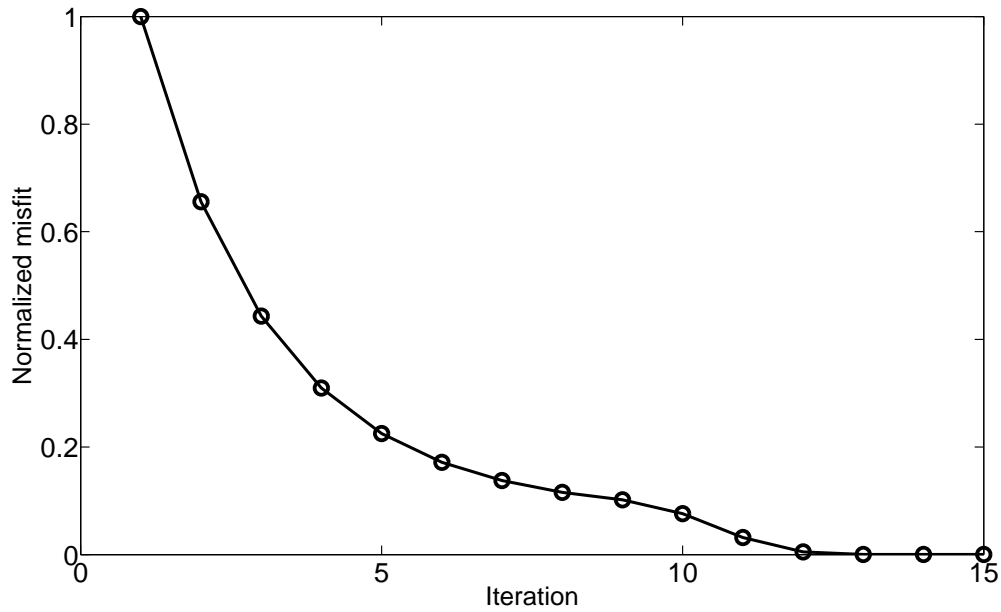
where θ is the phase angle with the symmetry axis. For small angles θ , the amplitude variation (i.e., the anisotropic geometric spreading) is largely controlled by $\eta \approx \epsilon - \delta$. Although equation 2.8 is derived for a homogeneous medium, it also describes the behavior of the anisotropic geometric-spreading factor in any TI layer crossed by the reflected ray (Tsvankin, 2012).

The PP-wave reflection coefficient at a boundary between two VTI halfspaces in the weak-contrast, weak-anisotropy ($|\delta| \ll 1$, $|\epsilon| \ll 1$) approximation is given by (Rüger, 1997, 2002):

$$R = \frac{1}{2} \frac{\Delta Z}{\bar{Z}} + \frac{1}{2} \left[\frac{\Delta V_{P0}}{\bar{V}_{P0}} - \left(\frac{2\bar{V}_{S0}}{\bar{V}_{P0}} \right)^2 \frac{\Delta G}{\bar{G}} + \Delta\delta \right] \sin^2 \theta + \frac{1}{2} \left[\frac{\Delta V_{P0}}{\bar{V}_{P0}} + \Delta\epsilon \right] \sin^2 \theta \tan^2 \theta, \quad (2.9)$$



(a)



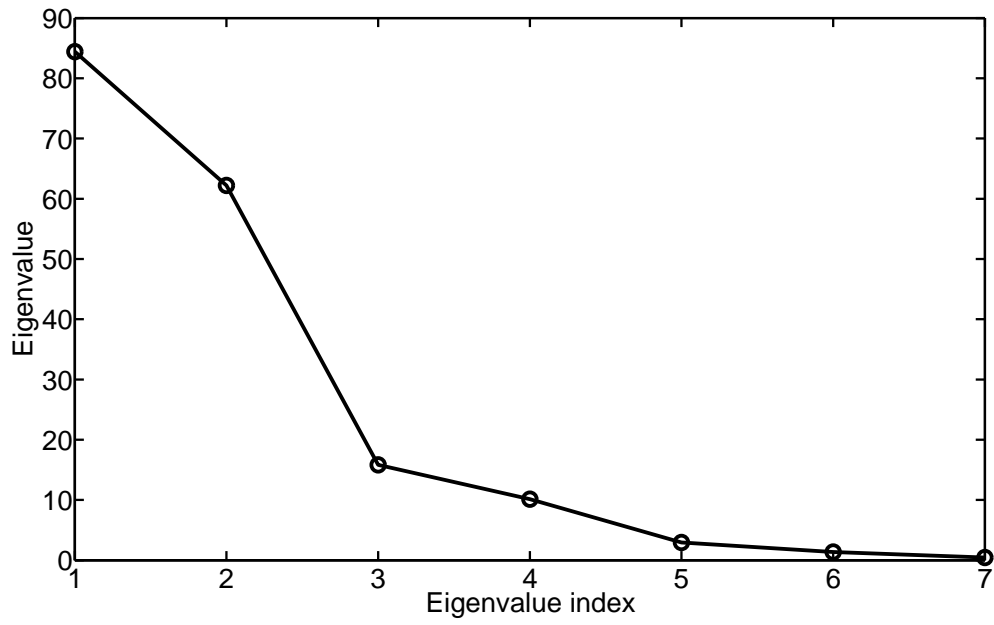
(b)

Figure 2.3: (a) Parameters of the VTI layer (circles) after each iteration of FWI; the actual values are marked by the horizontal dashed lines. The input data include PP reflections for the model in Figure 2.1 for $X/Z=1$. (b) Data misfit computed from equation 2.6 and normalized by the value for the initial model.

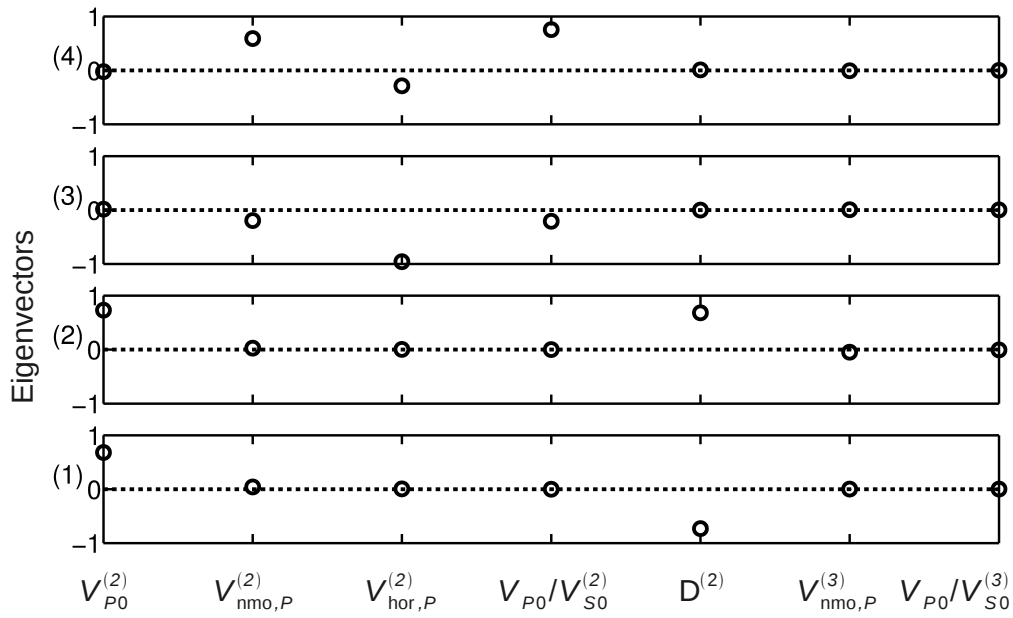
where θ is the incidence phase angle, $Z = \rho V_{P0}$ is the P-wave vertical impedance, and $G = \rho V_{S0}^2$ is the S-wave vertical rigidity modulus. The difference between each parameter B (V_{P0} , V_{S0} , etc.) below and above the reflector is denoted by $\Delta B = B_2 - B_1$, and the average is $\bar{B} = (B_1 + B_2)/2$. The first term in equation 2.9 is the normal-incidence reflection coefficient, also known as the AVO intercept, which is equal to the fractional difference between the P-wave impedances in the two media. The second term is responsible for amplitude variation near the vertical and is called the AVO gradient. It depends on the relative change in V_{P0} and G across the interface and on the contrast in the parameter δ . Hence, PP-wave reflection amplitudes at small offsets are sensitive to the jumps in V_{P0} , V_{S0} , ρ , and δ .

Because the densities in all layers and the velocities in the shallowest layer are fixed at the correct values, the amplitude signatures help resolve all VTI parameters for the model in Figure 2.1. In particular, the normal-incidence reflection coefficient provides constraints on V_{P0} in the VTI layer and the bottom half-space, whereas amplitude variation with angle allows us to estimate the other parameters. Note that the P-wave AVO gradient (and the P-wave reflection coefficient as a whole) includes the jump in the vertical rigidity modulus G (equation 2.9), which creates a dependence of the FWI objective function on V_{S0} . Still, the objective function for PP-wave inversion is not as sensitive to the V_{P0}/V_{S0} ratio as it is to V_{P0} and D (Figure 2.4), partially because the exact P-wave geometric-spreading factor in the $0^\circ - 40^\circ$ range typically changes by less than 2-3% for the V_{P0}/V_{S0} ratio varying from 1.73 to 2.2 (Tsvankin, 2012). We conclude that, FWI of PP reflections can reconstruct the depth scale of this three-layer model even without using long-offset data.

When larger offsets are included, the velocity $V_{\text{hor},P}$ (or η) is well-resolved even in the presence of random noise because it governs the magnitude of nonhyperbolic moveout. Indeed, for $X/Z=2$ the eigenvector associated with the largest eigenvalue of the Hessian points almost entirely in the direction of $V_{\text{hor},P}$ (Figure 2.5(b)). As explained above, the amplitude signatures provide additional information for accurate estimation of the parameters V_{P0} , V_{S0} , ϵ , and δ . In particular, errors in the anisotropy coefficients ϵ and δ do not exceed 0.02.

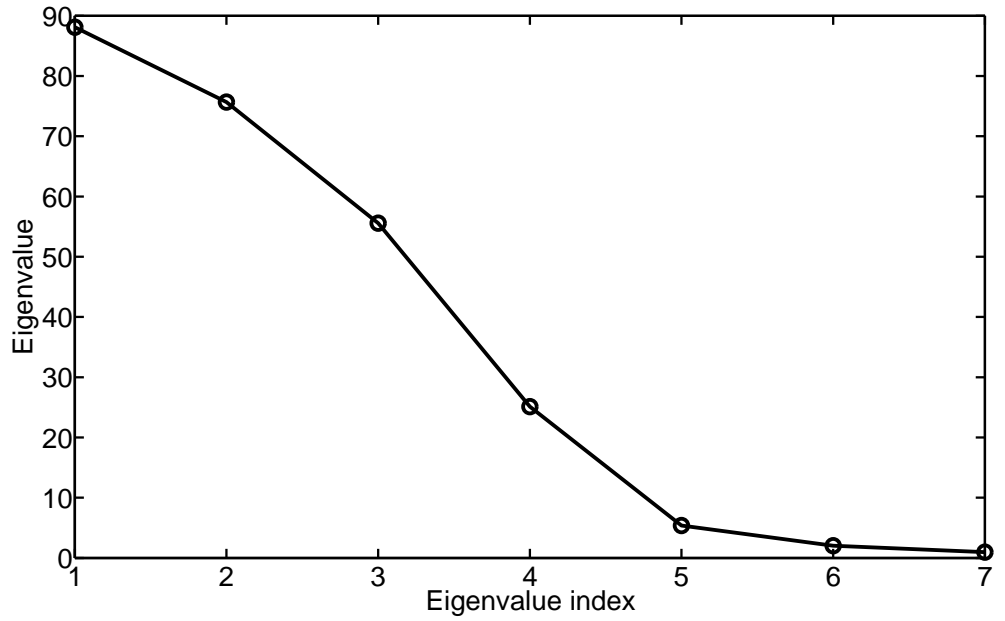


(a)

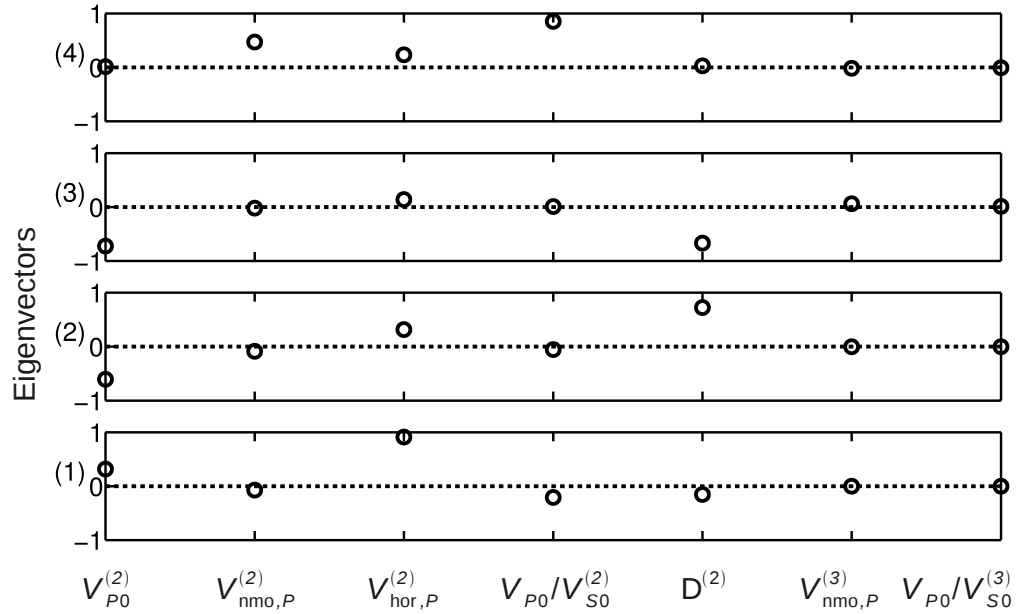


(b)

Figure 2.4: (a) Eigenvalues of the Hessian matrix and (b) the components of the eigenvectors (numbered 1 to 4) associated with the four largest eigenvalues of the Hessian. The input data include PP reflections for the model in Figure 2.1 for $X/Z=1$.



(a)



(b)

Figure 2.5: (a) Eigenvalues of the Hessian matrix and (b) the components of the eigenvectors (numbered 1 to 4) associated with the four largest eigenvalues of the Hessian. The input data include PP reflections for the model in Figure 2.1 for $X/Z=2$. The data are contaminated with band-limited (10-25 Hz) random noise; the signal-to-noise ratio is five.

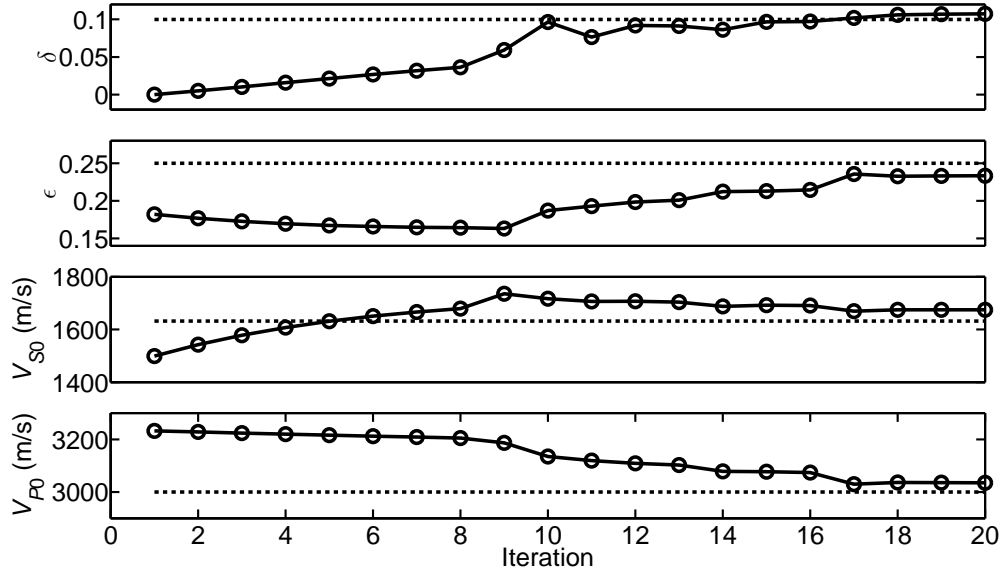


Figure 2.6: Parameters of the VTI layer (circles) after each iteration of FWI. The input data include PP reflections for the model in Figure 2.1 for $X/Z=2$. The data are contaminated with band-limited (10-25 Hz) random noise; the signal-to-noise ratio is five.

In the inversion we assign equal weights to the horizontal and vertical displacement components. For PP-waves recorded on conventional spreads ($X/Z \leq 1.5$), the largest eigenvalues of the Hessian associated with the horizontal component (\mathbf{H}_x) are much smaller than those for the vertical component (\mathbf{H}_z) (Figure 2.7). Hence, as expected, the objective function for PP-wave inversion on conventional spreads is more sensitive to the vertical displacement. However, for a longer spread ($X/Z=2$), the largest eigenvalues of \mathbf{H}_x and \mathbf{H}_z become comparable (Figure 2.8(a)). In addition, the largest eigenvalue of \mathbf{H}_x is three times or more the other eigenvalues, and the corresponding eigenvector points in the direction of $V_{\text{hor},P}$ (Figure 2.8(b)). Therefore, assigning a larger weight to the horizontal component in the objective function for long spreads may result in a faster convergence toward the velocity $V_{\text{hor},P}$.

2.3.2 Model 2

Next, we test the algorithm on PP and PS data for a stratified model that includes two VTI layers (Figure 2.9). Again, the parameters of the top (isotropic) layer are fixed at the correct values, and the bottom half-space is known to be isotropic. As was the case for the first model, convergence of

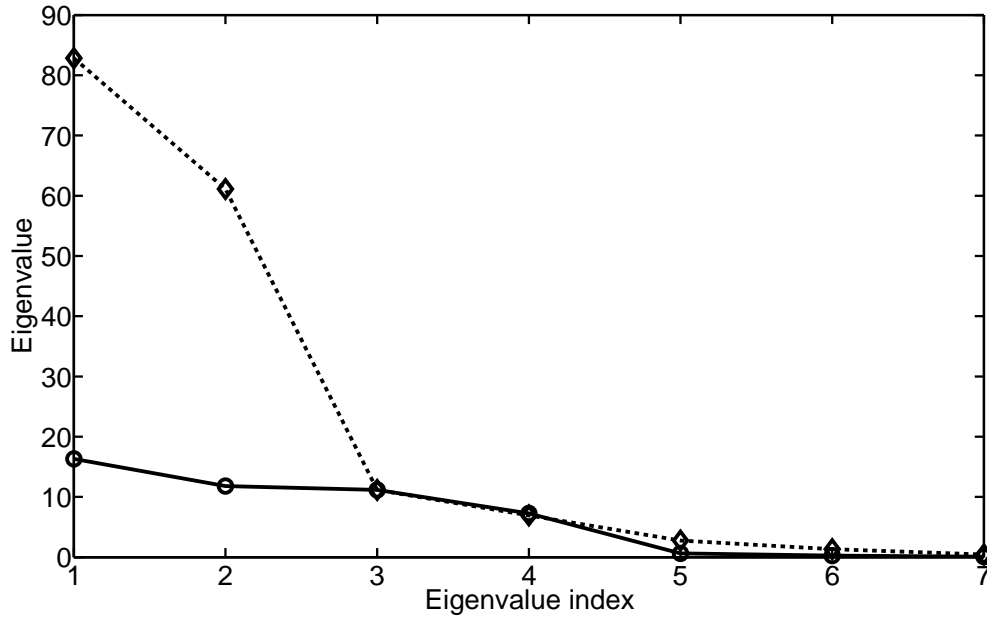
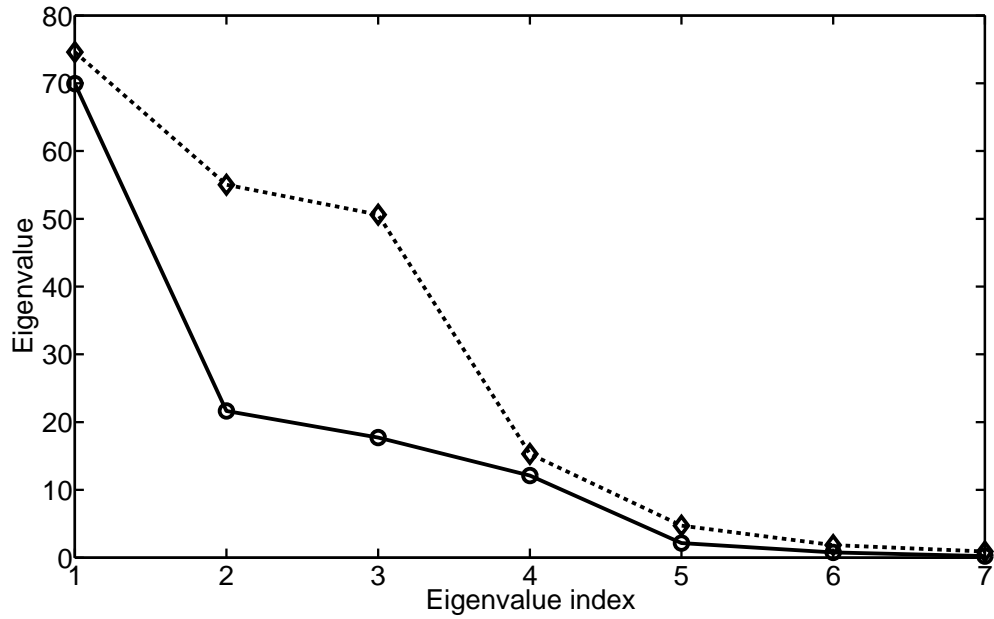


Figure 2.7: Eigenvalues of the Hessian matrices associated with the horizontal displacement component (circles) and the vertical component (diamonds). The input data include PP reflections for the model in Figure 2.1 for $X/Z=1$.

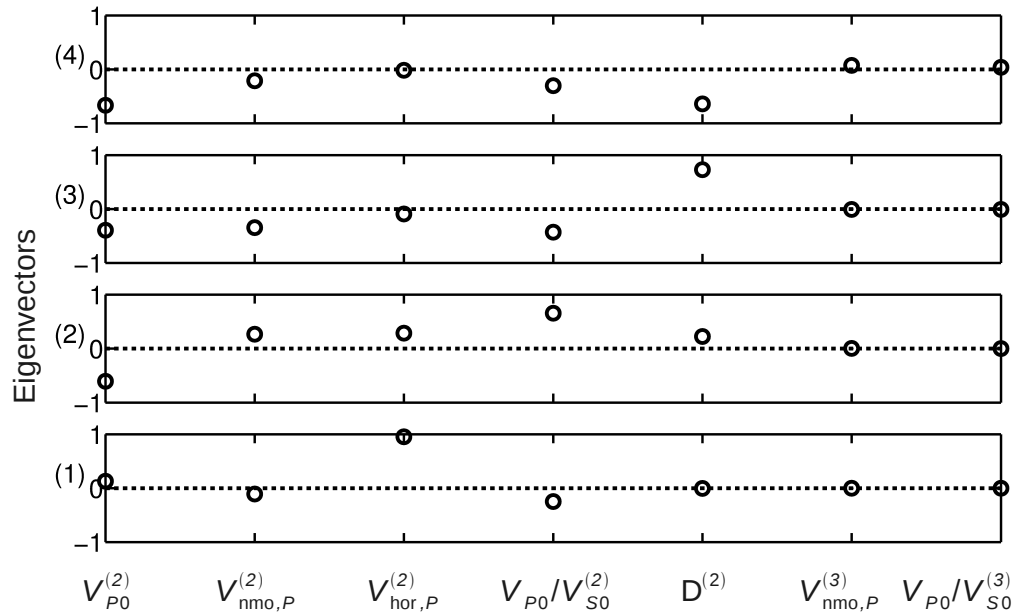
the joint PP/PS inversion toward the correct interval parameters is strongly dependent on the initial parameters. If the initial value of δ is set to zero in each layer (which causes a maximum error in δ of just 0.1) the inversion of PP and PS data gets trapped in local minima.

The sensitivity of the inversion to the initial model can be reduced by using a multiscale approach (Bunks et al., 1995). We apply four high-cut filters (limited by 3, 7, 11, and 15 Hz) to the recorded and modeled data and run four iterations for each frequency range. The low frequencies used in the beginning ensure that the objective function has fewer local minima, which are far apart. Therefore, after each update the solution moves closer to the global minimum. As a result, the algorithm operating with PP and PS data recorded for $X/Z_4 = 1$ (Z_4 is the depth of the bottom of the model) converges from the initial $\delta = 0$ to the correct values in just a few iterations (Figure 2.10).

When only PP data are inverted, the objective function apparently has a simpler shape (as for the first model), and the multiscale approach proved to be unnecessary. In the remaining tests, we focus on PP-wave inversion and contaminate the input traces with band-limited (10-25 Hz) random



(a)



(b)

Figure 2.8: (a) Eigenvalues of the Hessian matrices associated with the horizontal component (circles) and the vertical component (diamonds). (b) Components of the eigenvectors (numbered 1 to 4) associated with the four largest eigenvalues of \mathbf{H}_x . The input data include PP reflections for the model in Figure 2.1 for $X/Z=2$. The data are contaminated with band-limited (10-25 Hz) random noise; the signal-to-noise ratio is five.

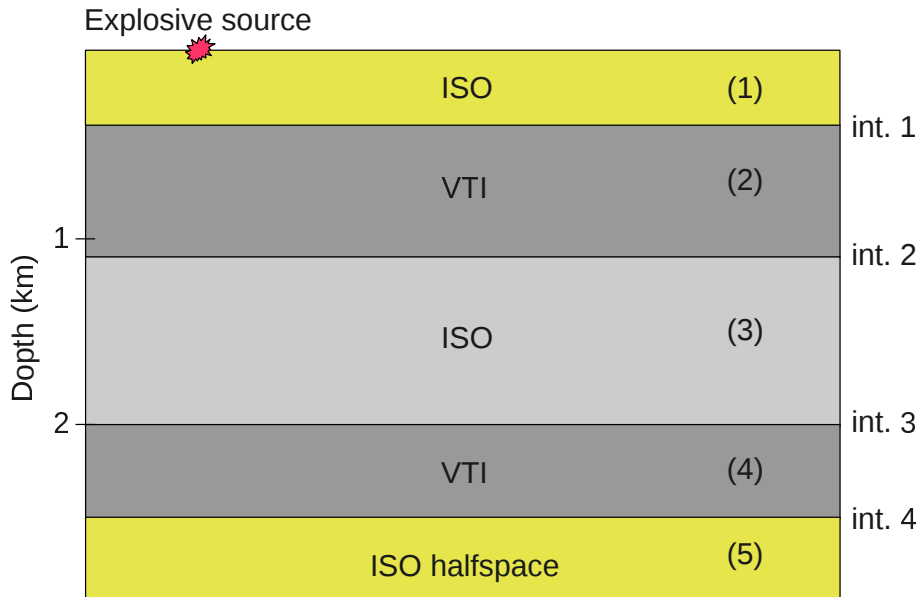


Figure 2.9: Model with two VTI layers sandwiched between isotropic media. The parameters of layer 1 are $V_P = 2800$ m/s, $V_S = 1400$ m/s, and $\rho = 1.8$ gm/cm³; for layer 2, $V_{P0} = 3000$ m/s, $V_{S0} = 1632$ m/s, $\epsilon = 0.1$, $\delta = -0.05$, and $\rho = 2.1$ gm/cm³; for layer 3, $V_P = 3400$ m/s, $V_S = 1800$ m/s, and $\rho = 2.4$ gm/cm³; for layer 4, $V_{P0} = 3700$ m/s, $V_{S0} = 2000$ m/s, $\epsilon = 0.25$, $\delta = 0.1$, and $\rho = 2.8$ gm/cm³; and for the bottom halfspace, $V_P = 4300$ m/s, $V_S = 2200$ m/s, and $\rho = 3.1$ gm/cm³.

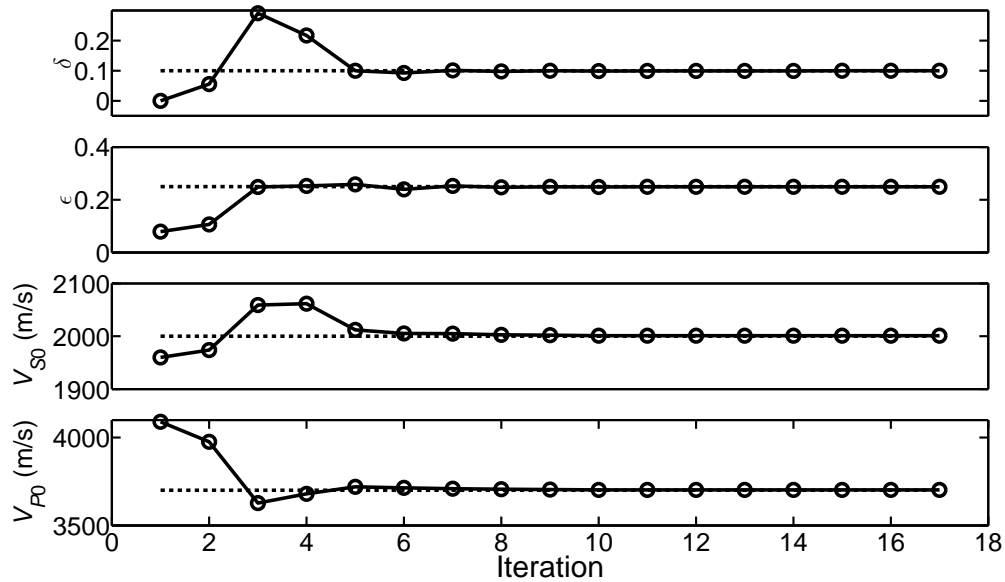


Figure 2.10: Parameters of layer 4 from the model in Figure 2.9 after each iteration when inversion is performed using a multiscale approach. The input data include PP and PS reflections; the spreadlength-to-depth ratio for the bottom of the model $X/Z_4 = 1$.

noise, as before. The eigenvector/eigenvalue decomposition of the Hessian matrix indicates that the objective function is most sensitive to the parameters V_{P0} , $V_{\text{hor},P}$, and D of the shallow VTI layer and to the P-wave velocity in the isotropic layer immediately below it. The influence of the parameters of the deeper layers on the objective function is much weaker.

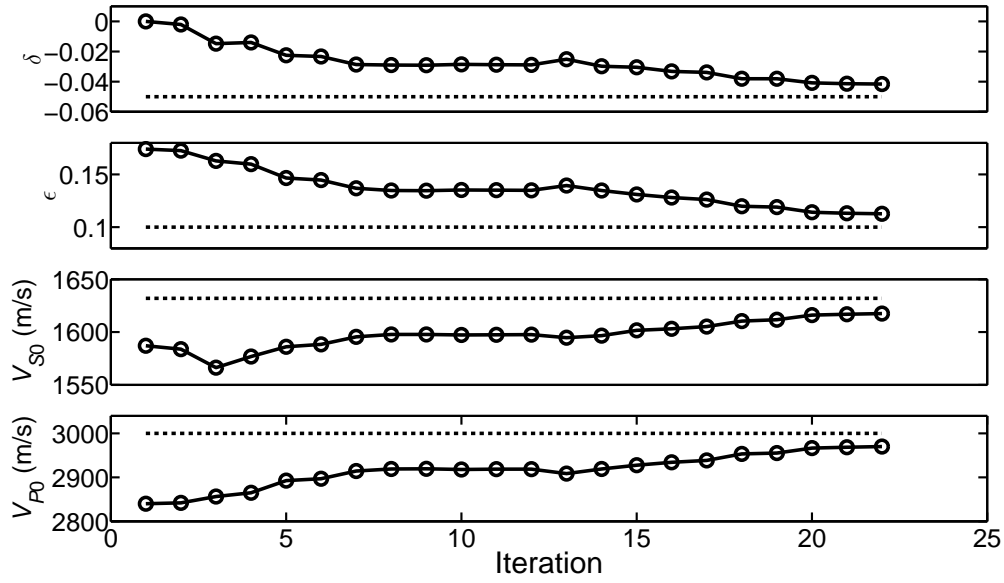
If the maximum offset is equal to the depth of the bottom of the model, the spreadlength-to-depth ratio for the bottom of the shallow VTI layer (X/Z_2) is close to 2.2. Then the parameters of that layer are well-constrained (Figure 2.11(a)), but there are significant errors in ϵ and δ for the deeper VTI layer (Figure 2.11(b)). As demonstrated above, inversion for such spreadlengths becomes stable with the addition of PS data (Figure 2.10).

However, for $X/Z_4 = 2$, the parameters of both VTI layers are accurately resolved with just PP-waves. Even in the presence of moderate band-limited random noise, the velocity V_{P0} for the deeper VTI layer is distorted by less than 2.2%, and the errors in ϵ and δ do not exceed 0.03 (Figure 2.12(b)). Therefore, when data include sufficiently long offsets, it is possible to invert for V_{P0} , V_{S0} , ϵ , and δ with only PP reflections.

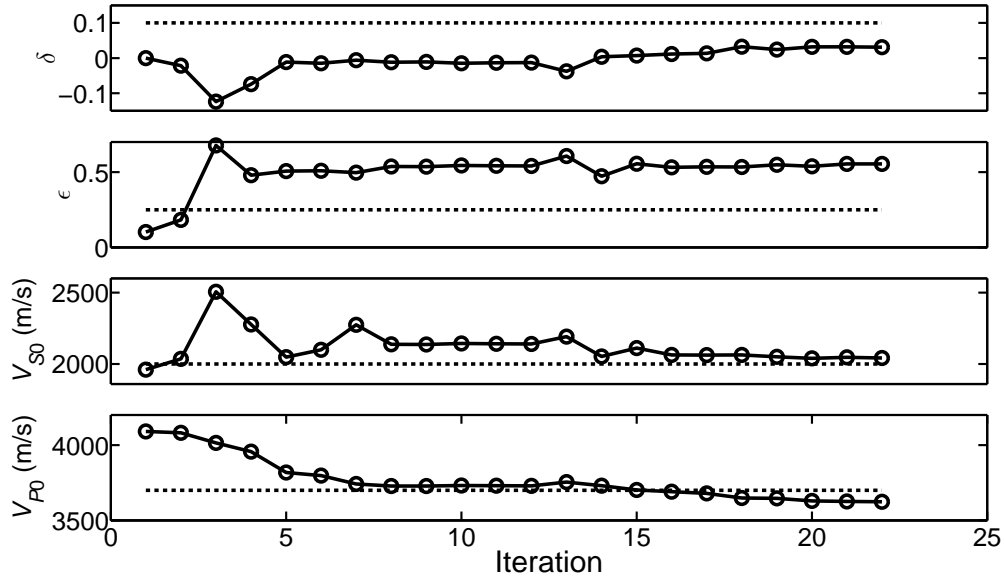
2.4 Conclusions

It is well known that the depth scale of horizontally layered VTI models is not constrained by reflection traveltimes of PP- and PS(PSV)-waves, even if long-spread data are acquired. Here, we show that the P- and S-wave interval vertical velocities and anisotropy parameters ϵ and δ of layer-cake VTI media can be estimated by full-waveform inversion of reflection data.

Our gradient-based inversion algorithm operates in the time domain with either PP reflections or the combination of PP-waves and mode-converted PS-waves. Modeling is carried out with the anisotropic reflectivity method, which generates exact 3D multicomponent wavefields for laterally homogeneous anisotropic media. The initial model for FWI is obtained from nonhyperbolic moveout inversion followed by kinematic layer stripping. It should be emphasized that our FWI algorithm estimates the parameters of all layers simultaneously to mitigate downward error propagation.

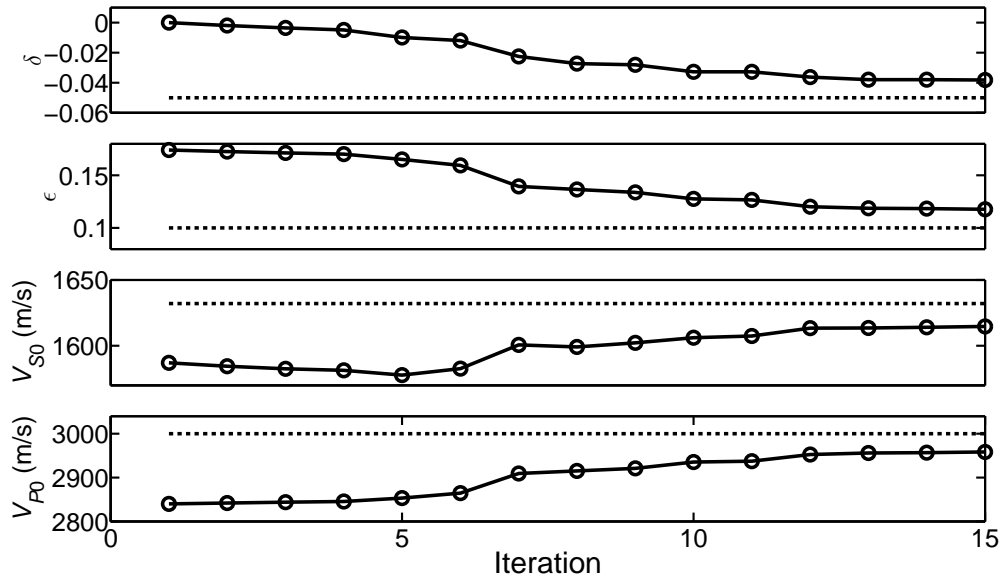


(a)

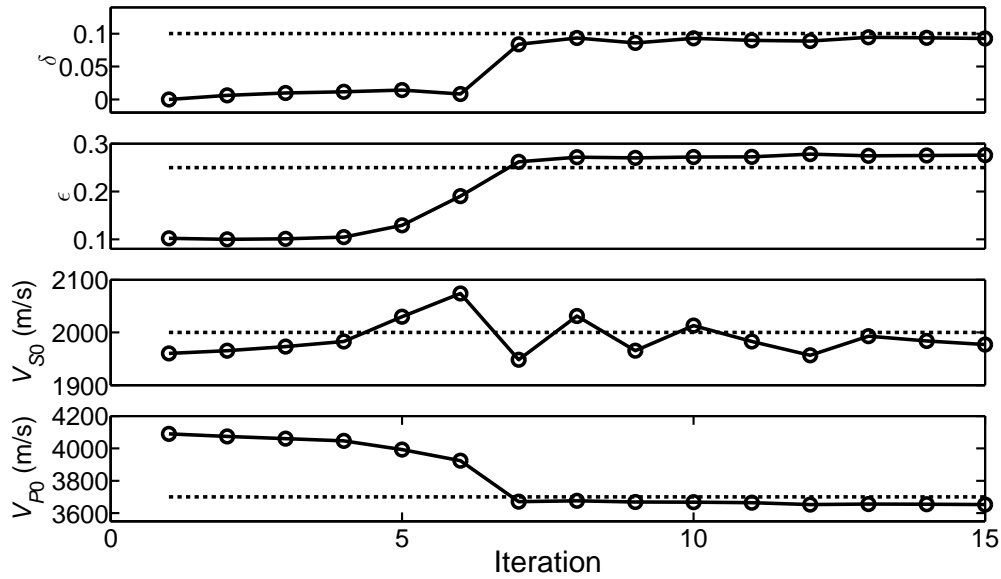


(b)

Figure 2.11: Parameters of (a) layer 2 and (b) layer 4 from the model in Figure 2.9 after each iteration. The input data include PP reflections; the spreadlength-to-depth ratio for the bottom of layer 2 is $X/Z_2 = 2.2$ (for the bottom of the model, $X/Z_4 = 1$). The data are contaminated with band-limited (10-25 Hz) random noise; the signal-to-noise ratio is 14.



(a)



(b)

Figure 2.12: Parameters of (a) layer 2 and (b) layer 4 from the model in Figure 2.9 after each iteration. The input data include PP reflections; the spreadlength-to-depth ratios are $X/Z_2 \approx 4.5$ and $X/Z_4 = 2$. The data are contaminated with band-limited (10-25 Hz) random noise; the signal-to-noise ratio is 14.

The parameters of the first layer have to be fixed at the correct values. Indeed, the near-surface velocity field on land often is strongly heterogeneous and its influence can be removed using static and datum corrections. Inverting for density increases the nonlinearity of the objective function and creates multiple local minima. Therefore, similar to most published FWI algorithms, we assume density to be known a priori.

First, we examined the inversion for a single VTI layer sandwiched between isotropic media. If the densities are known, the parameters V_{P0} , V_{S0} , ϵ , and δ are well-constrained by PP-waves alone. Interestingly, PP data produce accurate parameter estimates even for conventional spreadlengths limited by the reflector depth ($X/Z = 1$) due to additional constraints provided by the reflection coefficient (which is sensitive to V_{S0}) and geometric-spreading factor.

Application of FWI to multilayered VTI models showed that the sensitivity of the objective function to the interval parameters decreases with depth. However, if the ratio X/Z for the bottom of the deepest VTI layer reaches two, its parameters can be obtained from the inversion of PP reflections. Stable parameter estimation for smaller spreads requires the inclusion of PS-waves.

Whereas combining PP data with PS reflections adds useful constraints, it also increases sensitivity to the choice of the initial model. We found that such sensitivity can be mitigated using a multiscale approach, which also improves the convergence of the algorithm.

The wavefields analyzed here are generated for a stack of homogeneous layers and, therefore, do not include diving waves. In practice, diving waves help constrain the low-wavenumber component of the model, whereas reflections improve the spatial resolution. We plan to include both diving waves and reflected waves in our FWI algorithm for laterally heterogeneous VTI media, which is currently under development.

The FWI algorithm for stratified VTI media can be generalized for vertical symmetry planes of azimuthally anisotropic models (e.g., orthorhombic). However, geometric spreading in the symmetry planes of orthorhombic media is influenced by azimuthal velocity variations and has to be modeled in 3D.

The developed method should be applicable to many onshore reservoirs, such as unconventional shale plays, which are embedded in horizontally layered sediments. Our inversion technique based on the Gauss-Newton method cannot be directly extended to laterally heterogeneous media. Still, the presented results provide useful insights for designing inversion operators capable of handling more complicated heterogeneous structures.

2.5 Acknowledgments

We are grateful to the members of the A(nisotropy)-Team of the Center for Wave Phenomena (CWP), Colorado School of Mines (CSM), for fruitful discussions. We would also like to thank Jyoti Behura (CWP) for numerous helpful suggestions. The reviews by the anonymous referees of Geophysics were instrumental in improving the manuscript. This work was supported by the Consortium Project on Seismic Inverse Methods for Complex Structures at CWP and by the CIMMM Project of the Unconventional Natural Gas and Oil Institute (UNGI) at CSM.

CHAPTER 3
ELASTIC FULL-WAVEFORM INVERSION FOR VTI MEDIA: METHODOLOGY AND
SENSITIVITY ANALYSIS

Most existing implementations of full-waveform inversion (FWI) are limited to acoustic approximations. In this paper, we present an algorithm for time-domain elastic FWI in laterally heterogeneous VTI (transversely isotropic with a vertical symmetry axis) media. The adjoint-state method is employed to derive the gradients of the objective function with respect to the stiffness coefficients and then to a chosen set of VTI parameters. To test the algorithm, we introduce Gaussian anomalies in the Thomsen parameters of a homogeneous VTI medium and perform 2D FWI of multicomponent transmission data for two different model parameterizations. To analyze the sensitivity of the objective function to the model parameters, we obtain the Fréchet kernel of FWI is obtained by linearizing the elastic wave equation using the Born approximation and employing the asymptotic Green's function. The amplitude of the kernel ('radiation pattern') yields the angle-dependent energy scattered by a perturbation in a certain model parameter. Then we convert the general expressions into simple approximations for the radiation patterns of P- and SV-waves in VTI media. These analytic developments provide valuable insight into the potential of multicomponent elastic FWI and help explain the numerical results for models with Gaussian anomalies in the VTI parameters.

3.1 Introduction

Full-waveform inversion (FWI) is a technique for estimating subsurface properties by using recorded seismic waveforms. Depending on the problem and availability of forward-modeling algorithms, FWI can be performed in the time domain (Bunks et al., 1995; Gauthier, 1986; Kolb et al., 1986; Mora, 1987) or frequency domain (Pratt, 1999; Pratt and Shipp, 1999; Song and Williamson, 1995; Song et al., 1995). Evaluation of the gradient of the objective function is often

based on the adjoint-state method, as described in Bamberger (1982), Tarantola (1984a), Fichtner et al. (2006), and Liu and Tromp (2006).

FWI has been extended to anisotropic media, but is applied typically in the acoustic approximation (Gholami et al., 2011, 2013b; Plessix and Cao, 2011; Plessix and Rynja, 2010; Shen, 2012). A critical issue for anisotropic FWI is model parameterization. Thomsen notation, widely used in velocity analysis for VTI media, includes the vertical P- and S-wave velocities, V_{P0} and V_{S0} , and the anisotropy coefficients ϵ , δ , and γ . The anisotropy parameters are often replaced in FWI by the P-wave normal-moveout (NMO) velocity ($V_{\text{nmo}} = V_{P0}\sqrt{1 + 2\delta}$) and horizontal velocity ($V_{\text{hor}} = V_{P0}\sqrt{1 + 2\epsilon}$).

In the case of multiparameter inversion, the results strongly depend on the parameterization and the type of input data (for example, diving waves, near-offset or far-offset reflections). Plessix and Cao (2011) evaluate the sensitivity of the FWI objective function to different parameters by performing singular value decomposition (SVD) of the Fréchet derivative (or ‘sensitivity’) matrix. Another method of analyzing sensitivity is by computing the Fréchet kernel for a point scatterer in the subsurface (Alkhalifah and Plessix, 2014; Eaton and Stewart, 1994; Prioux et al., 2013a). The amplitude of the kernel as a function of the scattering angle (called the “radiation pattern”) reveals the sensitivity of FWI to a model parameter for a certain range of angles.

Gholami et al. (2013b) use finite differences to compute the Fréchet kernel for a point diffractor embedded in a homogeneous acoustic VTI space. An analytic description of the radiation patterns associated with a VTI perturbation in a homogeneous isotropic medium is presented by Alkhalifah and Plessix (2014). They study the radiation patterns for two parameterizations (V_{nmo} , η , δ and V_{hor} , η , ϵ) and conclude that either parameter set can be used when the inversion is carried out with a hierarchic approach.

Plessix and Cao (2011) also perform acoustic FWI of diving waves and small-offset reflection data generated for a synthetic VTI model and test different parameterizations with the goal of updating the low-wavenumber component of the model. They show that the combination of V_{nmo} , V_{hor} , and δ provides “slightly better” results than V_{nmo} , η , and δ . Using data from Valhall field,

Prieux et al. (2011) update the velocity V_{P0} with acoustic FWI, while keeping ϵ and δ fixed. These results are used as a benchmark to compare the velocity fields obtained with and without taking anisotropy into account. Warner et al. (2013) estimate V_{P0} by performing 3D acoustic FWI of field data from the North Sea with fixed profiles of ϵ and δ .

Anisotropic acoustic algorithms, however, do not properly handle reflection amplitudes and cannot be applied to multicomponent data. Elastic FWI of synthetic multicomponent surface data (consisting of both diving waves and reflections) for VTI media is performed by Lee et al. (2010), but suboptimal parameterization in terms of the stiffness coefficients causes ambiguity in their results.

In our previous work (Kamath and Tsvankin, 2013), we invert multicomponent reflection data (PP- and PSV-waves) from a horizontally layered VTI model for the interval Thomsen parameters V_{P0} , V_{S0} , ϵ , and δ . Although PP-waves alone may be sufficient to resolve V_{P0} , V_{S0} , ϵ , and δ , stable interval parameter estimation for layers at depth requires employing long-offset data (with the spreadlength-to-depth ratio reaching at least two) or the addition of PS-waves. Inversion of multicomponent data benefits from using a multiscale approach (Bunks et al., 1995), which reduces the sensitivity to the choice of the initial model.

Here, we introduce an extension of elastic FWI to laterally heterogeneous VTI media and study the sensitivity of the inversion to two different sets of model parameters. To compute the gradient of the objective function, we adapt the results of Liu and Tromp (2006) obtained with the adjoint-state method. Sensitivity analysis is performed by deriving the Fréchet kernel for elastic FWI using the Born and WKBJ approximations and an asymptotic representation of the Green's function. The kernel, obtained for arbitrarily anisotropic media, is then used to obtain the radiation patterns for the relevant model parameters. The developed algorithm is applied to transmission data generated for a homogeneous VTI background model with Gaussian anomalies in the Thomsen parameters. The inversion results are explained using the P- and SV-wave radiation patterns for a VTI scatterer.

3.2 Methodology

Here, we discuss gradient computation of the objective function using the adjoint-state method, and radiation patterns for anomalies in VTI parameters embedded in a homogeneous medium.

3.2.1 Full-waveform inversion for VTI media

Time-domain implementations of FWI are designed to minimize the following objective function:

$$\mathcal{F} = \frac{1}{2} \sum_{r=1}^N \|\mathbf{u}(\mathbf{x}_r, t) - \mathbf{d}(\mathbf{x}_r, t)\|^2, \quad (3.1)$$

where N is the number of receivers, $\mathbf{u}(\mathbf{x}_r, t)$ is the data (displacement) computed for a trial model, and $\mathbf{d}(\mathbf{x}_r, t)$ is the displacement recorded at receiver location \mathbf{x}_r . Equation 3.1 implies summation over multiple shots for the same receiver array. Although the relationship between the model and the data is nonlinear, a perturbation in the model is assumed to be linearly related to the perturbation in data:

$$\Delta \mathbf{m} = -\alpha \mathbf{J}^T \Delta \mathbf{d}, \quad (3.2)$$

where \mathbf{J} is the Fréchet derivative matrix, T denotes transposition, and $\Delta \mathbf{d}$ is the perturbation in the data. The model update $\Delta \mathbf{m}$ is computed as the gradient of the objective function, $\mathbf{J}^T \Delta \mathbf{d}$, scaled by α (which can be found from line search).

If the number of unknowns is relatively small (as for layered VTI media studied by Kamath and Tsvankin, 2013), the Fréchet matrix can be computed explicitly by perturbing each model parameter, which makes it possible to update the model using equation 3.2.

3.2.2 Application of the adjoint-state method

Computation of the Fréchet derivatives for laterally heterogeneous media becomes prohibitively expensive because it involves calculating as many forward models at each iteration as the number of parameters (typically defined on a grid). Hence, instead of using equation 3.2 it is more practi-

cal to calculate the gradient ($\mathbf{J}^T \Delta \mathbf{d}$ in equation 3.2) of the objective function with the adjoint-state method, which has been widely used in FWI (Fichtner et al., 2006; Liu and Tromp, 2006; Plessix, 2006; Tarantola, 1984b). The model update, which is a scaled version of the gradient, is then calculated using steepest-descent or conjugate-gradient algorithms. Alternatively, either the so-called BFGS (Broyden-Fletcher-Goldfarb-Shanno) method or its limited-memory equivalent, the L-BFGS method (both are quasi-Newton techniques), can be employed to scale the gradient by the inverse of an approximate Hessian matrix (Pratt et al., 1998; Virieux and Operto, 2009).

The adjoint-state method is designed to compute the gradient of the objective function using the so-called “adjoint wavefield.” Because the variable-density elastic wave equation is self-adjoint, it can be solved for the adjoint wavefield with the data residuals treated as sources (see Appendix A). The residuals at each time step are injected “backward in time” (i.e., starting from the last time sample), which is commonly described as back-propagation of data residuals. For 2D multi-component data, the vertical and horizontal displacement components of the data residuals should be injected into the medium simultaneously. The gradient computation, as shown in Appendix A, involves applying the imaging condition to the spatial derivatives of the forward and adjoint wavefields.

Here, we assume that the properties of the VTI medium vary in 2D and consider only in-plane polarized waves (P and SV). Hence, the model is described by four stiffness coefficients (written in the Voigt notation): C_{11} , C_{33} , C_{13} , and C_{55} . However, description of wave propagation and inversion of seismic data can be facilitated by employing Thomsen parameters and their combinations (e.g., the anellipticity coefficient η , Alkhalifah and Tsvankin, 1995). Lee et al. (2010), who parameterize the VTI model in terms of the stiffnesses, are unable to resolve the coefficient C_{13} , likely because of the tradeoff between C_{13} and C_{55} in P-wave kinematic signatures (Tsvankin, 2012).

Kamath and Tsvankin (2013) could constrain the relevant Thomsen parameters (V_{P0} , V_{S0} , ϵ , and δ), although the algorithm operated with the vertical velocities of P- and S-waves and the P-wave NMO and horizontal velocities. Here we define the model either in terms of the velocities V_{P0} , V_{S0} , V_{nmo} , and V_{hor} (parameterization I) or using $\ln(1/V_{P0}^2)$, $\ln(1/V_{S0}^2)$, $(1 + 2\epsilon)$, and $(1 + 2\delta)$

(parameterization II). The latter combination is an extension of Shen’s (2012) parameterization to elastic media; also, in contrast to Shen (2012), we update the coefficient δ during the inversion rather than keeping it fixed.

The gradients of the objective function (equation 3.1) with respect to the elements of the stiffness tensor are derived in Appendix A using the results of Liu and Tromp (2006):

$$\frac{\partial \mathcal{F}}{\partial c_{ijkl}} = - \int_0^T \frac{\partial u_i}{\partial x_j} \frac{\partial \psi_k}{\partial x_l} dt, \quad (3.3)$$

where \mathbf{u} and ψ are the forward and adjoint displacement wavefields, respectively. Using the chain rule, we can find the gradient for each model parameter m_n :

$$\frac{\partial \mathcal{F}}{\partial m_n} = \sum_{ijkl} \frac{\partial \mathcal{F}}{\partial c_{ijkl}} \frac{\partial c_{ijkl}}{\partial m_n}. \quad (3.4)$$

The stiffness coefficients are expressed in terms of the velocities (V_{P0} , V_{S0} , V_{nmo} , and V_{hor}) in equations A.18–A.21. Combining equations 3.3, 3.4, and A.18–A.21 yields the gradients for parameterization I (equations A.22–A.25). In a similar manner, we derive the gradients for parameterization II (equations A.31–A.34).

FWI is implemented here in the time domain and the model is updated using the steepest-descent method combined with a parabolic line-search algorithm. The same step length is used for all medium parameters.

3.2.3 Radiation patterns for elastic FWI

To obtain expressions for radiation patterns produced by a scatterer in the subsurface, we consider an elastic, anisotropic homogeneous background medium with spatially varying perturbations in the stiffness coefficients. It should be emphasized that the perturbed stiffnesses correspond to an arbitrarily anisotropic medium. Afterwards, we obtain relatively simple expressions for the radiation patterns assuming the background to be isotropic and the perturbations to have VTI symmetry.

General expressions

Following Calvet et al. (2006) and Alkhalifah and Plessix (2014), we represent the elastic wave equation for a perturbation δc_{ijkl} in the stiffness tensor using the Born approximation:

$$\rho \frac{\partial^2 \delta u_i}{\partial t^2} - \frac{\partial}{\partial x_j} \left(c_{ijkl} \frac{\partial \delta u_k}{\partial x_l} \right) = \frac{\partial}{\partial x_j} \left(\delta c_{ijkl} \frac{\partial u_k}{\partial x_l} \right), \quad (3.5)$$

where $\delta \mathbf{u}$ is the corresponding perturbation in the wavefield, and ρ is the density. The solution of equation 3.5 can be expressed in terms of the Green's functions G_{mk} and G_{ni} (Appendix B):

$$\begin{aligned} \delta u_n(\mathbf{x}_r, \omega) = & - \int_{V(\mathbf{x}')} f_m(\mathbf{x}_s, \omega) \delta c_{ijkl}(\mathbf{x}') \\ & \times \frac{\partial G_{mk}(\mathbf{x}_s, \mathbf{x}', \omega)}{\partial x'_l} \frac{\partial G_{ni}(\mathbf{x}_r, \mathbf{x}', \omega)}{\partial x'_j} dV(\mathbf{x}'), \end{aligned} \quad (3.6)$$

where \mathbf{x}_s and \mathbf{x}_r are the locations of the source and receiver, respectively, f is the density of body forces, and $V(\mathbf{x}')$ is the volume that includes all scatterers \mathbf{x}' . The Green's functions are then replaced by their asymptotic representation (Vavryčuk, 2007). Taking the spatial derivative of just the exponent of \mathbf{G} (i.e., of its rapidly varying part, according to the WKBJ approximation) yields (equation B.13):

$$\delta u_n(\mathbf{x}_r, \omega) = \int_{V(\mathbf{x}')} f_m(\mathbf{x}_s, \omega) \mathcal{A}(\omega) p_l^s p_j^r g_k^s g_i^r \delta c_{ijkl} dV(\mathbf{x}'). \quad (3.7)$$

Here, the superscripts s and r denote the source (incident) and receiver (scattered) wavefields, respectively, $\mathcal{A}(\omega)$ is a function of frequency and the background velocities for the incident and scattered wavefields (equation B.14), and \mathbf{p} and \mathbf{g} are the unit slowness and polarization vectors, respectively. The radiation pattern is the amplitude of the kernel in equation 3.7 that varies with the incident and scattering angles. For a model parameterized in terms of the stiffnesses, the radiation pattern derived from equation 3.7 is (equation B.15):

$$\Omega = p_l^s p_j^r g_k^s g_i^r. \quad (3.8)$$

Equation 3.8 is valid for a perturbation δc_{ijkl} corresponding to an elastic, arbitrarily anisotropic scatterer in 3D. In this study, however, we consider the in-plane polarized waves (P and SV) in a 2D elastic VTI medium, so the indices $i, j, k,$ and l in equations 3.6–3.8 take values of 1 and 3.

Application to VTI media

In Appendix B, we use equation 3.8 to obtain explicit expressions for the radiation patterns in VTI media. The normalized scattering coefficients for the P- and SV-wavefields for parameterization I are given by equations B.16–B.19 and B.20– B.23, respectively. In the case of the transmitted wavefield, the incidence and scattering angles coincide. Substituting equations B.24 – B.31 into equations B.16 – B.23, we obtain the following radiation patterns (normalized by $4\rho V_{P0}$) for the scattered P-wavefield:

$$\Omega^P(V_{P0}) = \cos^2 \theta, \quad (3.9)$$

$$\Omega^P(V_{S0}) = 0, \quad (3.10)$$

$$\Omega^P(V_{\text{nmo}}) = \frac{1}{4} \sin^2 2\theta, \quad (3.11)$$

$$\Omega^P(V_{\text{hor}}) = \sin^4 \theta, \quad (3.12)$$

where θ is the incidence angle. The patterns for the scattered SV-wavefield (normalized by $2\rho V_{P0}$) are:

$$\Omega^S(V_{P0}) = 0, \quad (3.13)$$

$$\Omega^S(V_{S0}) = -2 \frac{V_{S0}}{V_{P0}}, \quad (3.14)$$

$$\Omega^S(V_{\text{nmo}}) = \frac{1}{2} \sin^2 2\theta, \quad (3.15)$$

$$\Omega^S(V_{\text{hor}}) = \frac{1}{2} \sin^2 2\theta, \quad (3.16)$$

The absolute values (magnitude) of the radiation patterns in Figure 3.1 show how perturbations in the velocities V_{P0} , V_{nmo} , and V_{hor} scatter P-wave energy for different incidence angles. In our approximation, a perturbation in V_{S0} does not influence the scattered P-wavefield. As expected, the

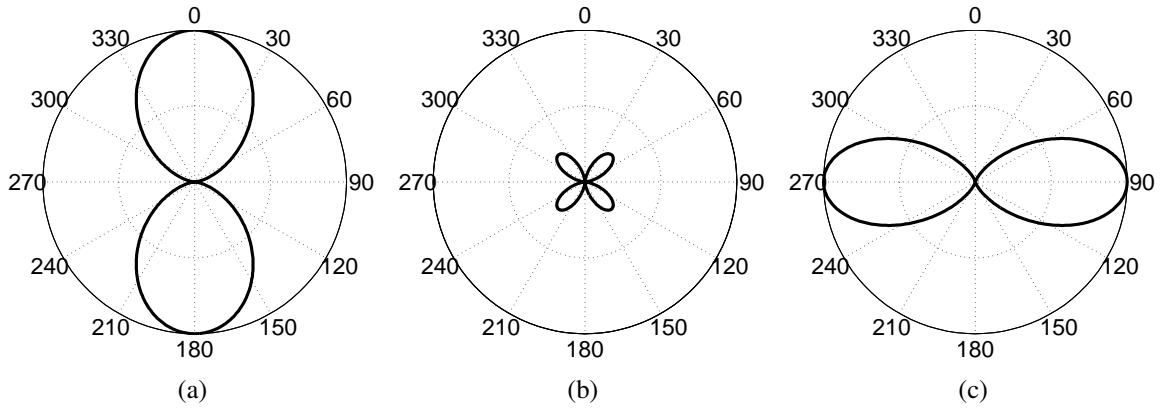


Figure 3.1: Radiation patterns of the velocities (a) V_{P0} , (b) V_{nmo} , and (c) V_{hor} computed from equations 3.9, 3.11, and 3.12 (respectively) for the P-wavefield. The VTI perturbations are inserted into a homogeneous isotropic background.

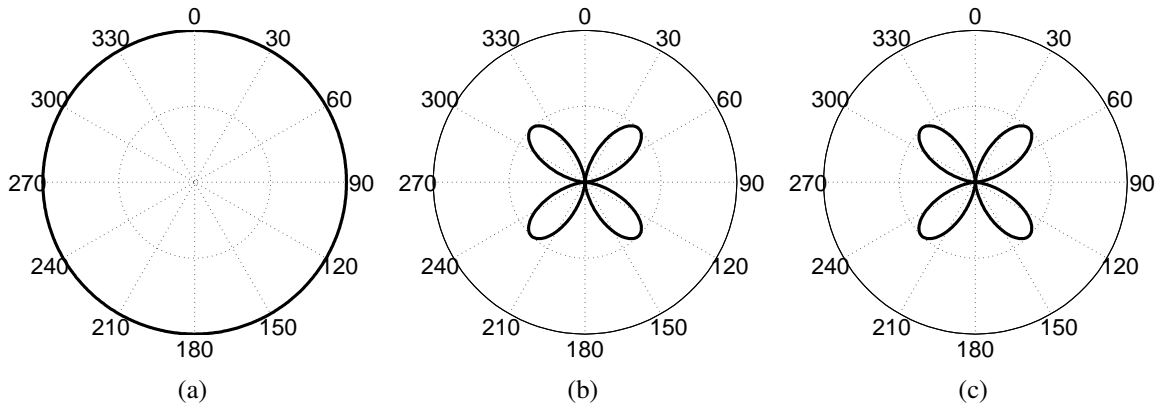


Figure 3.2: Radiation patterns of the velocities (a) V_{S0} , (b) V_{nmo} , and (c) V_{hor} computed from equations 3.14, 3.15, and 3.16 (respectively) for the S-wavefield. The VTI perturbations are inserted into a homogeneous isotropic background; the ratio $V_{S0}/V_{P0} = 0.5$.

intensity of the wavefield scattered by a perturbation in V_{P0} reaches its maximum for propagation along the symmetry axis and goes to zero in the orthogonal (isotropy) plane (Figure 3.1(a)). In contrast, a perturbation in V_{hor} produces the largest scattering in the isotropy plane, with a rapid decay toward the symmetry axis (Figure 3.1(c)). The maximum energy scattered by a perturbation in V_{nm0} is four times smaller than that for V_{P0} and corresponds to an angle of 45° with the symmetry axis (Figure 3.1(b)).

A perturbation in V_{S0} scatters the SV-wavefield uniformly for the entire range of incidence angles (Figure 3.2(a)), which is likely due to the fact that V_{S0} also represents the horizontal SV-wave velocity. The radiation patterns of V_{nm0} and V_{hor} (Figure 3.2(b) and Figure 3.2(c), respectively) for SV-waves are similar to that of V_{nm0} for the P-wave (Figure 3.1(b)). The SV-wave is primarily influenced by V_{S0} and the parameter $\sigma = (V_{P0}/V_{S0})^2(\epsilon - \delta) = (V_{\text{hor}}^2 - V_{\text{nm0}}^2)/(2V_{S0}^2)$ (Tsvankin, 2012). Therefore, for a model described in terms of V_{P0} , V_{S0} , V_{nm0} , and V_{hor} , the SV-wavefield is weakly dependent on the velocity V_{P0} . This explains why a perturbation in V_{P0} does not scatter SV-waves (equation 3.13).

The P-wave radiation patterns for the velocities V_{P0} , V_{nm0} , and V_{hor} are centered at angles 0° , 45° , and 90° , respectively, which mitigates the trade-off in the scattered energy for this parameterization. These radiation patterns can be used to qualitatively predict those for other parameterizations. For instance, if the model is described by the Thomsen parameters V_{P0} , ϵ , and δ , anomalies in both V_{P0} and δ should be responsible for the scattered energy near 45° because $V_{\text{nm0}} = V_{P0}\sqrt{1 + 2\delta}$. Similarly, one would expect anomalies in both V_{P0} and ϵ to contribute to scattering near the isotropy plane, as $V_{\text{hor}} = V_{P0}\sqrt{1 + 2\epsilon}$.

Because the scattered SV-wavefield is not sensitive to V_{P0} , the SV-wave radiation patterns for ϵ and δ have the same shape as those for V_{hor} and V_{nm0} , respectively. By making similar arguments, it is possible to deduce the general behavior of the radiation patterns for other parameterizations, such as the ones discussed in Gholami et al. (2013b) and Alkhalifah and Plessix (2014). Note that the radiation patterns for the transmitted P-wavefield in elastic media are identical to those obtained for acoustic media. Elastic FWI, however, also includes SV-waves, which help estimate

the velocity V_{S0} and better constrain the other parameters.

The P-wave radiation patterns (normalized by ρV_{P0}^2) for parameterization II, obtained analogously to those for parameterization I, are:

$$\Omega^P(\ln(1/V_{P0}^2)) = -1, \quad (3.17)$$

$$\Omega^P(\ln(1/V_{S0}^2)) = 0, \quad (3.18)$$

$$\Omega^P(1 + 2\epsilon) = \sin^4 \theta, \quad (3.19)$$

$$\Omega^P(1 + 2\delta) = \frac{1}{4} \sin^2 2\theta. \quad (3.20)$$

For the scattered S-wavefield (normalized by $\rho V_{P0}^2/4$), we find:

$$\Omega^S(\ln(1/V_{P0}^2)) = 0, \quad (3.21)$$

$$\Omega^S(\ln(1/V_{S0}^2)) = -4 \frac{V_{S0}^2}{V_{P0}^2}, \quad (3.22)$$

$$\Omega^S(1 + 2\epsilon) = \sin^2 2\theta, \quad (3.23)$$

$$\Omega^S(1 + 2\delta) = -\sin^2 2\theta. \quad (3.24)$$

Here, the velocities are normalized by 1 km/s. The P- and S-wave radiation patterns for parameterization II, computed from equations 3.17–3.24, are plotted in Figure 3.3 and Figure 3.4. These patterns generally confirm the above arguments regarding the sensitivity analysis in terms of Thomsen parameters. For example, the radiation patterns of the parameters $1 + 2\epsilon$ and $1 + 2\delta$ for both P- and SV-waves have the same shape as those for V_{hor} and V_{nmo} obtained for parameterization I.

The radiation patterns do not change if the velocities (or their squares) are used instead of the logarithm of the squared slownesses. However, we prefer to employ the logarithm for two reasons: (a) to make the parameters dimensionless, with the same order of magnitude as that of the anisotropy coefficients (because we do not have an inverse Hessian scaling the gradient), and (b) Shen (2012) showed that the logarithm-based parameterization may lead to faster convergence. Note that an anomaly in $\ln(1/V_{P0}^2)$ scatters P-wave energy uniformly in all directions (Figure 3.3(a)), which means that updates in V_{P0} are independent of the source-receiver configuration.

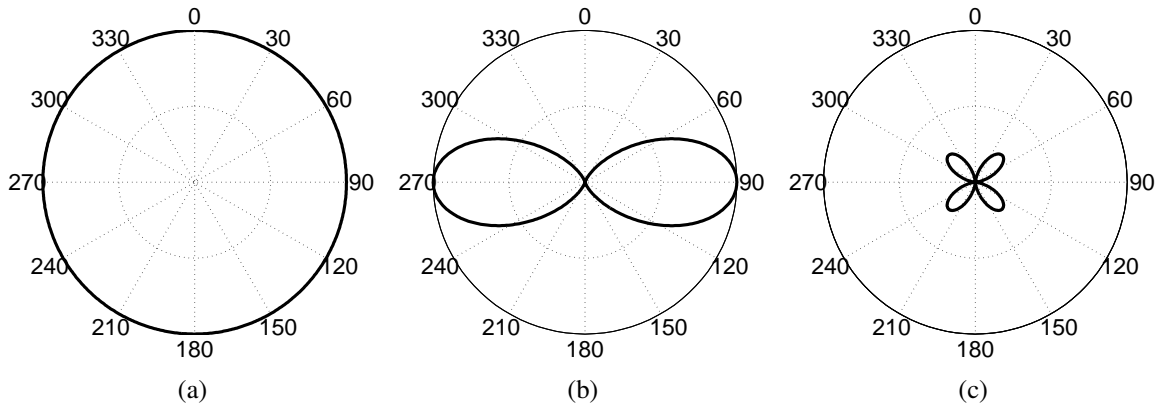


Figure 3.3: Radiation patterns of the parameters (a) $\ln(1/V_{P0}^2)$, (b) $1 + 2\epsilon$, and (c) $1 + 2\delta$ computed from equations 3.17, 3.19, and 3.20 (respectively) for the P-wavefield.

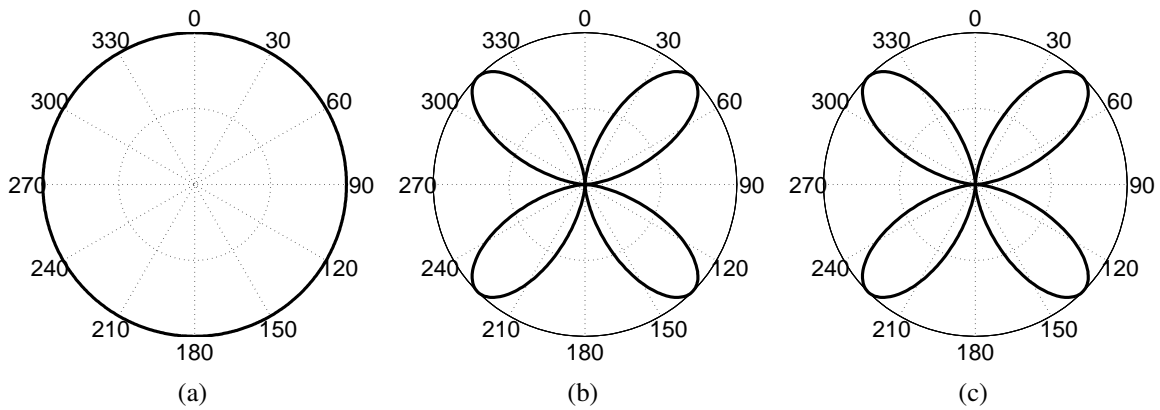


Figure 3.4: Radiation patterns of the parameters (a) $\ln(1/V_{S0}^2)$, (b) $1 + 2\epsilon$, and (c) $1 + 2\delta$ computed from equations 3.22, 3.23, and 3.24 (respectively) for the S-wavefield. The ratio $V_{S0}/V_{P0} = 0.5$.

Parameterization I yields radiation patterns that are more “orthogonal” (have less overlap), but this also restricts the range of wavenumbers that can be recovered by FWI (e.g., one can obtain only low-wavenumber updates for V_{hor}). The second parameterization has a velocity (V_{P0}) which has a more “isotropic” radiation pattern. This helps retrieve a wider range of wavenumbers for V_{P0} , but creates trade-offs between V_{P0} and the anisotropy coefficients.

3.3 Analysis of FWI of transmission data

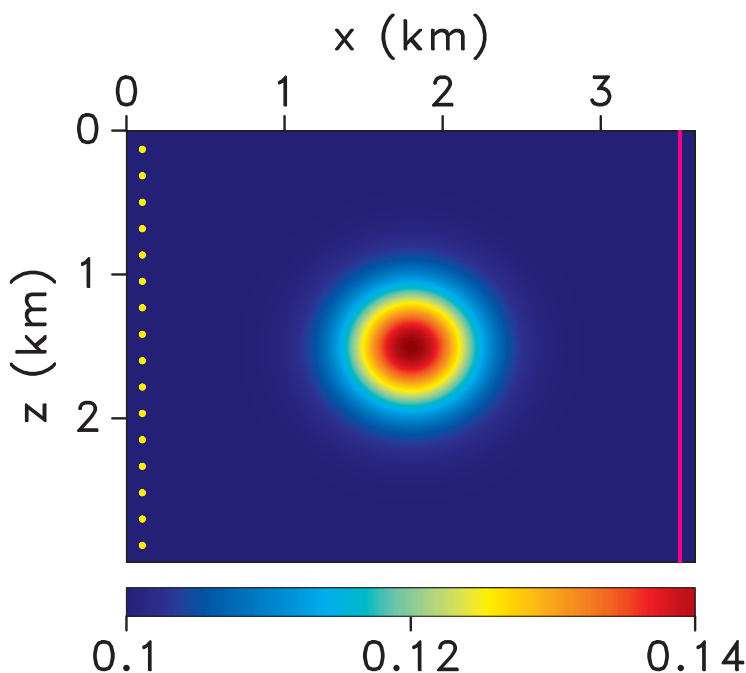


Figure 3.5: VTI model with a Gaussian anomaly (standard deviation $\sigma = 300$ m) in the anisotropy parameter ϵ . The background and maximum values of ϵ are 0.1 and 0.142, respectively. The other Thomsen parameters are spatially invariant: $V_{P0} = 3000$ m/s, $V_{S0} = 1500$ m/s, and $\delta = -0.05$. The dots on the left mark the source locations and the vertical line on the right represents an array of receivers placed at each grid point (6.6 m apart). The wavefields are generated by horizontal displace sources.

Next, we perform tests for simple synthetic models to verify the accuracy of the gradient computation and of the inversion algorithm as a whole. In addition, we employ the analytic expressions for radiation patterns obtained above to explain the inversion results. Because the initial stage of FWI typically involves diving waves, the data are generated for transmission experiments. The

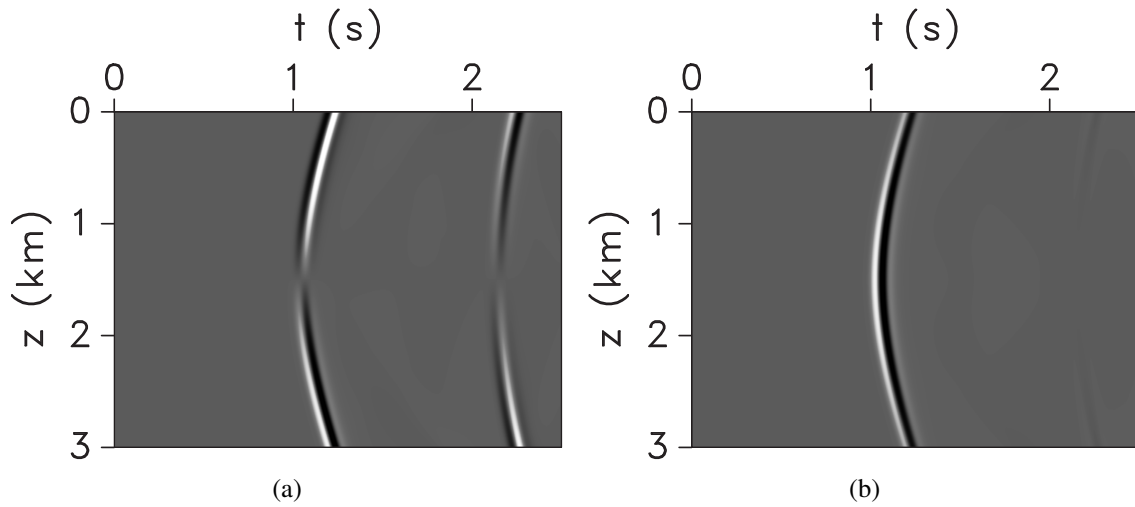


Figure 3.6: (a) Vertical and (b) horizontal displacements for the model in Figure 3.5 generated by a shot at $z = 1.5$ km.

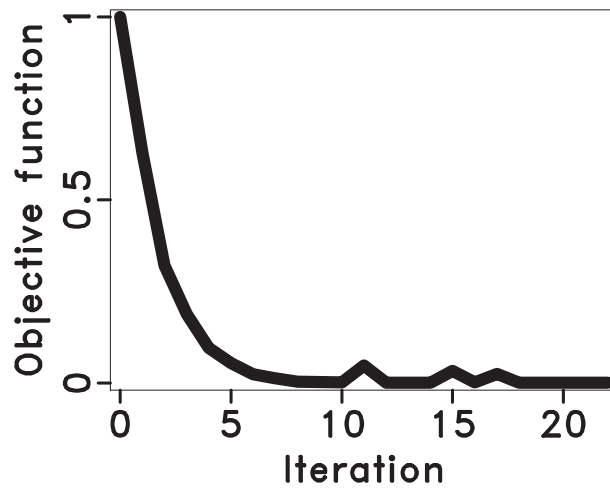


Figure 3.7: Change in the normalized objective function with iterations for the model from Figure 3.5.

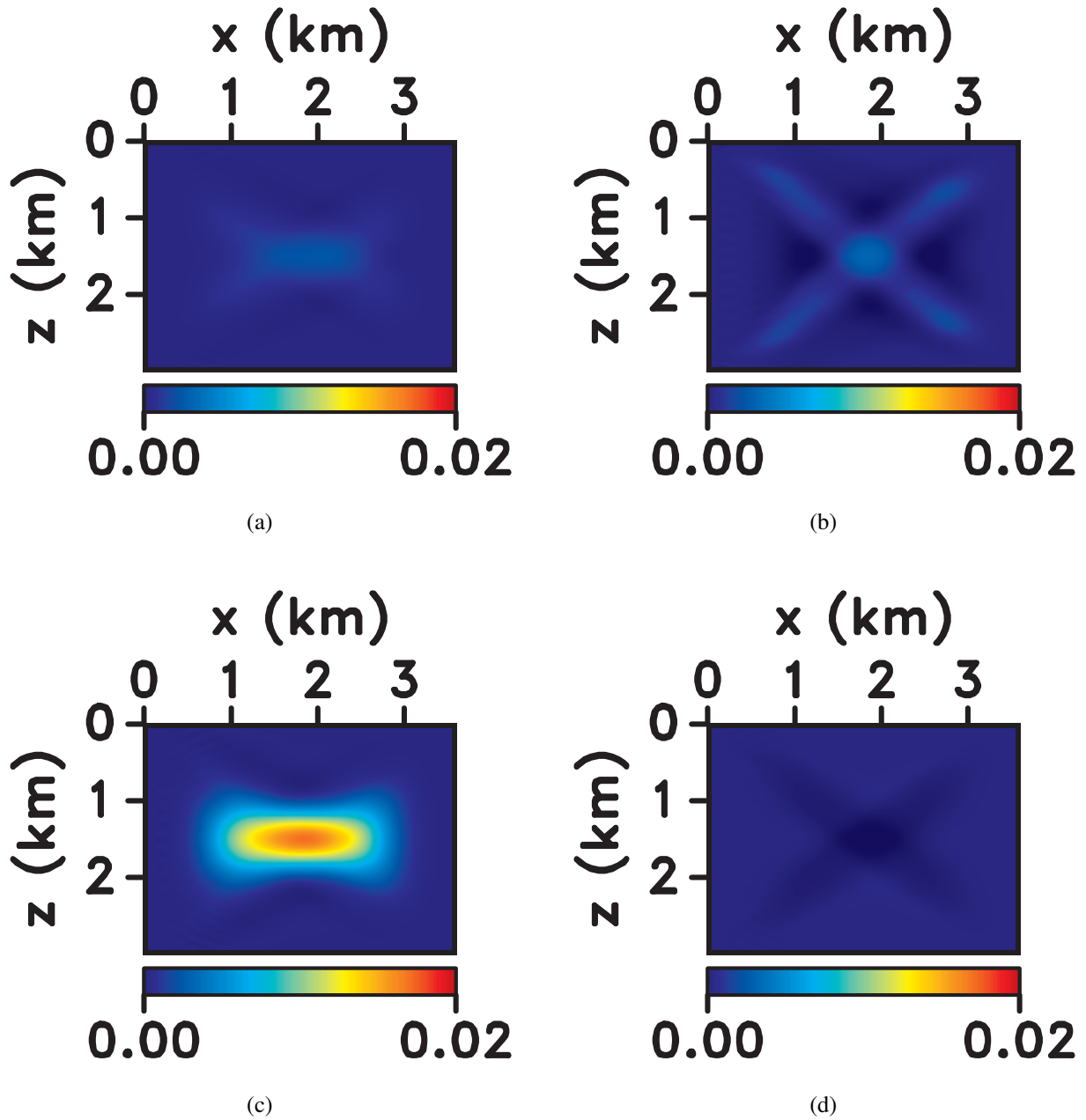


Figure 3.8: Fractional difference between the estimated and initial (background) parameters (a) V_{P0} and (b) V_{S0} for the model from Figure 3.5. The difference between the estimated and initial parameters (c) ϵ and (d) δ for the same model.

model includes Gaussian anomalies in the Thomsen parameters V_{P0} , V_{S0} , and ϵ inserted into a homogeneous VTI background between line arrays of sources and receivers.

The set of tests in Figure 3.5–Figure 3.18 is performed for parameterization I (V_{P0} , V_{S0} , V_{hor} , and V_{nmo}). In the first test, the model includes an anomaly in ϵ , while the other parameters are spatially invariant (Figure 3.5). The wavefield is generated by a point displacement source polarized in the horizontal direction with a peak frequency of 10 Hz. The vertical and horizontal displacements (“recorded data”) from a shot in the center of the array are shown in Figure 3.6. The “modeled” data are then generated in the background medium without the anomaly, and the adjoint source is obtained as the difference between the two wavefields.

Starting from the homogeneous background model, we perform the inversion using the steepest-descent method. We run up to 50 iterations and terminate the inversion if the objective function flattens out earlier (Figure 3.7). The inverted and initial values of V_{P0} and δ are close, which confirms that FWI converges toward the actual model. The updates in V_{hor} , combined with negligible changes in V_{P0} , ensure the reconstruction of the anomaly in ϵ (Figure 3.8).

These results are well explained by the radiation patterns in Figure 3.1. For this source-receiver geometry, the aperture is about 41° on both sides of the isotropy (horizontal) plane. The amplitude of the energy scattered by V_{hor} reduces by 50% at an angle of about $\pm 33^\circ$ from the horizontal (Figure 3.1(c)), so the radiation pattern of V_{hor} is largely decoupled from those of V_{P0} , V_{S0} , and V_{nmo} . Therefore, FWI updates only the horizontal velocity, which results in an appropriate change in the coefficient ϵ and an accurate inverted model.

Even though the objective function decreases to just 0.04% of the initial value, there is a small error in ϵ : the maximum estimated ϵ is about 0.12, whereas the actual value is 0.14. The shape of the anomaly is somewhat distorted (i.e., it is stretched along the horizontal axis) because of the source-receiver configuration. For this acquisition geometry, spatial resolution should indeed be higher in the vertical direction than horizontally, as discussed by Wu and Toksöz (1987). When the aperture is increased to about 51° on both sides of the isotropy plane (Figure 3.9), the shape of the anomaly is better resolved (Figure 3.10). In addition, because the inverted velocities are

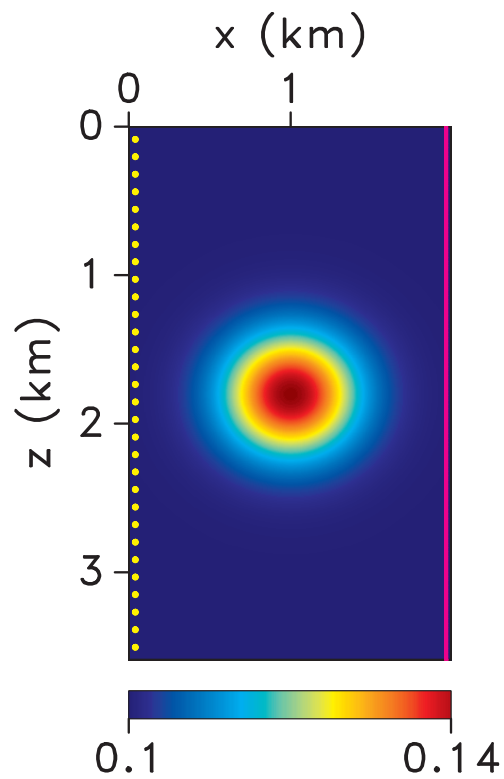
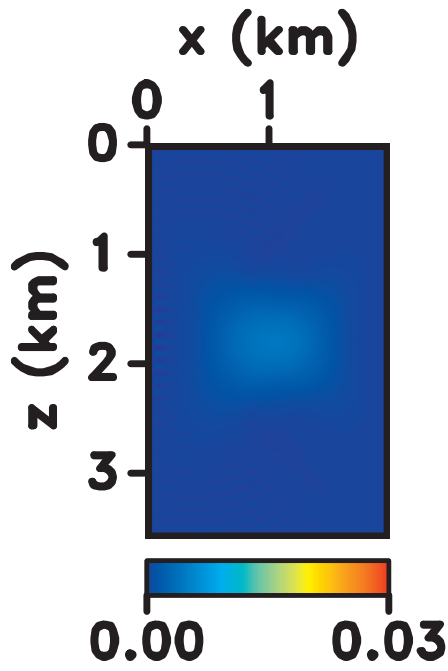
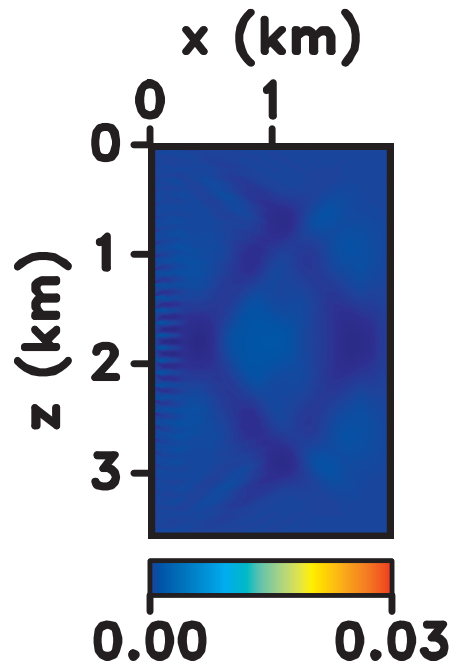


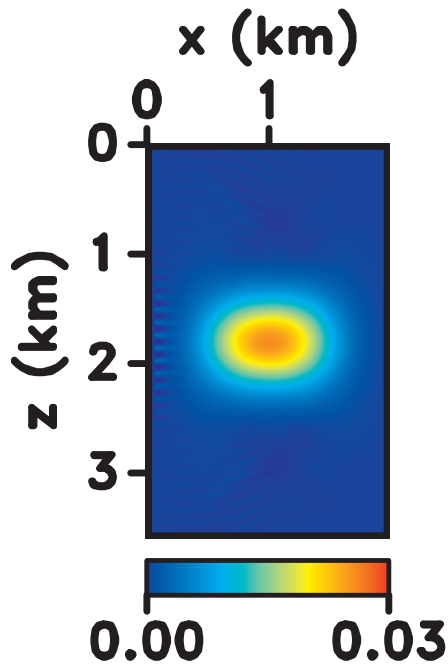
Figure 3.9: VTI model with the same parameters as in Figure 3.5, but the source and receiver arrays are extended vertically by 0.6 km and the distance between them is reduced from 3.4 to 1.92 km. The wavefields are generated by horizontal displacement sources.



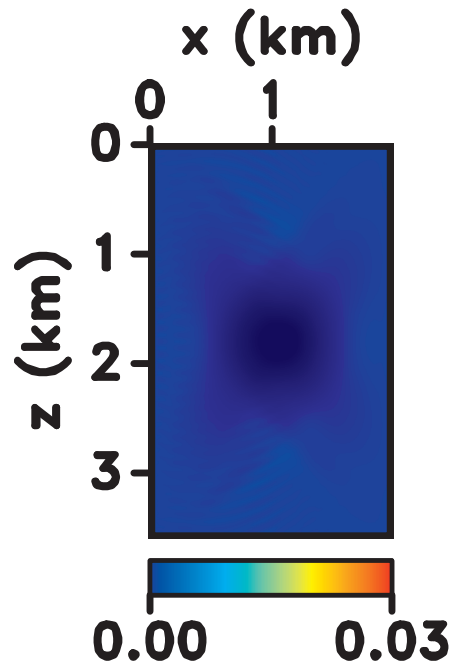
(a)



(b)



(c)



(d)

Figure 3.10: Fractional difference between the estimated and initial parameters (a) V_{P0} and (b) V_{S0} for the model from Figure 3.9. The difference between the estimated and initial parameters (c) ϵ and (d) δ for the same model.

closer to the actual values, the estimated ϵ (maximum value of 0.13) is slightly more accurate than in the previous example. This configuration, which yields better inversion results, is used in all subsequent tests.

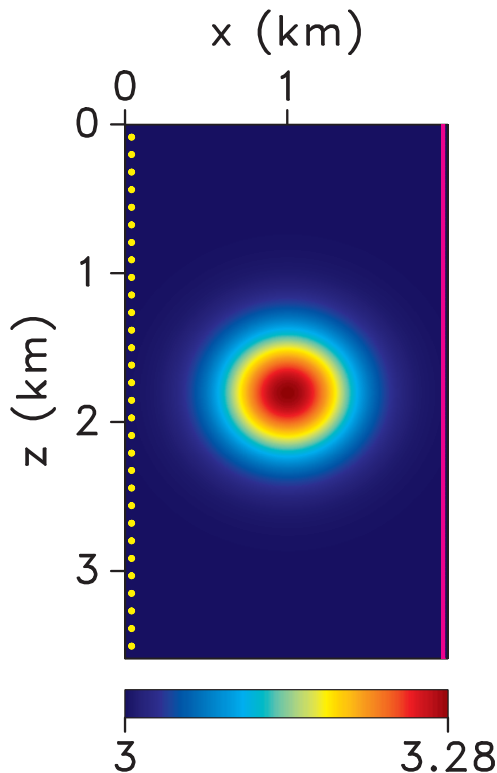
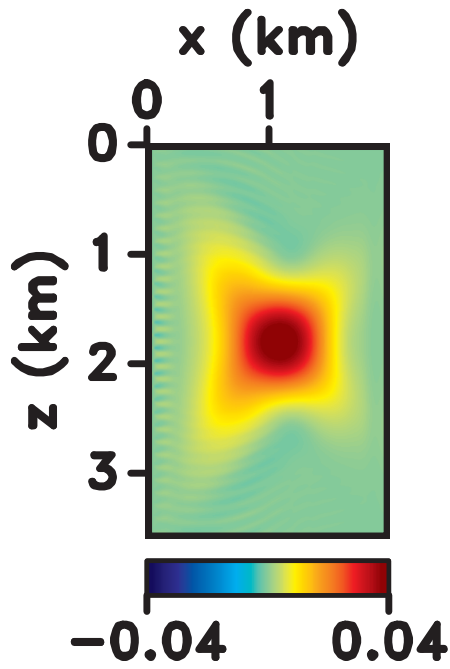
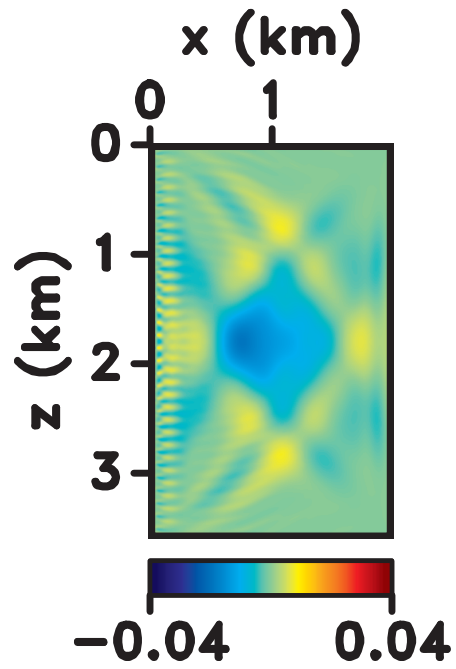


Figure 3.11: VTI model with a Gaussian anomaly in V_{P0} . The background and maximum values of V_{P0} are 3000 m/s and 3283 m/s, respectively. The other Thomsen parameters are spatially invariant: $V_{S0} = 1500$ m/s, $\delta = -0.05$, and $\epsilon = 0.1$. The wavefields are generated by horizontal displacement sources.

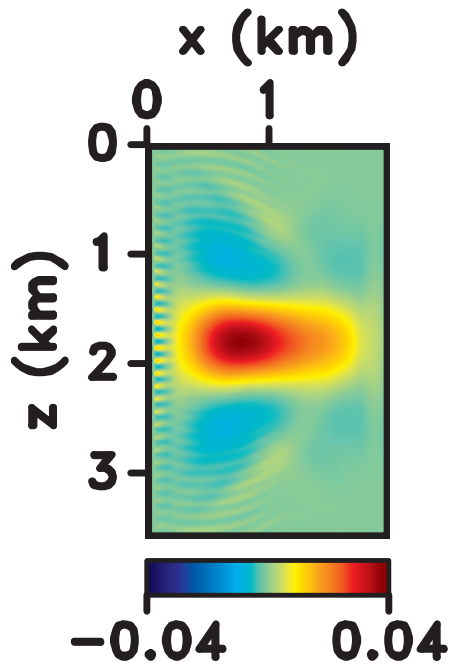
Next, we introduce an anomaly in the P-wave vertical velocity V_{P0} , with the sources still polarized horizontally (Figure 3.11). The anomaly in V_{P0} also causes perturbations in the NMO and horizontal velocities. The largest update (about 74% of the actual anomaly) for the given configuration is the one for the velocity V_{hor} , whereas the updates for V_{P0} (45%) and V_{nmo} (44%) are much smaller. A comparison of the observed displacement and that computed for the inverted model indicates that the data misfit is relatively small. Most likely, the search is trapped in a local minimum because of the complexity of the multicomponent wavefield. In a later test we show that it is possible to obtain much better results for the same configuration when the wavefield includes



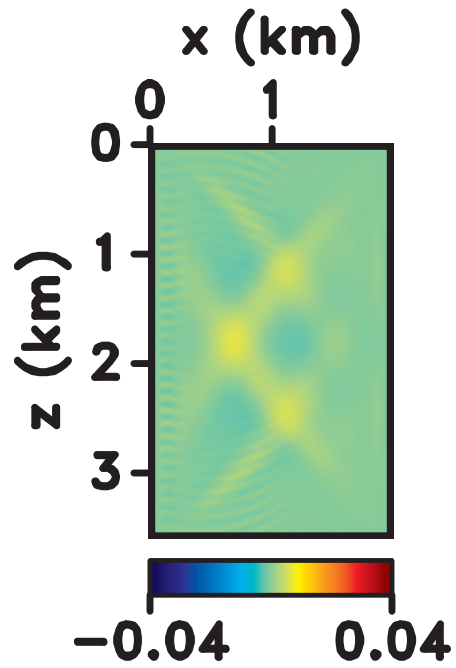
(a)



(b)



(c)



(d)

Figure 3.12: Fractional difference between the estimated and initial parameters (a) V_{P0} and (b) V_{S0} for the model from Figure 3.11. The difference between the estimated and initial parameters (c) ϵ and (d) δ for the same model.

only P-waves. Not only is the inversion unable to recover the true anomaly in V_{P0} (Figure 3.12(a)), an update in V_{hor} without the corresponding change in V_{P0} results in an undesired update in ϵ (Figure 3.12(c)). Because the parameter δ depends on the velocity ratio V_{nmo}/V_{P0} , and the inversion updates both the velocities proportionately, there is no significant change in δ (Figure 3.12(d)).

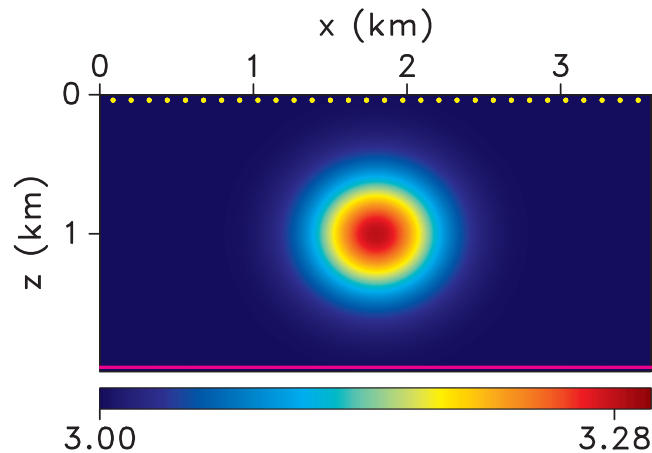
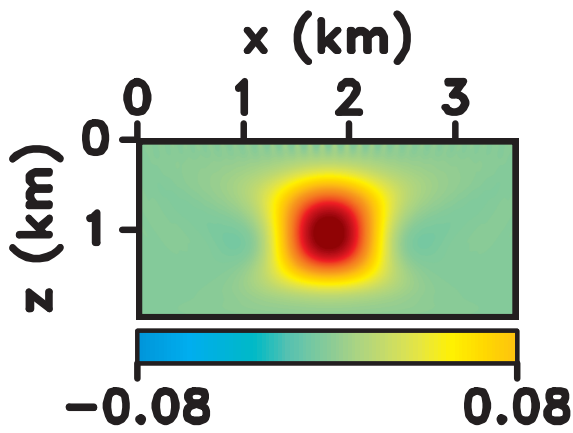


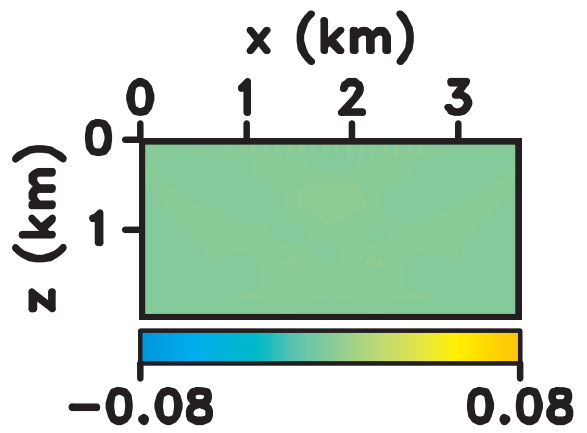
Figure 3.13: VTI model with a Gaussian anomaly in V_{P0} . The source and receiver arrays are horizontal. The wavefields are generated by vertical displacement sources.

When the source and receiver arrays for the same model are rotated by 90° (Figure 3.13), the inversion algorithm predominantly updates V_{P0} (Figure 3.14(a)). Because the receivers do not record most of the energy scattered by the anomalies in V_{nmo} and V_{hor} (Figure 3.1), the algorithm does not update these parameters. Hence, although the anomaly in V_{P0} is recovered, the parameters ϵ and δ , which depend on V_{hor} and V_{nmo} , are distorted (Figure 3.14(c) and Figure 3.14(d), respectively).

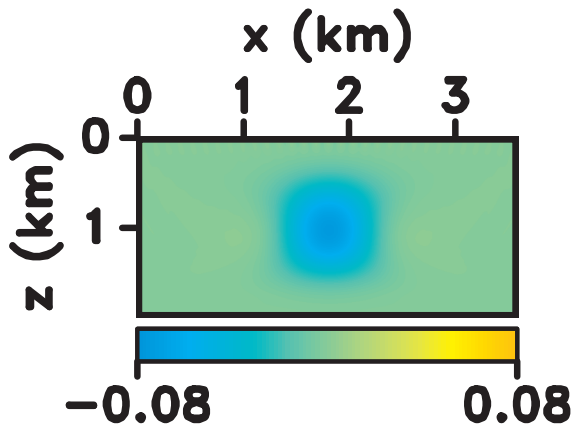
Another test is performed for a Gaussian anomaly in V_{S0} embedded between vertical source and receiver arrays (Figure 3.15). The maximum perturbation in V_{S0} with respect to the background is the same as that for V_{P0} in a previous test (Figure 3.11), but the percentage perturbation in V_{S0} is two times higher. Hence, to avoid the problem of cycle-skipping, the peak frequency of the source is reduced to 5 Hz. The inversion results, obtained using both P- and S-waves, include an update only in V_{S0} (Figure 3.16), which indicates no apparent trade-off between the model parameters. As was the case in the inversion for ϵ , despite the significant decrease in the objective function (to



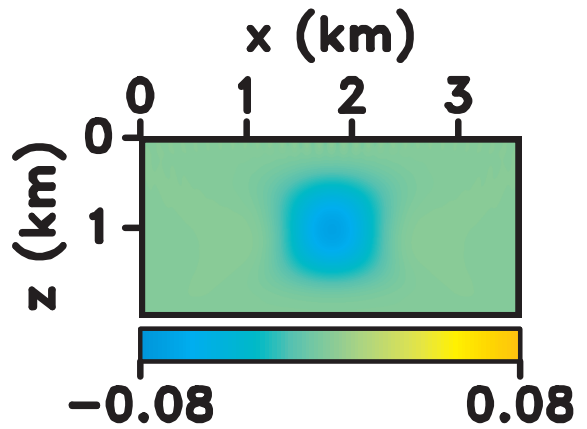
(a)



(b)



(c)



(d)

Figure 3.14: Fractional difference between the estimated and initial parameters (a) V_{P0} and (b) V_{S0} for the model from Figure 3.13. The difference between the estimated and initial parameters (c) ϵ and (d) δ for the same model.

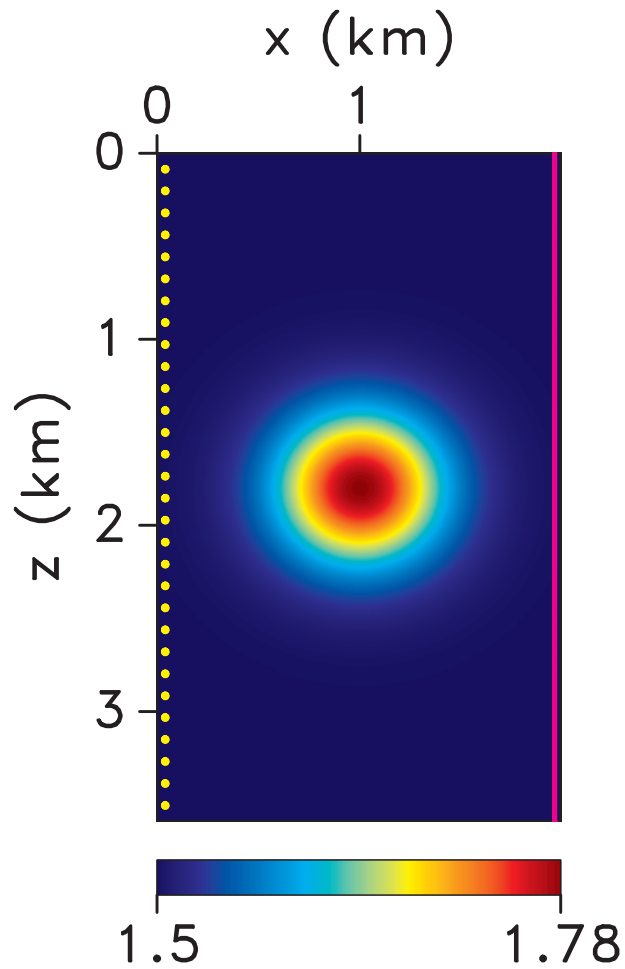


Figure 3.15: VTI model with a Gaussian anomaly in V_{S0} . The background and maximum values of V_{S0} are 1500 m/s and 1783 m/s, respectively. The other Thomsen parameters are spatially invariant: $V_{P0} = 3000$ m/s, $\delta = -0.05$, and $\epsilon = 0.1$. The wavefields are generated by vertical displacement sources.

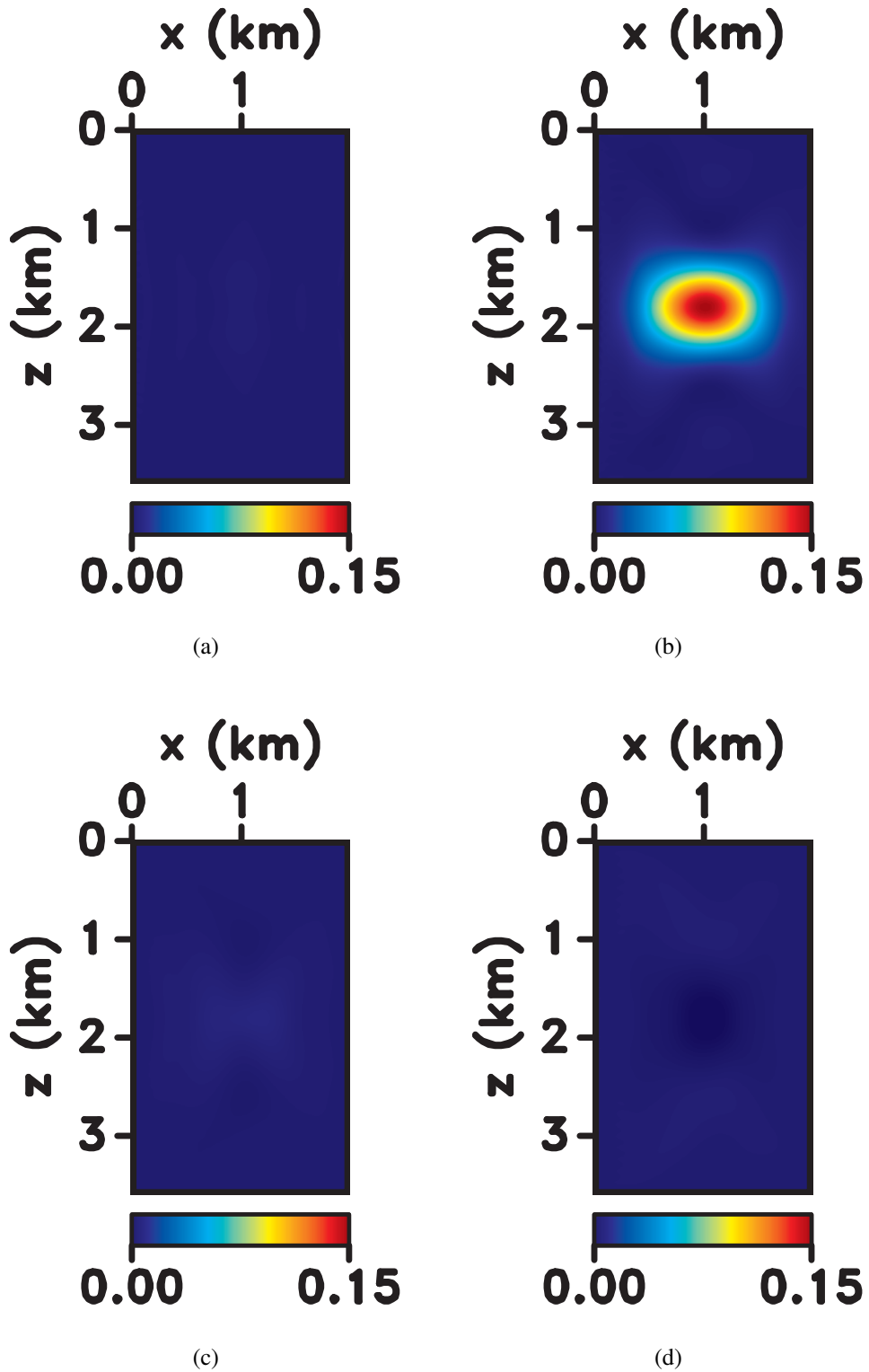


Figure 3.16: Fractional difference between the estimated and initial parameters (a) V_{P0} and (b) V_{S0} for the model from Figure 3.15. The difference between the estimated and initial parameters (c) ϵ and (d) δ for the same model.

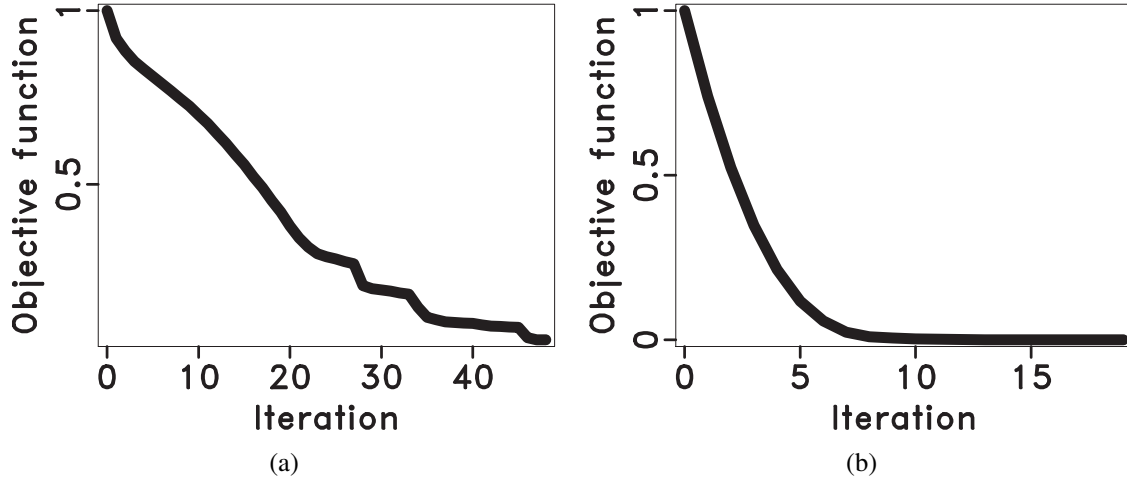


Figure 3.17: Change in the normalized objective function with iterations for the model from Figure 3.11 when the data (a) consist of both the P- and S-wave arrivals and (b) contain only the P-waves.

0.03% of the initial value), the estimated V_{S0} is off by about 3%. Interestingly, the inversion for V_{S0} yields similar results when the source and receiver arrays are horizontal and wave propagation is predominantly vertical, likely because the V_{S0} anomaly scatters the SV-waves equally in all directions (Figure 3.2(a)).

It is important to test the inversion algorithm on data consisting only of P- or SV-waves. After generating the complete wavefield for the model from Figure 3.11, we mask the S-wave arrivals. The shear data are also removed from the wavefield modeled at each iteration during the inversion, so the objective function contains the difference of the P-waveforms only. Note that although the adjoint sources include only the P-wave residuals, the adjoint wavefield contains both the P- and S-wavefields. Still, because the modeled and observed data are missing S-waves, the gradients are dominated by the P-wave events. As a result, the objective function becomes less complex and the inversion converges more rapidly (Figure 3.17). Furthermore, removing S-waves increases the accuracy of the inversion for the anomaly in V_{P0} (compare Figure 3.18 and Figure 3.12). Kamath and Tsvankin (2013), made a similar observation: operating with just PP data generally improved the convergence of FWI and the objective function seemingly became more quadratic. Note, however,

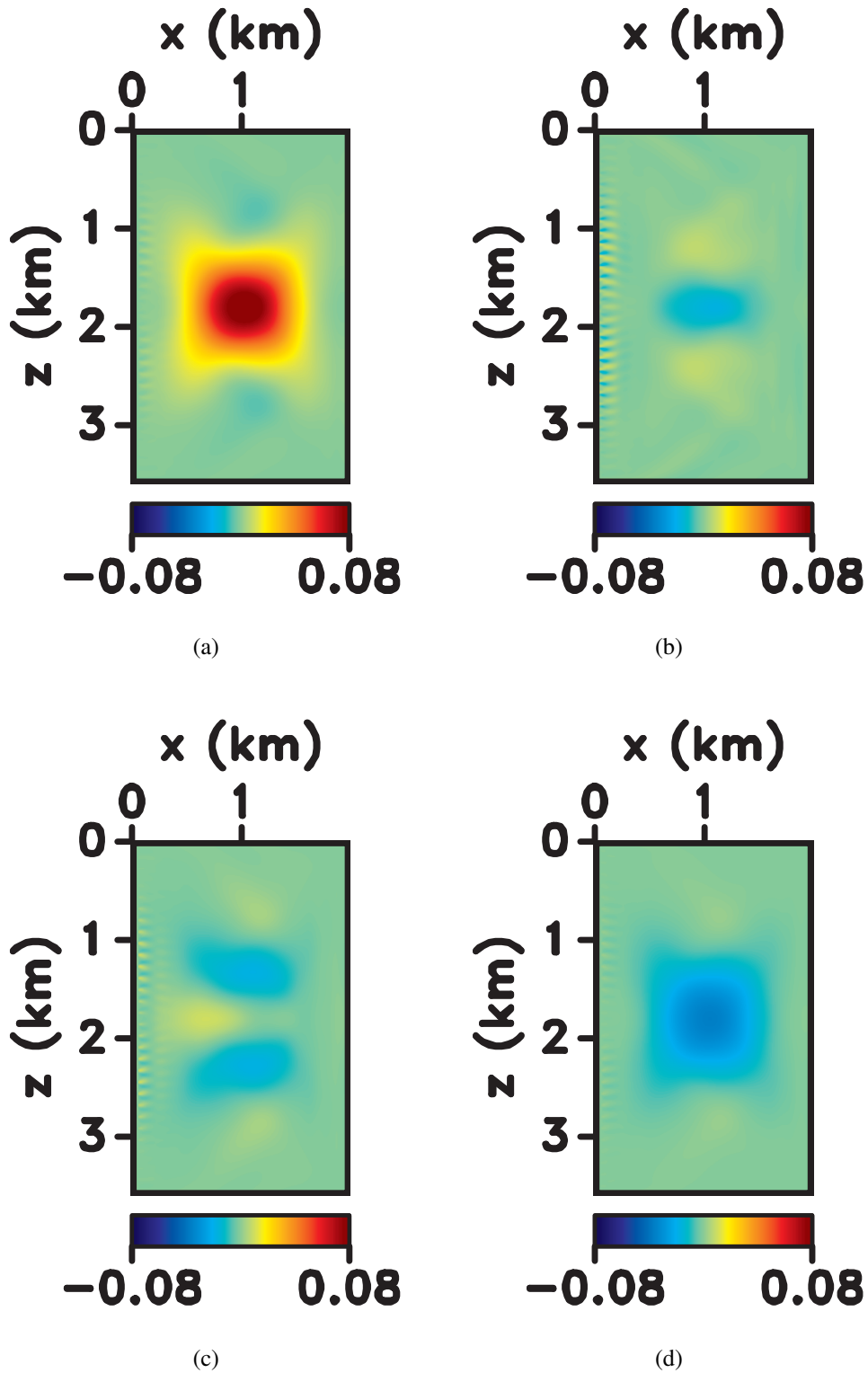


Figure 3.18: Fractional difference between the estimated and initial parameters (a) V_{P0} and (b) V_{S0} for the model from Figure 3.11 when the objective function is calculated using only the P-wave data. The difference between the estimated and initial parameters (c) ϵ and (d) δ for the same model.

that P-wave transmission data alone cannot constrain the velocity V_{S0} . Also, for more complex models, SV-waves should help better constrain the parameters V_{P0} , V_{nmo} , and V_{hor} .

Next, we mask the P-wave arrivals in both the observed and modeled data to determine the contribution of the shear wavefield to the inversion for an anomaly in ϵ (Figure 3.9). Although the adjoint wavefield contains both the P- and S-wavefields, in this case, the gradients (and, therefore, the inversion) are dominated by the SV-wave energy. FWI of SV-waves increases ϵ by only 25% of the desired update (plots for this test are not shown), whereas the joint inversion of P- and SV-waves produced a much more accurate result (Figure 3.10). In addition, there is a decrease in the value of δ , which clearly indicates the trade-off between the two parameters. Therefore, estimation of ϵ is primarily based on the information provided by P-waves.

Finally, we use parameterization II to recover the anomalies in ϵ , V_{P0} , and V_{S0} (Figure 3.9, Figure 3.11, and Figure 3.15, respectively). For the anomaly in ϵ (Figure 3.9), the results are close to those for parameterization I: the ϵ -field is well recovered, but the trade-off between V_{P0} and ϵ causes a small erroneous update in V_{P0} . The second parameterization, however, provides an improvement in the inversion results (Figure 3.19) for the anomaly in V_{P0} (Figure 3.11). Because the radiation pattern of $\ln(1/V_{P0}^2)$ is uniform (Figure 3.3(a)), a larger fraction of energy scattered by that parameter is recorded by the receivers. Hence, the update in V_{P0} is close to the desired value (9%), although the trade-off between V_{P0} and ϵ results in a slight distortion in the latter parameter (Figure 3.19(c)). The nonlinearity of the inversion (likely at least partially caused by the presence of shear-wave data) manifests itself in the oscillations in the objective function (Figure 3.20). The radiation patterns of $\ln(1/V_{S0}^2)$ (parameterization II) and V_{S0} (parameterization I) are identical, so the shear-wave vertical velocity (e.g., for the model in Figure 3.15) is resolved equally well with both parameterizations.

3.4 Conclusions

Here, we presented a framework for time-domain full-waveform inversion of multicomponent data from elastic VTI media and discussed sensitivity analysis for different model parameteriza-

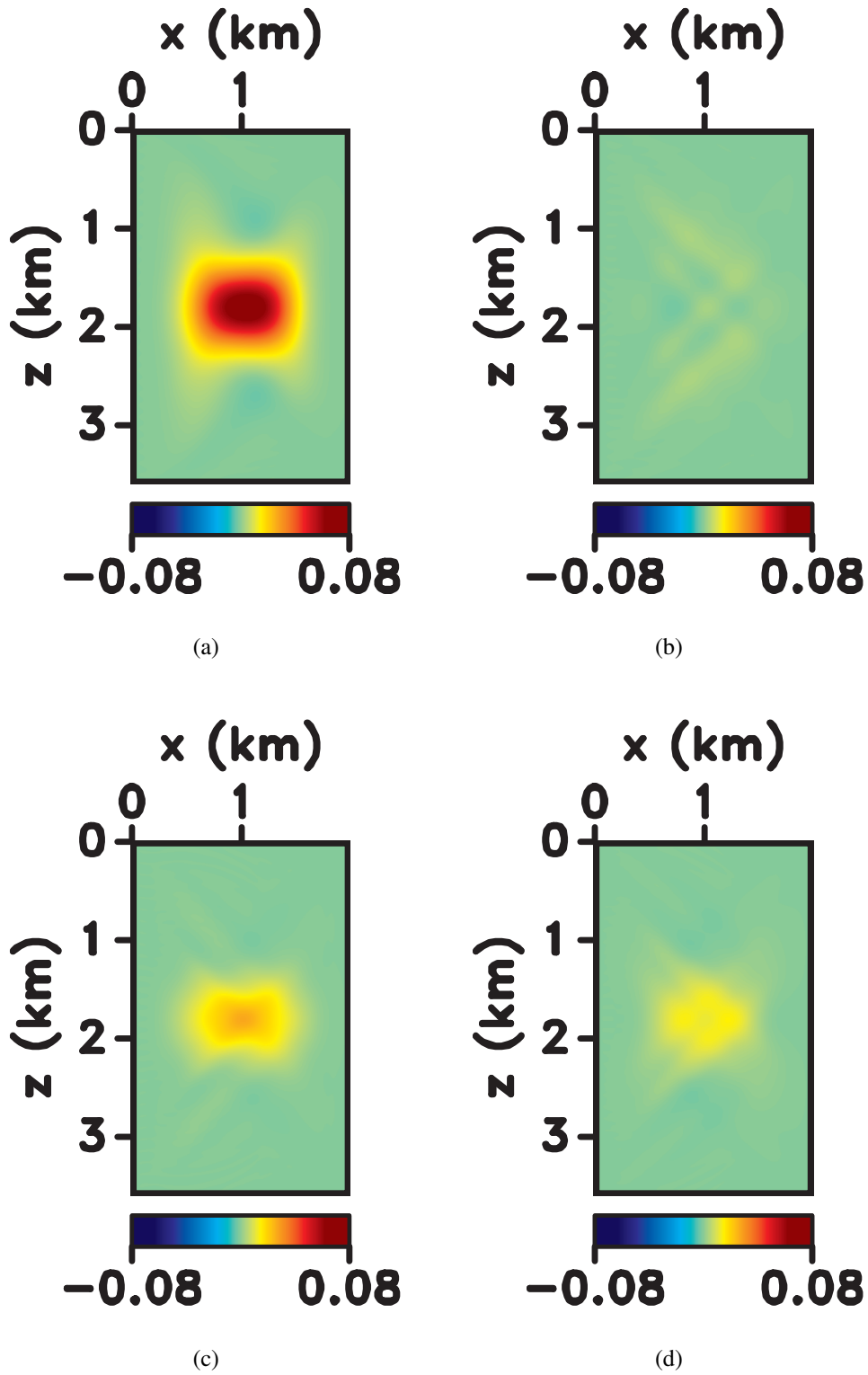


Figure 3.19: Inversion results obtained with parameterization II. Fractional difference between the estimated and initial parameters (a) V_{P0} and (b) V_{S0} for the model from Figure 3.11. The difference between the estimated and initial parameters (c) ϵ and (d) δ for the same model.

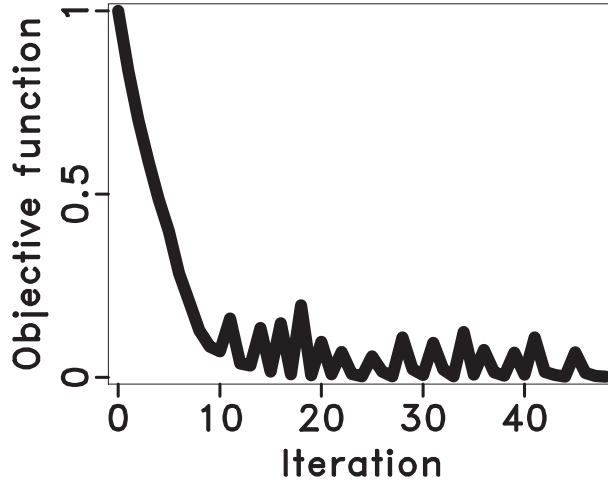


Figure 3.20: Change in the normalized objective function with iterations for the model from Figure 3.11. The function is computed using parameterization II.

tions. The method of Lagrange multipliers was employed to compute the gradient of the objective function with respect to the stiffness coefficients for an arbitrarily anisotropic heterogeneous medium. The gradient expressions were adapted for 2D VTI models, in which the in-plane polarized waves (P and SV) are controlled by combinations of four stiffness coefficients: C_{11} , C_{13} , C_{33} , and C_{55} .

To obtain radiation patterns for different model parameterizations, a point diffractor corresponding to a perturbation in the stiffness coefficients was inserted into a homogeneous isotropic background medium. By employing the Born and WKBJ approximations along with an asymptotic representation of the Green's functions, we derived a general expression for the Fréchet kernel of FWI. This result can be used to evaluate the sensitivity of the elastic FWI to parameters of arbitrarily anisotropic media.

The FWI algorithm and sensitivity analysis were implemented for two VTI model parameterizations. The first includes the P-wave vertical (V_{P0}), NMO (V_{nmo}), and horizontal (V_{hor}) velocities and the S-wave vertical velocity (V_{S0}). Parameterization II operates with the following parameter combinations: $\ln(1/V_{P0}^2)$, $\ln(1/V_{S0}^2)$, $(1 + 2\epsilon)$, and $(1 + 2\delta)$. In both cases, the model parameters have the same order of magnitude, which makes it possible to update all of them using the same

step-length in a given iteration. To gain insight into the potential of each parameterization, we obtained simple explicit expressions for the corresponding radiation patterns of P- and SV-waves.

For parameterization I, the scattered P-wavefield is insensitive to the S-wave velocity V_{S0} , whereas the radiation patterns of V_{P0} and V_{hor} are decoupled. An anomaly in V_{P0} scatters most of the P-wave energy in the vicinity of the symmetry axis, so stable estimation of V_{P0} requires good wavefield sampling in that range of angles. In contrast, a perturbation in V_{hor} produces the largest P-wave scattering near the isotropy (horizontal) plane, which helps estimate V_{hor} (and, therefore, ϵ) in crosshole geometry.

The SV-wavefield is not scattered by the velocity V_{P0} , so transmitted SV-waves cannot be used to invert for the P-wave symmetry-direction velocity. A perturbation in the shear-wave velocity V_{S0} scatters the SV-wave energy uniformly in all directions, thus allowing elastic FWI to recover V_{S0} for any aperture of the experiment. An anomaly in the velocity V_{nmo} predominantly scatters both the P- and SV-wavefields near an angle of 45° , and the scattering amplitude is smaller than that of the other parameters. Hence, transmitted P- and SV-waves do not provide tight constraints on the NMO velocity V_{nmo} , which could be estimated from reflected waves.

For parameterization II, an anomaly in V_{P0} scatters P-wave energy uniformly, whereas the radiation pattern of $1 + 2\epsilon$ has the same shape as that for V_{hor} in parameterization I. Hence, this parameterization makes it possible to recover anomalies not just in ϵ , but also in V_{P0} for crosshole data. As is the case for parameterization I, V_{S0} is well constrained irrespective of the acquisition geometry.

Our results indicate that if the background model is known and the receivers record P- and SV-wave energy in the vicinity of the symmetry axis, FWI of transmission data using parameterization I should resolve the velocities V_{P0} and V_{S0} . In the case of crosshole geometry, multicomponent transmission data inverted with parameterization I constrain ϵ and V_{S0} . The main advantage of parameterization II is a uniform radiation pattern of the velocity V_{P0} , which helps estimate that parameter from crosshole data.

In the employed approximation, the P-wave radiation patterns for elastic VTI media coincide with those for acoustic models. It is impossible, however, to estimate the velocity V_{S0} without including SV-waves. Also, when FWI is applied to more complex models and includes reflection data, the shear wavefield ought to provide tighter constraints on the velocities V_{P0} , V_{nmo} , and V_{hor} . If the wavefield is separated into P- and S-waves, it may be possible to apply a filter based on scattering angles to update a certain parameter (e.g., V_{S0} from shear data) or perform wavenumber filtering, as has been done for acoustic models.

3.5 Acknowledgments

We are grateful to the members of the A(nisotropy) team at CWP, Tariq Alkhalifah (KAUST), and Andreas Rüger (Landmark Graphics) for fruitful discussions. Research reported in this publication was supported by the Consortium Project on Seismic Inverse Methods for Complex Structures at CWP, the CIMMM Project of the Unconventional Natural Gas and Oil Institute (UNGI) at CSM, and competitive research funding from King Abdullah University of Science and Technology (KAUST). The reproducible numeric examples in this paper are generated with the Madagascar open-source software package freely available from <http://www.ahay.org>.

CHAPTER 4

ELASTIC FULL-WAVEFORM INVERSION FOR A SYNTHETIC VTI MODEL FROM VALHALL FIELD

One of the main challenges for full-waveform inversion (FWI) is taking into account both anisotropy and elasticity. Here, we perform FWI for a synthetic 2D elastic VTI (transversely isotropic with a vertical symmetry axis) model based on the geologic section at Valhall field in the North Sea. Multicomponent surface data are generated by a finite-difference code. We apply FWI in the time domain using a multiscale approach with three frequency bands. An approximate inverse Hessian matrix, computed using the L-BFGS-B algorithm, is employed to scale the gradients of the objective function and improve the convergence. In the absence of significant diving-wave energy, the model is updated primarily with reflection data. A horizontal displacement source, which excites intensive shear waves in the conventional offset range, helps provide more accurate updates to the SV-wave vertical velocity, especially in the shallow layers. We test three model parameterizations, which exhibit different radiation patterns and, therefore, create different parameter trade-offs. The choice of parameterization for FWI depends on the availability of long-offset data, the quality of the initial model for the anisotropy coefficients, and the parameter that needs to be resolved with the highest accuracy.

4.1 Introduction

Full-waveform inversion (FWI), as originally proposed by Tarantola (1984b), is designed to estimate an earth model that minimizes the difference between the observed and simulated seismic wavefields. The main advantage of this method is the possibility of achieving high resolution by employing the phase and amplitude information contained in the recorded waveforms.

FWI typically operates with diving-wave energy to update the long-wavelength (or smoothly varying) component of the velocity model. Once an accurate background model has been obtained

using low frequencies, the FWI gradient becomes more sensitive to reflection events, which can help update the reflectivity model and improve the resolution (Bunks et al., 1995).

Most existing FWI algorithms assume the earth model to be isotropic and acoustic (Baeten et al., 2013; Choi and Alkhalifah, 2013; Plessix et al., 2010; Pratt, 1999; Shin and Cha, 2008; Sirgue and Pratt, 2004). Recent advances include methods for mitigating the nonlinearity of the problem (Alkhalifah, 2015b; Choi and Alkhalifah, 2013) and using the entire bandwidth of the data at the same time (Biondi and Almomin, 2014).

When FWI is performed for anisotropic media, it is typically done in the acoustic approximation. Plessix and Cao (2011), Gholami et al. (2013b), and Alkhalifah and Plessix (2014) discuss the sensitivity of the objective function to different parameters of acoustic VTI media. They apply FWI for various combinations of the P-wave vertical (V_{P0}), NMO ($V_{nmo} = V_{P0}\sqrt{1 + 2\delta}$), and horizontal ($V_{hor} = V_{P0}\sqrt{1 + 2\delta}$) velocities and the anisotropy coefficients ϵ , δ , and $\eta = (\epsilon - \delta)/(1 + 2\delta)$. Optimal parameter combinations for FWI depend on acquisition geometry, the data used for the inversion (diving waves or reflection events), and type of inversion (simultaneous or hierarchic). Although the acoustic approximation is computationally efficient, it cannot properly model reflection amplitudes and handle shear- and mode-converted waves.

Lee et al. (2010) perform FWI of synthetic surface data for 2D elastic VTI media but describing the model in terms of the stiffness coefficients leads to ambiguity in their results. Sears et al. (2008) develop a methodology to invert multicomponent OBC (ocean-bottom-cable) data from isotropic elastic media for short and intermediate length-scale P- and S-wave velocities. Application of this approach to FWI of field data recorded at Alba Field, U.K. is presented by Sears et al. (2010). Elastic FWI is employed by Prieux et al. (2013b) to invert hydrophone and OBC data from the Valhall field in the North Sea. Although the modeling operator accounts for anisotropy, the inversion algorithm updates only the P- and S-wave vertical velocities. Vigh et al. (2014) carry out elastic isotropic FWI of a data set from the Gulf of Mexico. Their algorithm operates with pressure records along with the vertical and horizontal displacements recorded in the OBC survey.

Kamath and Tsvankin (2013) perform elastic FWI of multicomponent data from a horizontally layered VTI model. They show that it is possible to estimate the parameters V_{P0} , V_{S0} , ϵ , and δ even for offset-to-depth ratios close to unity, primarily because the algorithm accurately models reflection coefficients. The gradients of the FWI objective function for elastic arbitrarily anisotropic media are derived by Kamath and Tsvankin (2016). They develop a methodology for FWI in 2D elastic VTI media and apply their algorithm to multicomponent data for models with Gaussian anomalies in the Thomsen parameters. Kamath and Tsvankin (2016) also present general expressions for “radiation” (i.e., sensitivity) patterns of model parameters for elastic anisotropic FWI and use this formalism to explain their numerical results for different VTI parameterizations.

Here, we invert multicomponent surface data generated for a 2D elastic VTI model based on the geologic section at Valhall field. First, we review the inversion methodology based on the algorithm of Kamath and Tsvankin (2016). Then we describe the model used to generate the wavefield and the processing steps applied to the simulated data. A multiscale approach is employed to perform FWI in three frequency bands. We discuss the inversion results obtained for different model parameterizations and explain them in terms of the radiation (sensitivity) patterns.

4.2 Methodology

Here, we describe the strategy adopted for inversion, and the processing applied to the data generated for the synthetic model.

4.2.1 Inversion methodology

We carry out FWI in the time domain by minimizing the following objective function:

$$\mathcal{F} = \frac{1}{2} \sum_{r=1}^N \|\mathbf{u}(\mathbf{x}_r, t) - \mathbf{d}(\mathbf{x}_r, t)\|^2, \quad (4.1)$$

where N is the number of receivers, $\mathbf{u}(\mathbf{x}_r, t)$ is the displacement computed for a trial model at receiver location \mathbf{x}_r , and $\mathbf{d}(\mathbf{x}_r, t)$ is the recorded displacement. Summation over shots is implied. The gradient of \mathcal{F} with respect to the stiffness coefficients c_{ijkl} is obtained using the adjoint-state

method (Kamath and Tsvankin, 2016):

$$\frac{\partial \mathcal{F}}{\partial c_{ijkl}} = - \int_0^T \frac{\partial u_i}{\partial x_j} \frac{\partial \psi_k}{\partial x_l} dt, \quad (4.2)$$

where \mathbf{u} and ψ are the forward and adjoint displacement fields, respectively. The gradient for a chosen model parameter m_n can be found as:

$$\frac{\partial \mathcal{F}}{\partial m_n} = \sum_{ijkl} \frac{\partial \mathcal{F}}{\partial c_{ijkl}} \frac{\partial c_{ijkl}}{\partial m_n}. \quad (4.3)$$

Here, we define the model using three different parameter sets. Parameterization I (Kamath and Tsvankin, 2013) includes the velocities V_{P0} , V_{S0} , V_{nmo} , and V_{hor} ; parameterization II consists of the squared velocities V_{nmo}^2 and V_{S0}^2 , $(1 + 2\eta)$, and $(1 + 2\delta)$; parameterization III is a combination of the squared velocities V_{hor}^2 and V_{S0}^2 , $(1 + 2\eta)$, and $(1 + 2\epsilon)$. The last two parameter sets were suggested and analyzed for acoustic VTI media by Alkhalifah and Plessix (2014). The velocities in parameterizations II and III are normalized by the squares of the respective initial values, which makes the corresponding parameters dimensionless and reduces them to same order of magnitude as the anisotropy coefficients. Including density as a model parameter makes the objective function highly nonlinear (e.g., Kamath and Tsvankin, 2013), so here we fix density at the actual value.

The 2D elastic finite-difference modeling code from the Madagascar package is used to generate the data. To obtain the model update at each iteration, the gradient is scaled by a factor which can be chosen in different ways. In the widely used steepest-descent method, the scaling factor is set equal to the step length, which does not account for the energy loss due to geometric spreading. In the absence of a Hessian term (or its approximation), the gradient is too large near the sources and receivers, which complicates velocity estimation. Therefore, the gradients at the source and receiver locations have to be masked to ensure meaningful model updates. In addition, the steepest-descent technique could produce slow convergence if the objective function has a long and narrow “valley.”

The problems associated with the steepest-descent algorithm can be circumvented by applying the Gauss-Newton method and computing the model update $\Delta\mathbf{m}$ from

$$\Delta\mathbf{m} = [\mathcal{H}]^{-1} \mathbf{G}, \quad (4.4)$$

where \mathcal{H} is the Hessian operator and \mathbf{G} is the gradient of the objective function. Computation of the Hessian, however, is extremely expensive. The Broyden-Fletcher-Goldfarb-Shanno (BFGS) algorithm or its low-memory equivalent (L-BFGS) are often used to obtain an approximate Hessian. We employ the L-BFGS-B (bounded) package of Byrd et al. (1995) to compute the operator \mathcal{H} and update the model from equation 4.4.

4.2.2 Synthetic model and data processing

The synthetic model used here is based on the parameters estimated for Valhall field in the North Sea (Munns, 1985). The V_{P0} -field (Figure 4.1(a)) includes low-velocity gas layers above the reservoir, which is located at a depth of 2.5 km. The original model is sampled every 3.125 m in the horizontal and vertical directions. However, to reduce computational time in the finite-difference modeling, the grid spacing here is increased to 20 m. Although the original Valhall model has a water column on top, we make the entire section elastic and clip the shear-wave velocity V_{S0} so that its minimum value near the surface is 700 m/s.

Multicomponent synthetic data are generated by a horizontal array of vertical and/or horizontal displacement sources placed with an 80 m increment at a depth of 20 m. The receivers are located at every grid point at the same depth (20 m). The source signal is a Ricker wavelet with a peak frequency of 3.5 Hz.

To better understand the wavefield, we shoot a fan of rays from two source locations using a VTI ray-tracing program (`sfrays2a`) in Madagascar (Figure 4.2). Most of the P-wave diving-wave energy is limited to depths down to 1.5 km, although shots at the edges of the survey produce diving waves that penetrate down to about 2.5 km. In addition to diving waves, we record reflections from the shallow gas layers, which should allow us to achieve relatively high spatial resolution

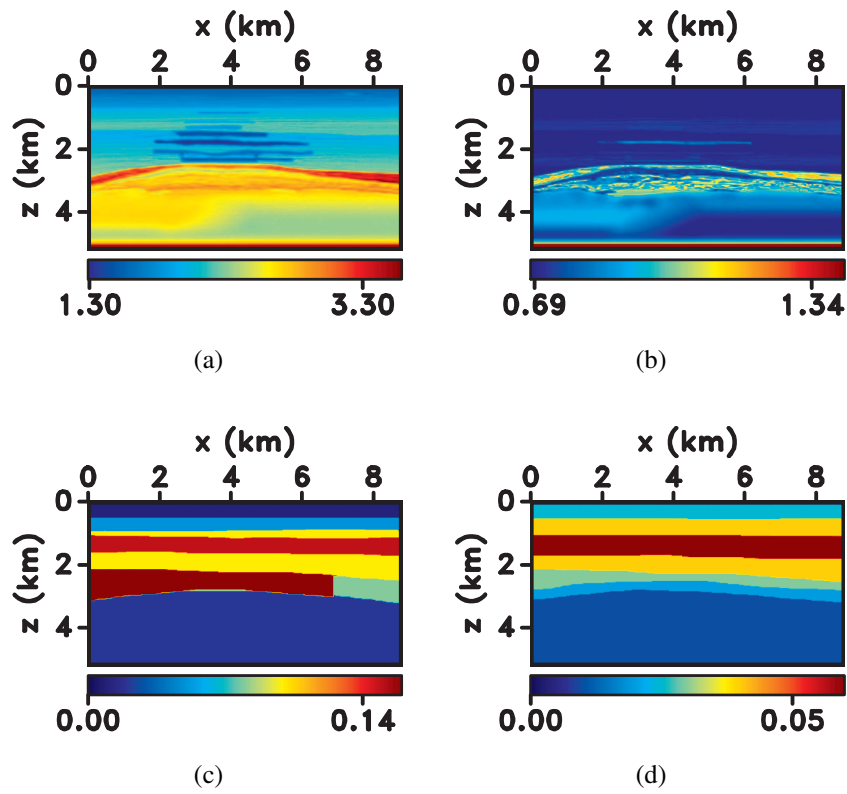


Figure 4.1: Parameters (a) V_{P0} , (b) V_{S0} , (c) ϵ , and (d) δ of a synthetic model based on sections from the Valhall field. The velocities here and in the subsequent plots have units of km/s.

for the top 1.5 km of the section. The laterally extended model in Gholami et al. (2013a) makes it possible to acquire diving waves from the layer immediately above the reservoir, where our model produces only reflections.

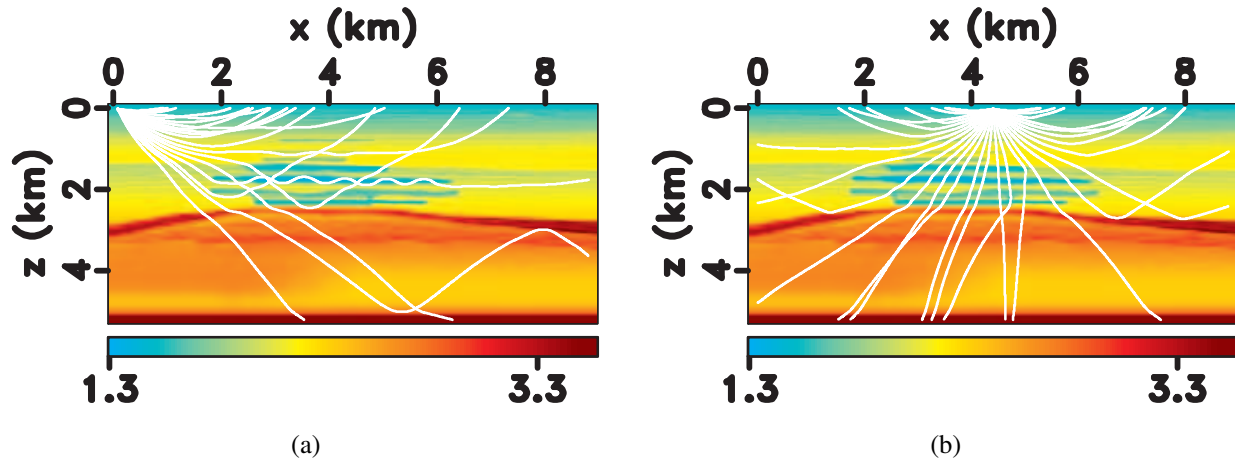


Figure 4.2: Fans of rays from sources at (a) $x=0$ km and (b) $x=4.4$ km superimposed on the actual V_{P0} -field.

The actual fields of the velocities V_{P0} , V_{S0} , V_{nmo} , and V_{hor} are smoothed to generate the initial model for FWI using parameterization I (Figure 4.3). The initial models for parameterizations II and III are computed from the initial velocities. The vertical variation of the actual coefficient δ is much smoother than that of ϵ , which has large jumps at depths of 1.7 km and 2.2 km. Hence, the difference between the initial and actual ϵ - and η -fields reaches maximum values of about 0.08 (Figure 4.4(e) and Figure 4.4(g), respectively), whereas the initial δ is more accurate. However, the average initial ϵ -, η -, and δ -fields are relatively close to the actual model.

The L-BFGS-B implementation requires putting bounds on the model parameters, so each velocity is bounded by its minimum and maximum values for the actual model. As mentioned above, FWI is applied with the actual density field. We carry out the inversion using a multiscale approach with the following frequency bands: 0 – 1.5 Hz, 0 – 3 Hz, and 0 – 5 Hz. The inversion results for each frequency band provide the initial models for the next band. For this range of frequencies, FWI is unlikely to resolve some high-resolution features of the actual velocity fields

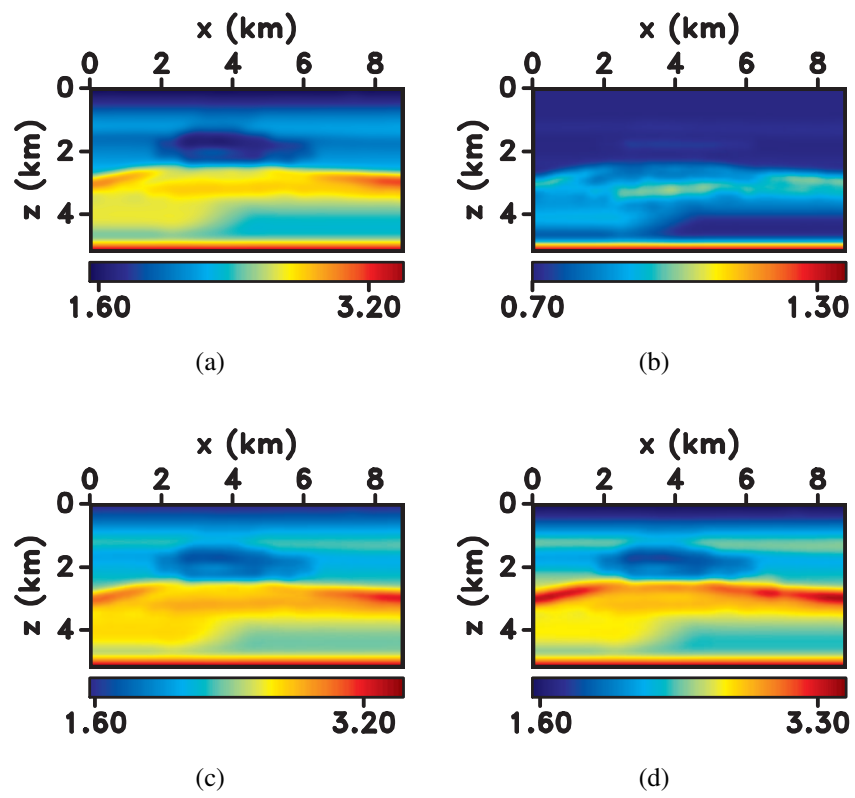


Figure 4.3: Initial model for the velocities (a) V_{P0} , (b) V_{S0} , (c) V_{nmo} , and (d) V_{hor} .

(Figure 4.4(a) to Figure 4.4(d)). Although including higher frequencies should improve resolution, we restrict the frequency range to reduce the computational cost.

4.3 Numerical tests

Here, we discuss FWI results obtained for three model parameterizations.

4.3.1 Parameterization I

The first test is performed for parameterization I with the wavefield generated by a vertical displacement source. Figure 4.5–Figure 4.7 illustrate the improvement in data fit between the initial and inverted models for each frequency band. As expected, the wavenumber content of the inverted models increases with inclusion of higher temporal frequencies in the data.

Figure 4.8(b) indicates that the shallow-gas layers are generally well delineated in the updated V_{P0} -field. However, lack of frequencies above 5 Hz in the data limits the spatial resolution of the inverted V_{P0} and results in errors at depths of about 1.2 km, 2.2 km, and 2.5 km (Figure 4.9(a)). The relatively low amplitude of shear waves produced by a vertical source does not allow the algorithm to properly update V_{S0} (Figure 4.8(e) and Figure 4.9(b)). Although the inverted velocity V_{nmo} matches the trend of the actual curve more closely than the initial model (Figure 4.9(c)), the spatial resolution in V_{nmo} is lower than that for V_{P0} , with noticeable deviations at depths of 1.2 km, 1.5 km, 2.2 km, and 2.5 km. The low-frequency trend of the V_{hor} -field, especially at depths of 1.5 km, 1.8 km, 2 km, and 2.2 km, matches well with the actual curve (Figure 4.9(d)).

The P-wave radiation patterns of the model parameters (Figure 4.10(a)) can help explain the obtained results (Kamath and Tsvankin, 2016). A V_{P0} -anomaly on a horizontal reflector scatters P-wave energy mostly near the vertical symmetry axis, which results in a relatively high vertical resolution of the updated V_{P0} -field (Wu and Toksöz, 1987). In the case of an anomaly in V_{hor} , most of the energy is scattered near the horizontal isotropy plane, which explains why the updates in the horizontal velocity are mostly confined to the middle part of the model probed by large-angle reflections. Diving waves and large-angle reflections are largely responsible for long-wavelength updates, whereas conventional-offset reflections improve the spatial resolution of the model (Wu

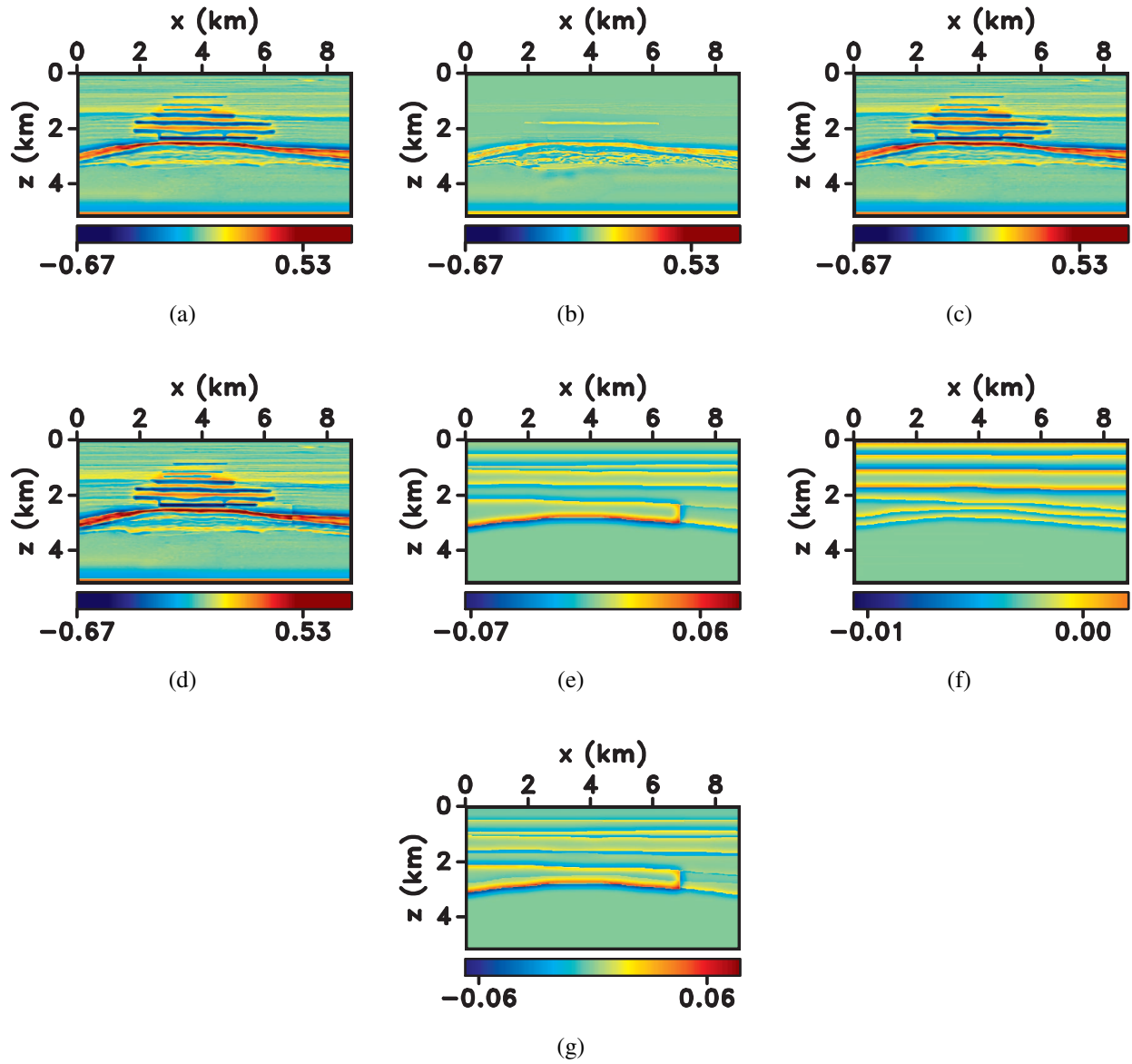


Figure 4.4: Difference between the actual and initial models: (a) V_{P0} , (b) V_{S0} , (c) V_{nmo} , (d) V_{hor} , (e) ϵ , (f) δ , (g) η .

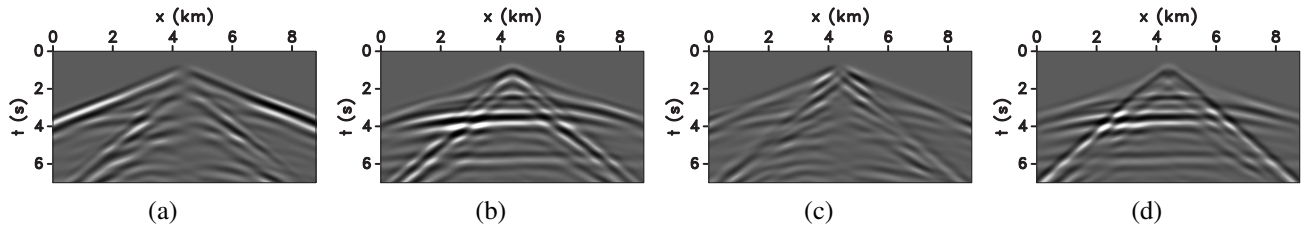


Figure 4.5: (a) Horizontal and (b) vertical displacement components of the difference between the observed data and those computed for the initial model in the 0 – 1.5 Hz frequency range. The (c) horizontal and (d) vertical components of the difference between the observed data and those computed for the inverted model. The data are generated by an array of vertical displacement sources.

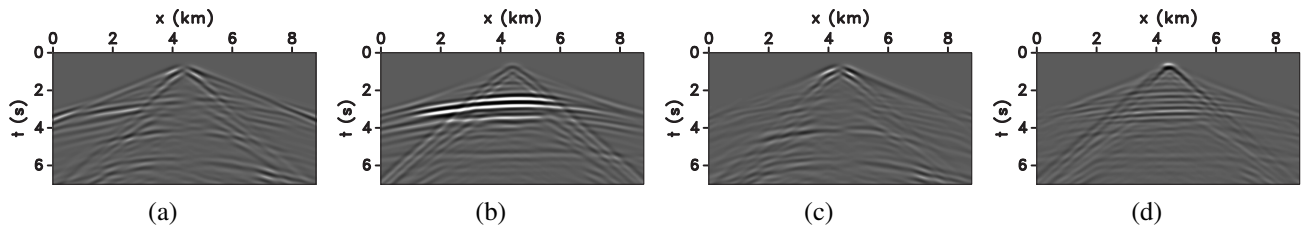


Figure 4.6: (a) Horizontal and (b) vertical displacement components of the difference between the observed data and those computed for the initial model in the 0 – 3 Hz frequency range. The (c) horizontal and (d) vertical components of the difference between the observed data and those computed for the inverted model.

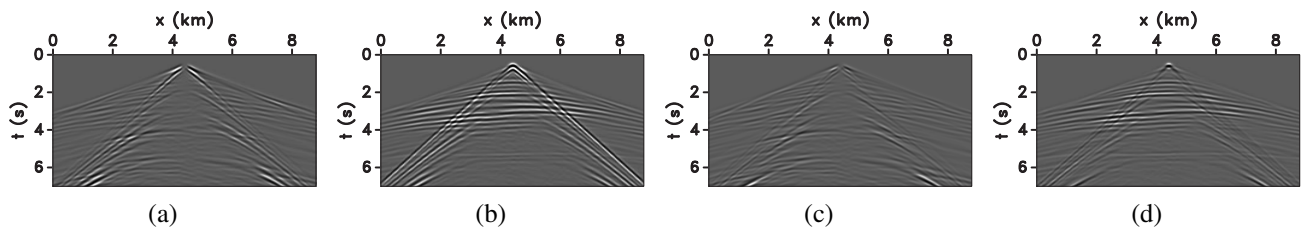


Figure 4.7: (a) Horizontal and (b) vertical displacement components of the difference between the observed data and those computed for the initial model in the 0 – 5 Hz frequency range. The (c) horizontal and (d) vertical components of the difference between the observed data and those computed for the inverted model.

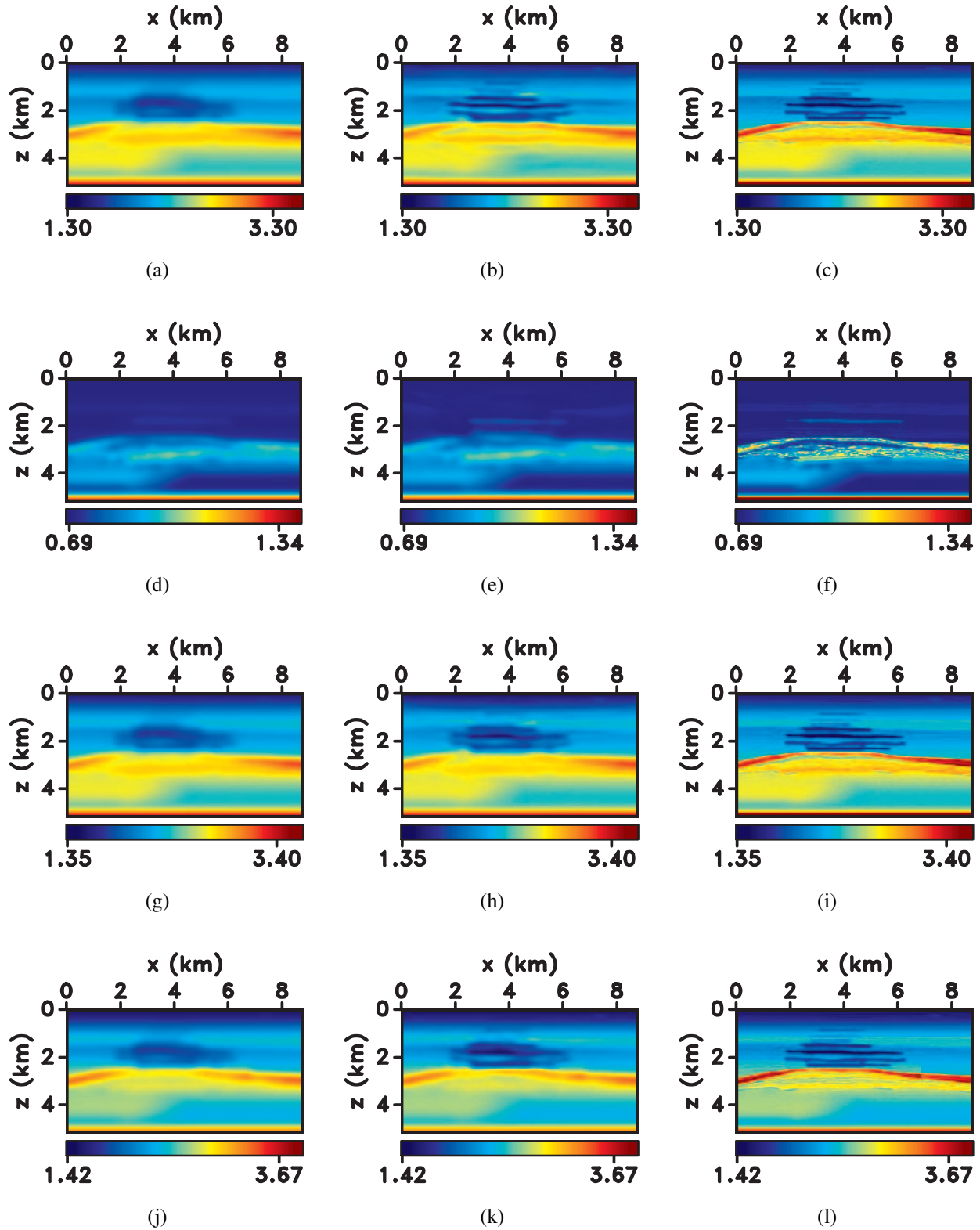


Figure 4.8: Initial (left column), updated (middle column), and actual (right column) models for FWI performed using parameterization I. (a), (b), (c) correspond to V_{P0} , (d), (e), (f) to V_{S0} , (g), (h), (i) to V_{nmo} and (j), (k), (l) to V_{hor} .

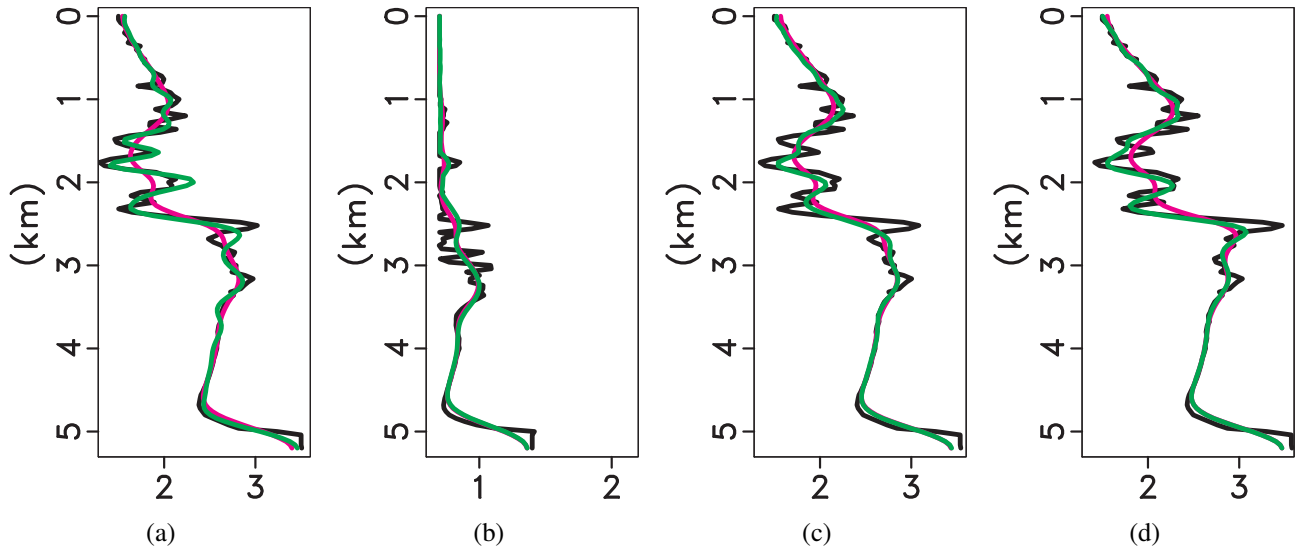


Figure 4.9: Actual (black), initial (magenta), and inverted (green) velocities for parameterization I: (a) V_{P0} , (b) V_{S0} , (c) V_{nmo} , and (d) V_{hor} . The data were generated by an array of vertical displacement sources. The profiles here and in the subsequent plots are displayed at location $x = 3.5$ km

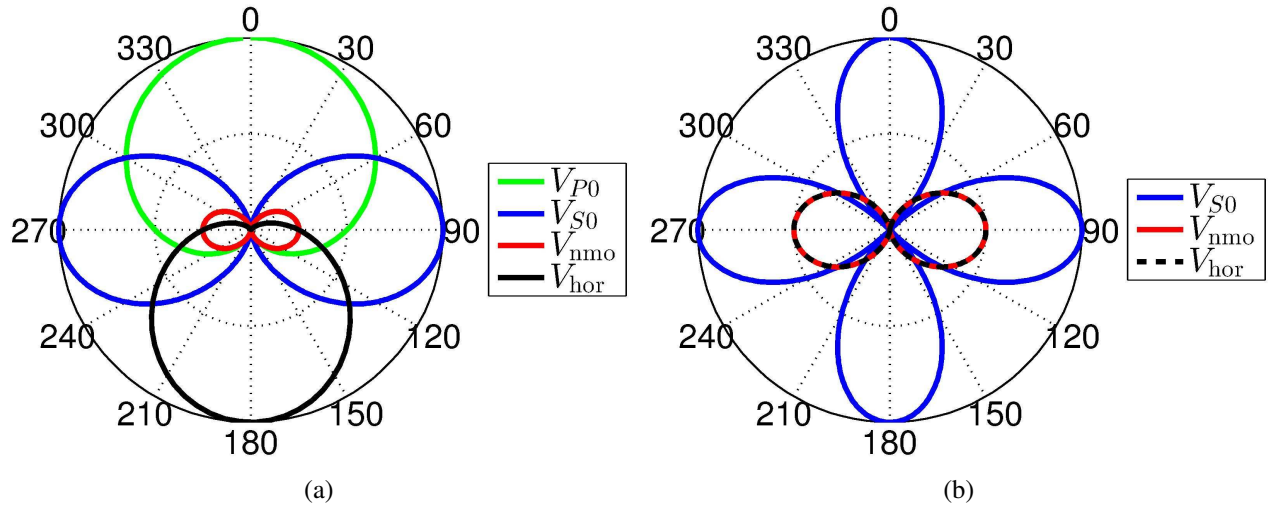


Figure 4.10: (a) P- and (b) SV-wave radiation patterns obtained with parameterization I for reflections from a horizontal interface. The patterns here and in the subsequent plots are computed as functions of the opening angles at the diffractor with the background $V_P/V_S = 2$.

and Toksöz, 1987). The resolution provided by diving waves (typically on the order of wavelength) is, however, higher than that obtained from reflection or traveltime tomography, in which the resolution is limited by the first Fresnel zone (Williamson, 1991). Overall, the velocity V_{hor} is estimated with a higher accuracy compared to V_{nmo} but has a lower spatial resolution than V_{P0} and V_{nmo} .

The maximum energy of P-waves scattered by a V_{nmo} -anomaly (Figure 4.10) is only about 25% of that for V_{P0} , and is focused at opening angles near 90° (which correspond to incidence angles of about 45°). Therefore, the algorithm cannot update V_{nmo} at depths below 2.4 km. Scattering by an anomaly in V_{S0} has a pattern similar to that in V_{nmo} , which causes a trade-off between the two velocities. The radiation patterns in Figure 4.10, Figure 4.13, and Figure 4.20 assume a background V_P/V_S -ratio of two, for which the energy scattered by an anomaly in V_{S0} is higher than that for V_{nmo} . However, for the model used in this paper, the V_{P0}/V_{S0} -ratio reaches values of up to three between the depths of 0.5 km and 2.5 km. The increase in the V_{P0}/V_{S0} -ratio reduces the magnitude of the V_{S0} -radiation pattern, which leads to a more significant trade-off between V_{S0} and V_{nmo} and inaccurate updates in V_{S0} from the P-wavefield. Based on the S-wave radiation patterns (Figure 4.10(b)), we expect significant updates in the V_{S0} -field from both near- and far-offset shear-wave data. However, a vertical displacement source does not generate intensive shear waves in the recorded offset range, which suppresses updates in V_{S0} .

One of the advantages of parameterization I is insignificant trade-off between V_{P0} and V_{hor} . The P-wave radiation patterns (Figure 4.10(a)) suggest that near-offset data are largely responsible for updating the V_{P0} -field, whereas long-offset data and diving waves should help constrain V_{hor} . However, the inversion results for V_{hor} are satisfactory only in the shallow region (above 2 km), for which the offset-to-depth ratio is sufficiently large. Hence, if long-offset data (with the offset-to-depth ratio of two or more) are available, diving waves can be inverted for an accurate low-wavenumber V_{hor} -field. In the deeper layers, the estimates of V_{hor} and the parameter ϵ (obtained from the relation $V_{\text{hor}} = V_{P0} \sqrt{1 + 2\epsilon}$) are unsatisfactory. Likewise, the updates in V_{nmo} have a lower magnitude and vertical resolution compared to those in V_{P0} , thereby resulting in the distorted

δ -field computed from the equation $V_{\text{nmo}} = V_{P0} \sqrt{1 + 2\delta}$.

Overall, parameterization I helps resolve the P-wave vertical velocity V_{P0} , but the other Thomson parameters for our synthetic survey are not well-constrained. There is no trade-off between V_{P0} and the other velocities for relatively small opening angles, which ensures accurate V_{P0} -updates. Hence, if only conventional-offset data (with the maximum offset-to-depth ratio close to unity) are available, it is advantageous to invert for V_{P0} using parameterization I.

Next, we perform FWI for data generated with an oblique displacement source, whose vertical and horizontal components are equal. Such a source generates more intensive shear waves in the recorded offset range, which results in better updates for the V_{S0} -field, especially in the 1 – 1.5 km depth range (Figure 4.11(e)). The SV-wave radiation patterns for anomalies in V_{nmo} and V_{hor} are identical; both have trade-offs with V_{S0} for intermediate opening angles (Figure 4.10(b)). This causes insufficiently large updates in the velocities V_{nmo} and V_{hor} (compare Figure 4.9 and Figure 4.12) at depths of 1.8 km and 2.2 km, and incorrect updates in V_{S0} at 2.2 km. However, for depths down to 1.8 km, the 45°-rotation of the source produces an improvement in all four inverted velocities. Overall, intensive shear waves bring in more information and help resolve the V_{S0} -field, but also create additional trade-offs for parameterization I. Still, to exploit the shear-wave information, the oblique source is employed in all tests for the other two parameterizations.

4.3.2 Parameterization II

Next, we perform the inversion using parameterization II, which includes V_{nmo}^2 , V_{S0}^2 , $(1 + 2\eta)$, and $(1 + 2\delta)$; the squared velocities are normalized by the respective initial values. The P-wave radiation pattern of an anomaly in V_{nmo} is “isotropic” (Figure 4.13(a)), with energy scattered over the full range of angles. Plessix and Cao (2011) employ the combination $(V_{\text{nmo}}, \eta, \text{ and } \delta)$ for FWI in acoustic VTI media and demonstrate that V_{nmo} is the most tightly constrained of the three parameters, whereas estimates of η and δ are hampered by large null-spaces. The radiation patterns exhibit trade-offs between V_{nmo} and δ for small opening angles and between V_{nmo} and η for large angles (Figure 4.13(a)).

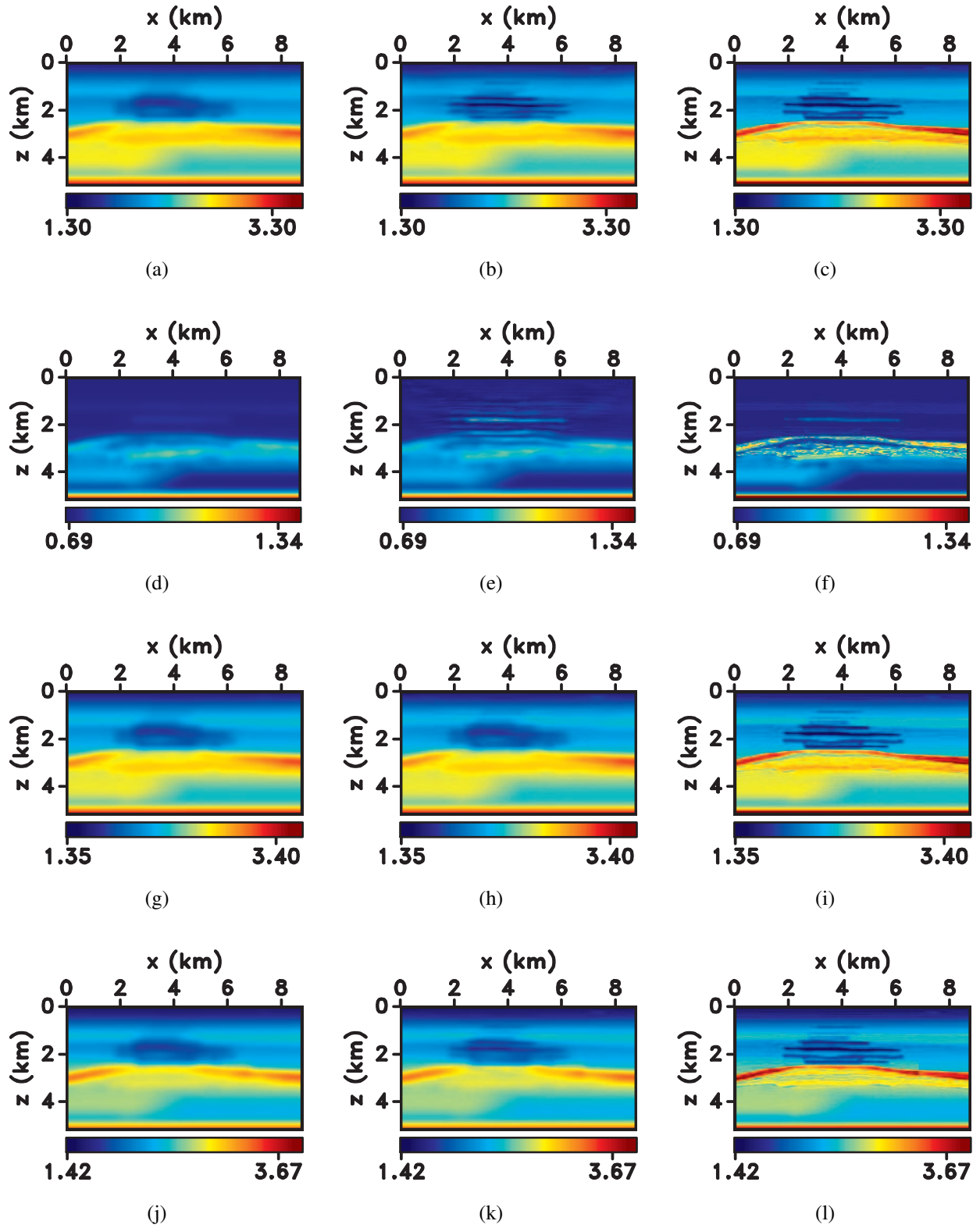


Figure 4.11: Initial (left column), inverted (middle column), and true (right column) models for FWI performed using parameterization I. (a), (b), (c) correspond to V_{P0} , (d), (e), (f) to V_{S0} , (g), (h), (i) to V_{nmo} and (j), (k), (l) to V_{hor} . The data here and in the subsequent plots are generated by an array of oblique displacement sources. 73

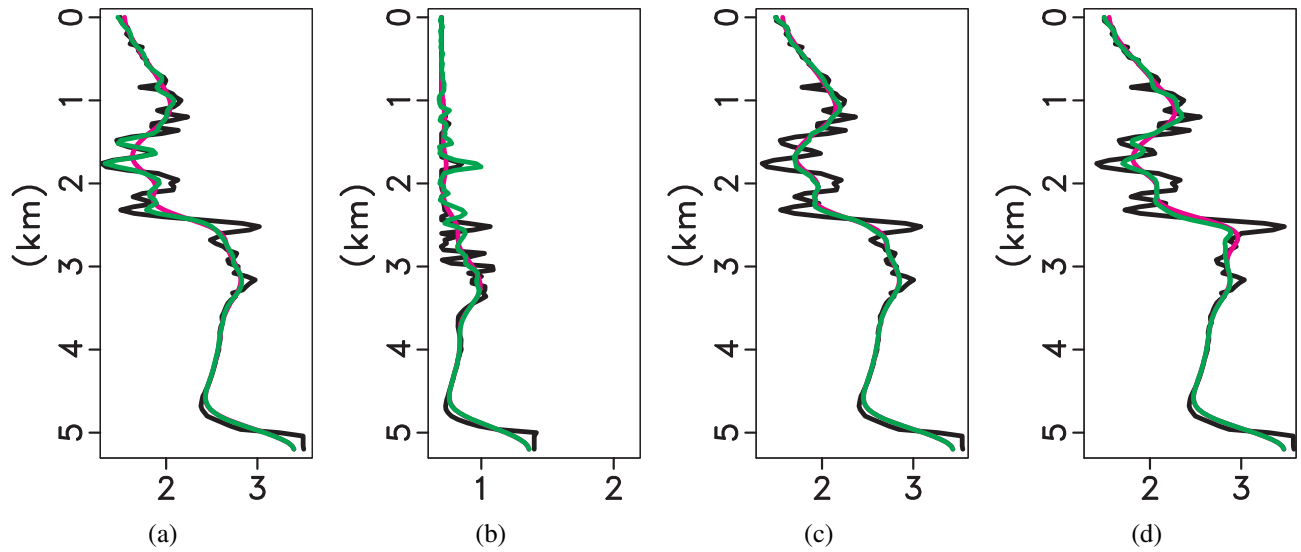


Figure 4.12: Actual (black), initial (magenta), and inverted (green) velocities for parameterization I: (a) V_{P0} , (b) V_{S0} , (c) V_{nmo} , and (d) V_{hor} .

The P- and SV-wave radiation patterns for V_{S0} are similar to those for parameterization I. The SV-wave radiation patterns (Figure 4.13(b)) indicate trade-offs between V_{S0} and η for intermediate opening angles (incidence angles of around 45°). The updates in the V_{S0} -field are accurate down to a depth of 2 km (Figure 4.15(b)), which indicates that the objective function is more sensitive to the velocity V_{S0} than the coefficient η .

A purely isotropic P-wave radiation pattern for V_{nmo} combined with a higher sensitivity to this velocity makes parameterization II most suitable for estimating this parameter from data recorded for a wide offset range. Indeed, employing parameterization II results in a marked improvement (compared to parameterization I) in the V_{nmo} -field. At depths of 1.2 km, 2.2 km, and 2.5 km (Figure 4.15(a)), the inverted V_{nmo} matches the actual values better than for parameterization I. Because the initial η - and δ -fields are relatively close to the actual models, the updates in both anisotropy coefficients are insignificant (Figure 4.15(c) and Figure 4.15(d)). An accurate inverted V_{nmo} -field combined with just slightly distorted anisotropy coefficients yields good estimates of the velocities V_{P0} and V_{hor} . The V_{P0} -profile (Figure 4.16(a)) matches the true values at depths of 1.2 km, 2.2 km, and 2.5 km even more closely than for parameterization I (Figure 4.9(a)).

Figure 4.16(d) illustrates an improvement in the spatial resolution of the inverted V_{hor} -field as well (compare with Figure 4.9(d) at depths of 1.2 km, 1.7 km, 2.2 km, and 2.5 km).

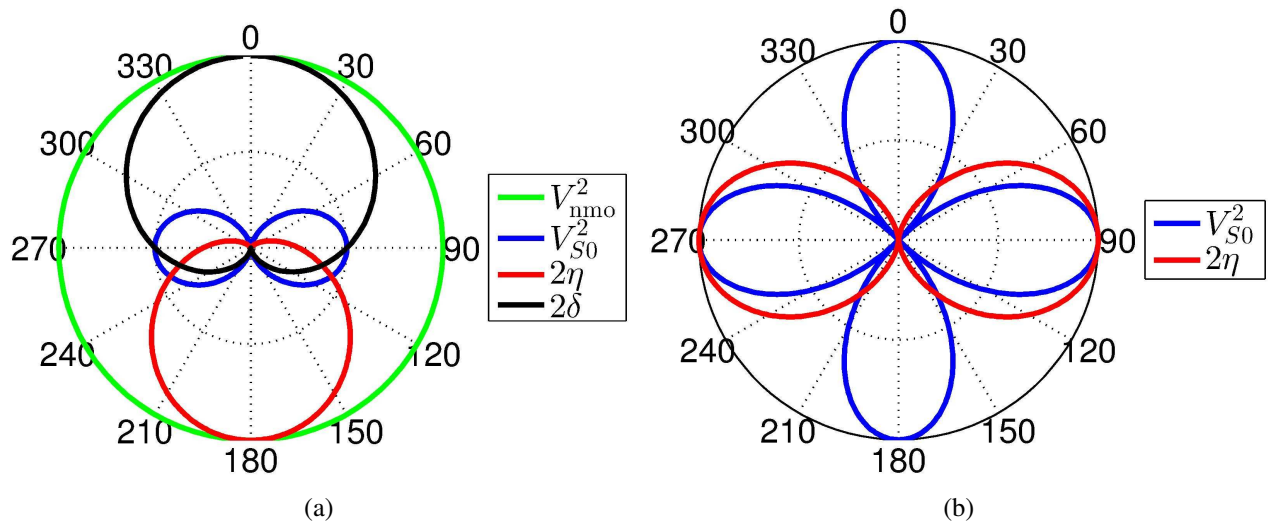


Figure 4.13: (a) P- and (b) SV-wave radiation patterns obtained with parameterization II for reflections from a horizontal interface.

Migration velocity analysis in VTI media can recover smooth fields of V_{nmo} and η (or V_{hor} e.g., Tsvankin, 2012), but errors in the parameter δ are typically higher. Hence, next we add a constant value of 0.1 to the initial δ -field used before (Figure 4.17(j)). Such an overestimated δ yields understated initial velocities V_{P0} which move the imaged reflectors up toward the surface. In this parameterization, V_{P0} is not updated directly; also, the updates in the anisotropy coefficients η and δ remain relatively small (Figure 4.18(c) and Figure 4.18(d), respectively). Consequently, the estimated V_{nmo} - and V_{hor} -fields (Figure 4.19(c) and Figure 4.19(d), respectively) are shifted vertically with respect to the actual model. Therefore, parameterization II should be useful in cases when not only a wide range of offsets is recorded, but also prior estimates of the η - and δ -fields are sufficiently accurate.

4.3.3 Parameterization III

Finally, the inversion is carried out for parameterization III [V_{hor}^2 , V_{S0}^2 , $(1 + 2\eta)$, and $(1 + 2\epsilon)$], with the squared velocities normalized by their initial values. The P- and SV-wave radiation pat-

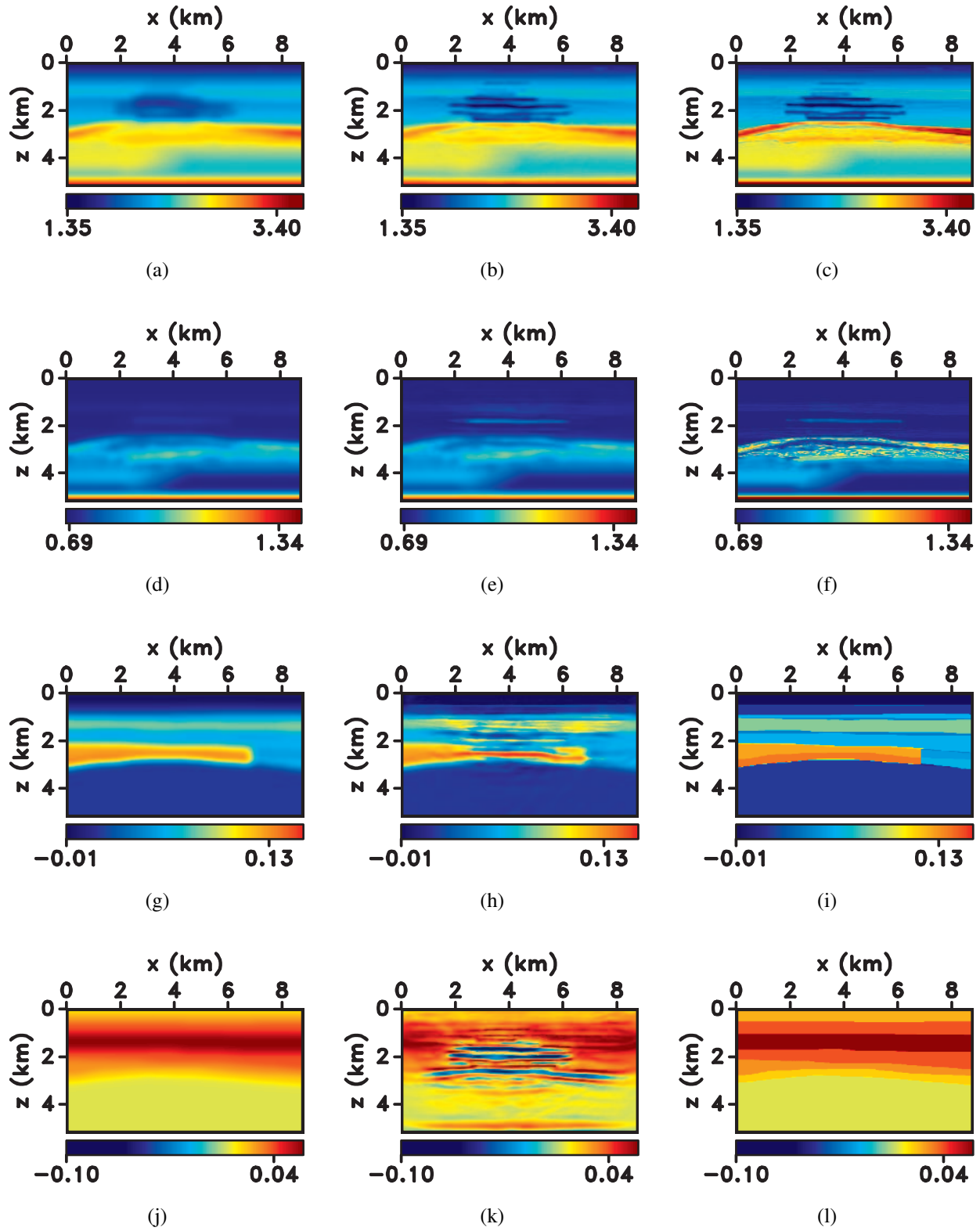


Figure 4.14: Initial (left column), inverted (middle column), and actual (right column) models for FWI performed using parameterization II. (a), (b), (c) correspond to V_{nmo} , (d), (e), (f) to V_{s0} , (g), (h), (i) to η and (j), (k), (l) to δ .

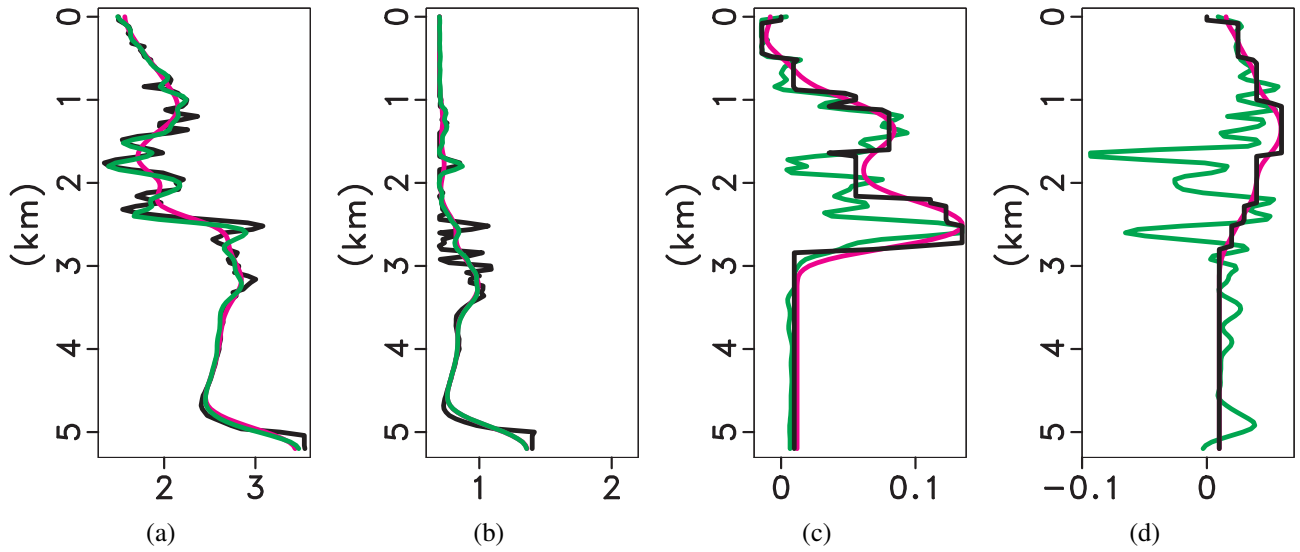


Figure 4.15: Actual (black), initial (magenta), and inverted (green) parameters for parameterization II: (a) V_{nmo} , (b) V_{S0} , (c) η , and (d) δ .

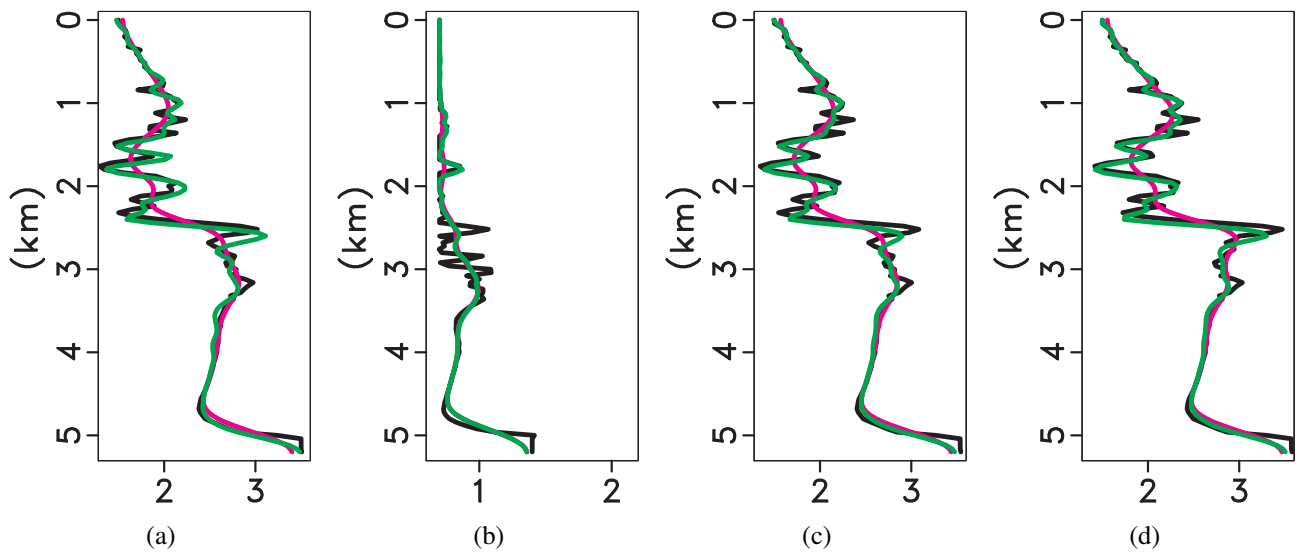


Figure 4.16: Actual (black), initial (magenta), and inverted (green) velocities for parameterization II: (a) V_{P0} , (b) V_{S0} , (c) V_{nmo} , and (d) V_{hor} .

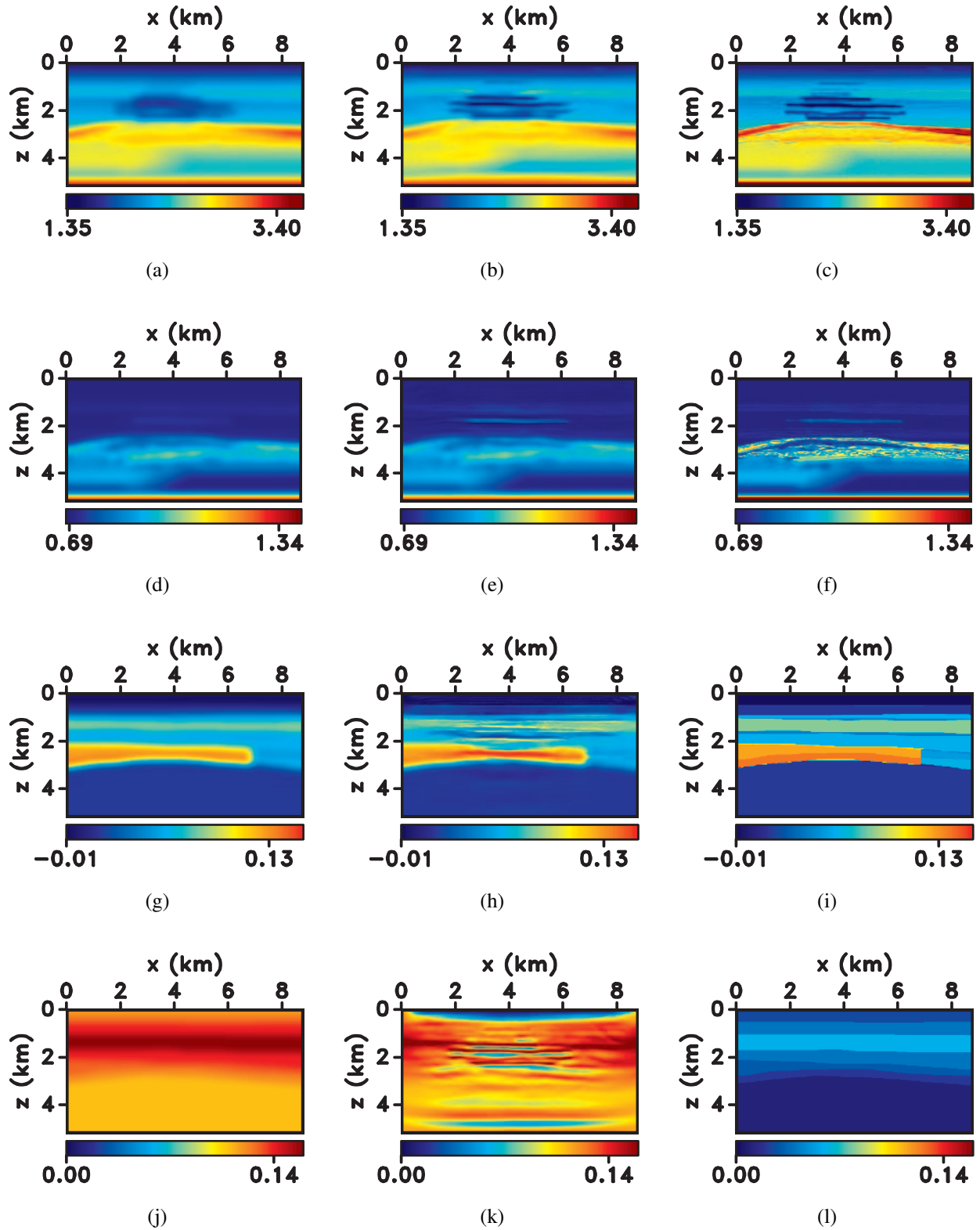


Figure 4.17: Initial (left column), inverted (middle column), and actual (right column) models for FWI performed using parameterization II. (a), (b), (c) correspond to V_{nmo} , (d), (e), (f) to V_{S0} , (g), (h), (i) to η and (j), (k), (l) to δ . The initial δ here is obtained by adding a constant value of 0.1 to the δ -field from Figure 4.14(j).

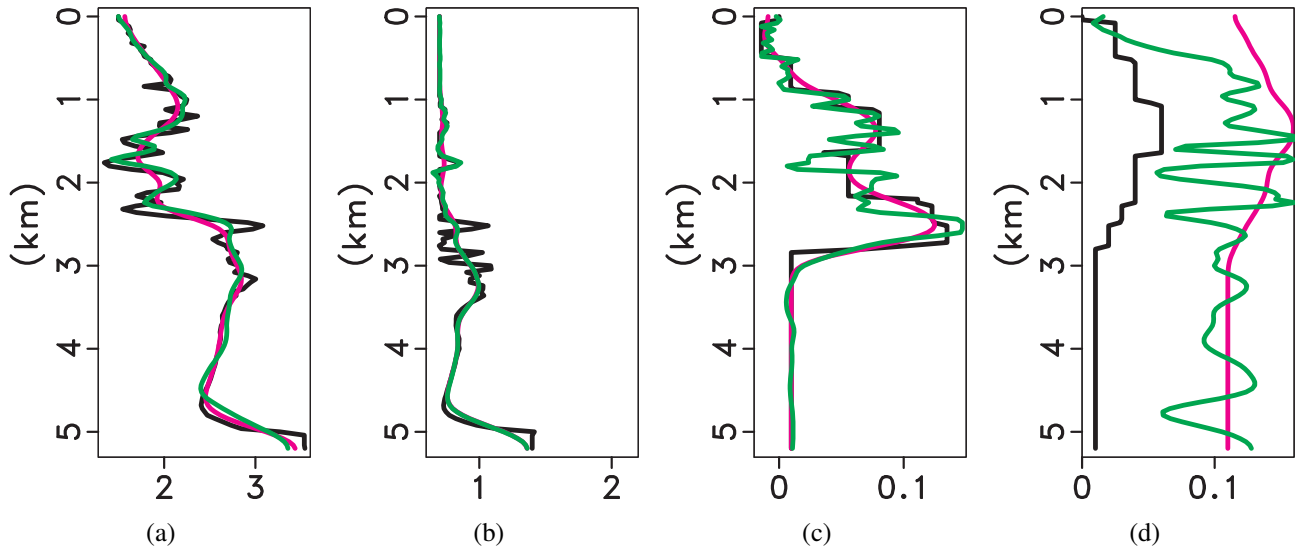


Figure 4.18: Actual (black), initial (magenta), and inverted (green) parameters for parameterization II: (a) V_{nmo} , (b) V_{S0} , (c) η , and (d) δ . Inversion is performed for the distorted initial δ from Figure 4.17(j).

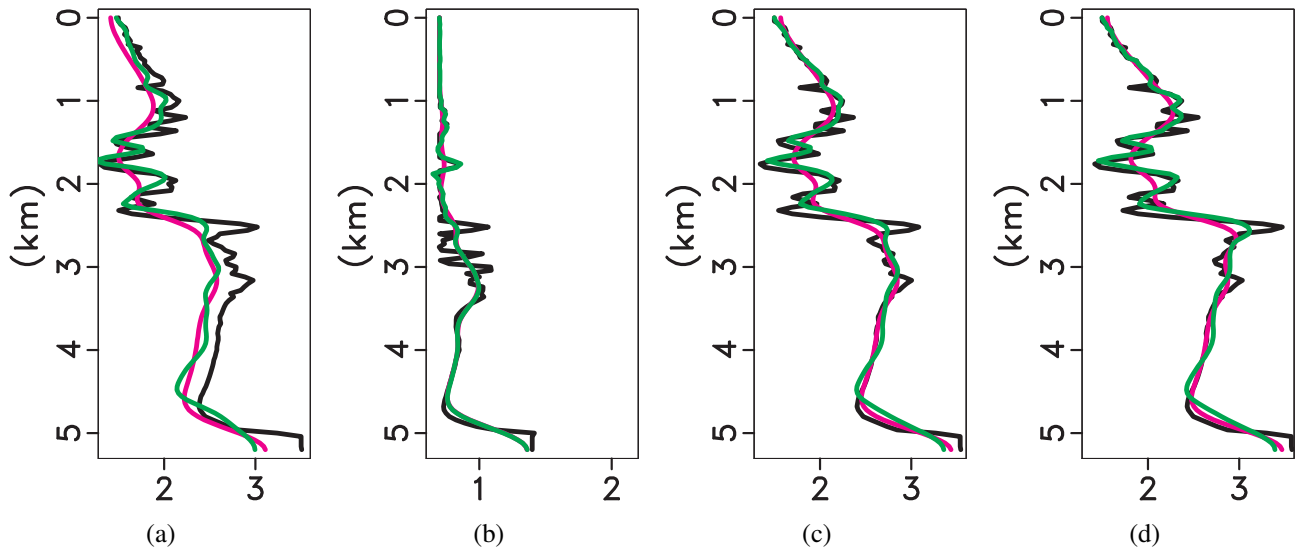


Figure 4.19: Actual (black), initial (magenta), and inverted (green) velocities for parameterization II: (a) V_{P0} , (b) V_{S0} , (c) V_{nmo} , and (d) V_{hor} . Inversion is performed for the distorted initial δ from Figure 4.17(j).

terns for an anomaly in V_{S0} are similar for all three parameterizations, and the SV-wave pattern for η coincides with that for parameterization II. For parameterization III, the velocity V_{hor} has a purely isotropic P-wave radiation pattern (Figure 4.20(a)), which was the case for V_{nmo} in parameterization II. Trade-offs exist between V_{hor} and ϵ for small opening angles, and between V_{hor} and η for intermediate opening angles (which correspond to incidence angles close to 45°). Because V_{hor} has no trade-offs with any other parameter for large opening angles, diving waves can be employed to accurately update the long-wavelength V_{hor} -field (Alkhalifah, 2015a).

In agreement with the results of Alkhalifah (2015a) for acoustic media, for this parameterization V_{hor} is the best constrained parameter (Figure 4.21(b) and Figure 4.22(a)). The updates in the η - and ϵ -fields, which are relatively close to the actual values to begin with, are insignificant (Figure 4.22(c) and Figure 4.22(d), respectively). The inverted V_{hor} -field is similar to that obtained with parameterization II (compare Figure 4.23(d) and Figure 4.16(d)). In addition, because the values of η and ϵ are fairly accurate, the V_{P0} - and V_{nmo} -fields estimated from V_{hor} and the anisotropy coefficients are also well resolved and resemble those for parameterization II. A distorted initial ϵ -field computed from the erroneous δ -model in Figure 4.17(j) yields the inverted velocities V_{hor} and V_{nmo} with vertical shifts, as was the case for parameterization II.

The main advantage of this parameter combination over parameterization II is that diving waves data can be inverted for an accurate low-wavenumber V_{hor} -field. High-resolution estimates of V_{hor} can be obtained from conventional offsets if the coefficient ϵ is well-constrained a priori.

4.4 Conclusions

We presented the results of elastic FWI for a 2D synthetic VTI model fashioned after the geologic section at Valhall field in the North Sea. The model includes low-velocity lenses above the reservoir, which are supposed to represent gas clouds. Diving waves mostly illuminate the top 1.5 km of the model, so the updates in the deeper regions are provided by reflected energy.

The inversion is carried out in the time domain with the gradients scaled by the inverse of an approximate Hessian matrix estimated using the L-BFGS-B algorithm. The initial model is generated

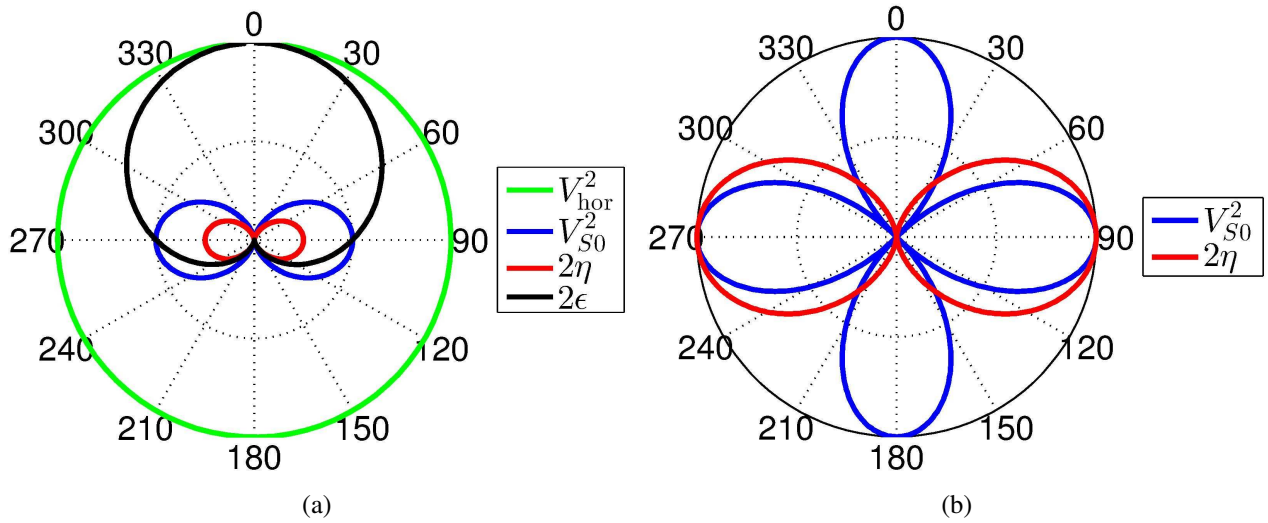


Figure 4.20: (a) P- and (b) SV-wave radiation patterns obtained with parameterization III for reflections from a horizontal interface.

by smoothing the actual velocities V_{P0} , V_{S0} , V_{nmo} , and V_{hor} , and the initial anisotropy coefficients ϵ , δ , and η are computed from the velocity fields. A multiscale approach is employed to mitigate cycle-skipping; the resolution of the inverted model, as expected, increases with the addition of higher frequencies. It is essential to employ an oblique (rather than vertical) displacement source, which produces intensive shear waves in the recorded offset range. This shear energy improves the inversion results not just for the S-wave vertical velocity V_{S0} , but also for the other parameters.

We test the performance of FWI for three different model parameterizations. The first includes the P-wave vertical (V_{P0}), NMO (V_{nmo}) and horizontal (V_{hor}) velocities and the shear-wave vertical velocity (V_{S0}). The P-wave radiation patterns of V_{P0} and V_{hor} do not significantly overlap, and the objective function is most sensitive to these two velocities. A high-resolution V_{P0} -field can be obtained even with conventional-offset data if the initial model does not produce cycle-skipping. To build an accurate low-wavenumber model of V_{hor} , it is necessary to use diving waves.

The objective function for the second parameterization, which consists of V_{nmo}^2 , V_{S0}^2 , $(1 + 2\eta)$, and $(1 + 2\delta)$, is more sensitive to the velocity V_{nmo} than to the other parameters. Because of the trade-off between V_{nmo} and the anisotropy coefficient η at large offsets, the long-wavelength model

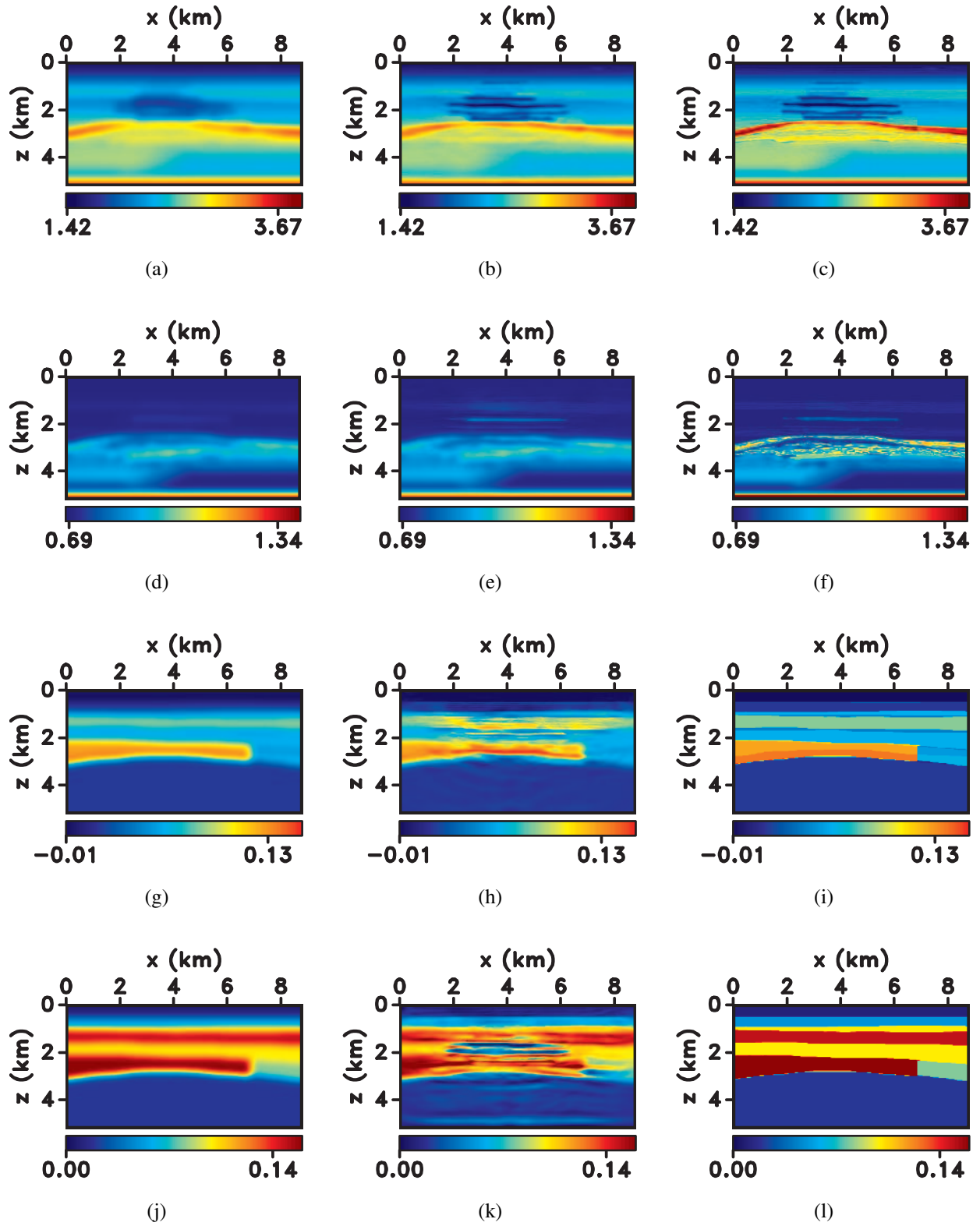


Figure 4.21: Initial (left column), inverted (middle column), and actual (right column) models for FWI performed using parameterization III. (a), (b), (c) correspond to V_{hor} , (d), (e), (f) to V_{S0} , (g), (h), (i) to η and (j), (k), (l) to δ .

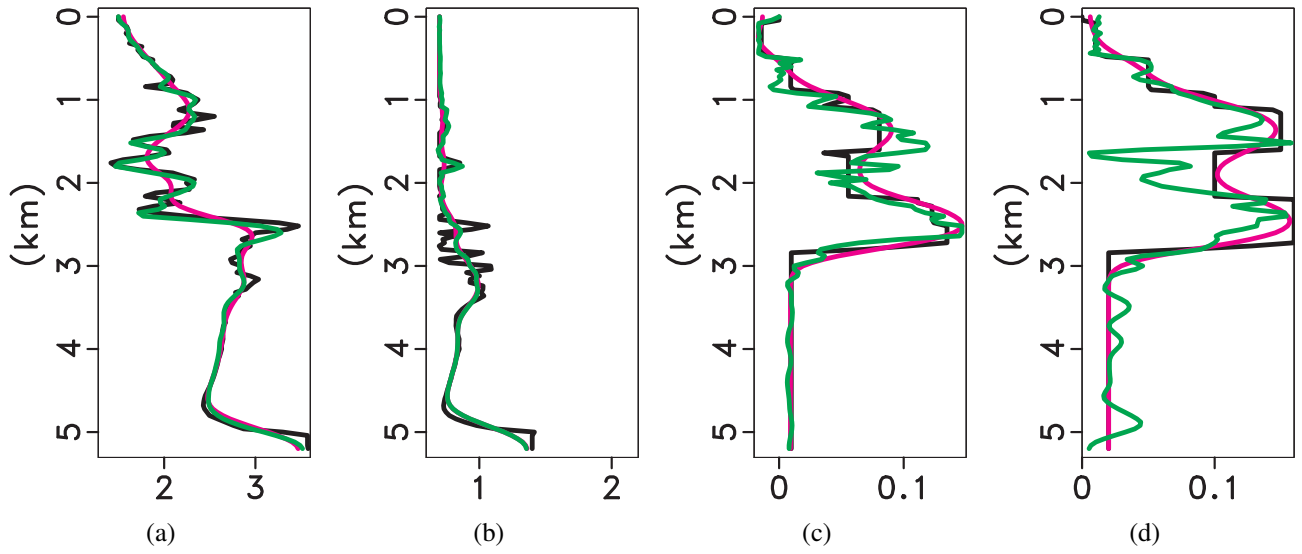


Figure 4.22: Actual (black), initial (magenta), and inverted (green) parameters for parameterization III: (a) V_{hor} , (b) V_{S0} , (c) η , and (d) ϵ .

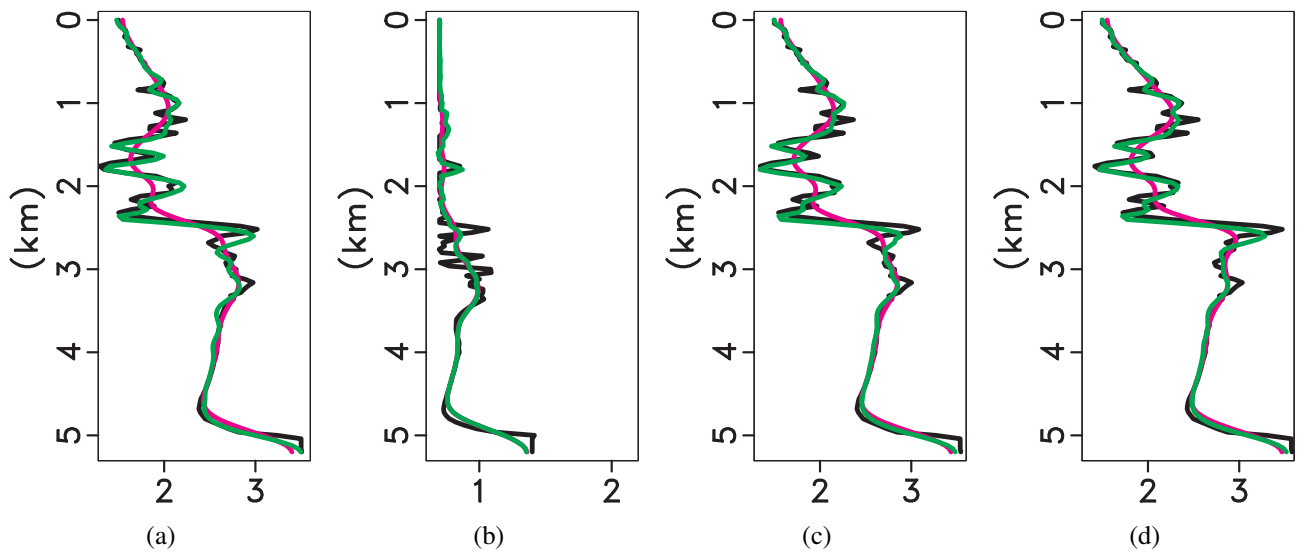


Figure 4.23: Actual (black), initial (magenta), and inverted (green) velocities for parameterization III: (a) V_{P0} , (b) V_{S0} , (c) V_{nmo} , and (d) V_{hor} .

of V_{nmo} cannot be built without good a priori knowledge of η . The possibility of obtaining a high-resolution V_{nmo} -field from data in the conventional offset range depends on the accuracy of the initial δ -field.

A low-wavenumber model of the horizontal velocity for parameterization III [V_{hor}^2 , V_{S0}^2 , $(1 + 2\eta)$, and $(1 + 2\epsilon)$] can be accurately estimated by inverting long-offset data because there are no trade-offs between V_{hor} and other parameters at large opening angles. Conventional-offset data can yield a high-resolution model of V_{hor} provided the ϵ -field is known with sufficient accuracy.

The results for this synthetic model provide important insights into the performance of elastic FWI for VTI media and should help in choosing the most suitable parameterization for different inversion scenarios.

4.5 Acknowledgments

We are grateful to the members of the A(nisotropy)- and i(maging)- teams at CWP and to Chunlei Chu and Phuong Vu (BP) for fruitful discussions. The fields of V_{P0} , V_{S0} , ϵ , and δ were provided to us by Romain Brossiere (Université Joseph Fourier, Grenoble) and Olav Barkved (Petoro, Norway). This work was supported by the Consortium Project on Seismic Inverse Methods for Complex Structures at CWP and competitive research funding from King Abdullah University of Science and Technology (KAUST). The reproducible numerical examples are generated with the Madagascar open-source software package freely available from <http://www.ahay.org>.

CHAPTER 5

SUMMARY AND FUTURE RECOMMENDATIONS

Here, I summarize the results of my thesis and provide recommendations for future work.

5.1 Summary

In this thesis I presented a methodology for full-waveform inversion (FWI) of multicomponent data in elastic VTI media. Sensitivity analysis for different model parameterizations employed in the inversion provided valuable insight into the obtained results.

First, FWI was performed for synthetic data generated for a horizontally layered VTI model. Moveout inversion, followed by kinematic layer stripping, was applied to compute the initial model. The parameters in the first layer and the densities in the entire model were fixed at the actual values during the inversion. The dynamic information contained in the reflected events helped invert for the parameters V_{P0} , V_{S0} , ϵ , and δ , even when only conventional offsets (with the offset-to-depth ratio close to unity) are available, and the data contain just PP events. The sensitivity of the objective function to the interval VTI parameters decreases with depth, and constraining the parameters of the deeper layers typically requires the addition of PS data.

Then elastic FWI was extended to 2D VTI media. The adjoint-state method is used to calculate the gradients of the objective function with respect to the model parameters. FWI is performed in the time domain and the steepest-descent method is employed to iteratively update the model. Two different parameterizations are used to test the algorithm on multicomponent data generated for Gaussian anomalies in Thomsen parameters embedded in a homogeneous VTI background.

To study the sensitivity of FWI to model parameters, I employed the Born and WKBJ approximations and ray-theoretic Green's functions to derive the P- and SV-wave radiation patterns for parameter perturbations. The general expressions were converted into simple approximations for perturbations in VTI parameters embedded in a homogeneous isotropic background. The P-wave radiation patterns in elastic VTI media are identical to those for acoustic VTI models. However,

in the absence of shear waves, the velocity V_{S0} cannot be determined. The parameter that scatters most of the energy close to the isotropy plane can be resolved in a crosshole setup. However, waves traveling predominantly in the vertical direction are required to constrain the parameters that scatter energy close to the symmetry axis.

To test the FWI algorithm in a more realistic scenario, I generated multicomponent data for a model based on a geologic section of the Valhall Field in the North Sea. A multiscale approach is employed to perform FWI using three model parameterizations. An oblique displacement source, which generates intensive shear waves, provides better parameter estimates than a vertical source. The parameterization that includes the velocities V_{P0} , V_{S0} , V_{nmo} , and V_{hor} produces P-wave radiation patterns with insignificant overlap between the velocities V_{P0} and V_{hor} . Therefore, diving-wave data can be used to estimate low-wavenumber components of the V_{hor} -field. If the initial V_{P0} -model can generate data which are not cycle-skipped, FWI also yields a high-resolution V_{P0} -field. Parameterization II includes the squared velocities V_{nmo}^2 and V_{S0}^2 and the parameters $(1 + 2\eta)$ and $(1 + 2\delta)$. For this parameter set, diving waves help estimate the low-wavenumber V_{nmo} -field, whose accuracy depends on a priori knowledge of the anellipticity parameter η . A higher resolution in V_{hor} can be obtained by inverting conventional-offset data provided the δ -field is known with sufficient accuracy. The third parameterization [V_{hor}^2 , V_{S0}^2 , $(1 + 2\eta)$, and $(1 + 2\epsilon)$] makes it possible to build an accurate long-wavelength model of the horizontal velocity because V_{hor} does not have trade-offs with any other parameter at long offsets. The results for this synthetic model provide important insights into the performance of elastic FWI for VTI media and should help in choosing the most suitable parameterization for different inversion scenarios.

5.2 Recommendations for future work

Existing FWI algorithms heavily rely on diving waves, which are most sensitive to the horizontal velocity V_{hor} , to update the background velocity model. It is extremely difficult to invert for the anisotropy coefficient δ without acquiring very low frequencies in the data (Alkhalifah, 2015a). For a horizontally layered VTI medium, I showed that modeling reflections helps invert for the

Thomsen coefficients V_{P0} , V_{S0} , ϵ , and δ with reasonable accuracy. In the case of a laterally heterogeneous medium, however, the background V_{P0} -field is seldom known with accuracy sufficient for imaging the reflectors at the correct depths. In addition, introducing high-resolution details in the model early on in the inversion leads to bias in the estimated parameters. There are ongoing efforts to build reflectors into the model, and simulate reflections at small and intermediate offsets (Wu and Alkhalifah, 2015; Xu et al., 2012; Zhou et al., 2015). This should help update the velocity V_{P0} , as was shown here for the transmission experiments. Such work is currently limited to acoustic (isotropic and VTI) media and could be extended to anisotropic elastic media. However, reflections generate mode conversions, which are likely to create artifacts and make the objective function more complex.

For the simple transmission experiments performed in this thesis, suppressing the SV-wave data in the adjoint source made the inversion converge much faster, and the results for V_{P0} , V_{nmo} , and V_{hor} were closer to the actual model. Hence, it may be beneficial to decompose the wavefields into modes during inversion. The added benefit of mode decomposition might be improved updates in the velocity V_{S0} (Wang and Cheng, 2015). This inversion, however, requires defining appropriate weights to combine the gradients computed with the P- and the SV-wavefields.

It has been shown that scaling the gradient of the objective function by an inverse Hessian (or an approximation of the Hessian) matrix leads to faster convergence (Métivier et al., 2014; Pratt et al., 1998; Virieux and Operto, 2009). The inverse Hessian compensates for geometrical spreading of the wavefield, the band-limited nature of the data, and higher-order scattering in the model. In this thesis, I implement the L-BFGS-B technique of Byrd et al. (1995) for the inversion tests performed on the synthetic Valhall Model. Métivier et al. (2014) show that the truncated-Newton method yields an improved approximation of the inverse Hessian matrix and accounts for second-order scattering better. In addition, they claim that this technique could help mitigate trade-offs between different parameters in multiparameter inversion. Hence, the truncated-Newton method, employed to FWI in elastic VTI media, might reduce the dependence of inversion results on model parameterization.

The inversion technique used in this thesis can be applied in the vertical symmetry planes of an orthorhombic medium. However, taking azimuthal variation into account would introduce more parameters and an appropriate scheme would have to be developed to invert for the full parameter set. Masmoudi and Alkhalifah (2016) perform a parameterization study for FWI in acoustic orthorhombic media and discuss a hierarchical strategy to invert 3D wide-azimuth data for the model parameters. Their strategy can be extended to elastic orthorhombic models.

REFERENCES CITED

- Aki, K., and P. G. Richards, 2002, Quantitative seismology, 2nd ed.: University Science Books.
- Alkhalifah, T., 2015a, Research Note: Insights into the data dependency on anisotropy: an inversion prospective: *Geophysical Prospecting*, **64**, 505–513.
- , 2015b, Scattering-angle based filtering of the waveform inversion gradients: *Geophysical Journal International*, **200**, 363–373.
- Alkhalifah, T., and R. Plessix, 2014, A recipe for practical full-waveform inversion in anisotropic media: An analytical parameter resolution study: *Geophysics*, **79**, R91–R101.
- Alkhalifah, T., and I. Tsvankin, 1995, Velocity analysis for transversely isotropic media: *Geophysics*, **60**, 1550–1566.
- Baeten, G., J. W. de Maag, R.-E. Plessix, R. Klaassen, T. Qureshi, M. Kleemeyer, F. t. Kroode, and Z. Rujie, 2013, The use of low frequencies in a full-waveform inversion and impedance inversion land seismic case study: *Geophysical Prospecting*, **61**, 701–711.
- Bamberger, A., 1982, Inversion of normal incidence seismograms: *Geophysics*, **47**, 757.
- Biondi, B., and A. Almomin, 2014, Simultaneous inversion of full data bandwidth by tomographic full-waveform inversion: *Geophysics*, **79**, WA129–WA140.
- Brenders, A. J., and R. G. Pratt, 2007, Full waveform tomography for lithospheric imaging: results from a blind test in a realistic crustal model: *Geophysical Journal International*, **168**, 133–151.
- Bunks, C., F. M. Saleck, S. Zaleski, and G. Chavent, 1995, Multiscale seismic waveform inversion: *Geophysics*, **60**, 1457–1473.
- Byrd, R. H., P. Lu, J. Nocedal, and C. Zhu, 1995, A limited memory algorithm for bound constrained optimization: *SIAM Journal on Scientific Computing*, **16**, 1190–1208.
- Calvet, M., S. Chevrot, and A. Souriau, 2006, P-wave propagation in transversely isotropic media: I. finite-frequency theory: *Physics of the Earth and Planetary Interiors*, **156**, 12–20.
- Chang, H., and G. McMechan, 2009, 3D 3-C full-wavefield elastic inversion for estimating anisotropic parameters: A feasibility study with synthetic data: *Geophysics*, **74**, WCC159–WCC175.

- Choi, Y., and T. Alkhalifah, 2013, Frequency-domain waveform inversion using the phase derivative: *Geophysical Journal International*, **195**, 1904–1916.
- Eaton, D. W. S., and R. R. Stewart, 1994, Migration/inversion for transversely isotropic elastic media: *Geophysical Journal International*, **119**, 667–683.
- Fichtner, A., H.-P. Bunge, and H. Igel, 2006, The adjoint method in seismology: I. theory: *Physics of the Earth and Planetary Interiors*, **157**, 86 – 104.
- Fryer, G. J., and L. N. Frazer, 1984, Seismic waves in stratified anisotropic media: *Geophysical Journal of the Royal Astronomical Society*, **78**, 691–710.
- Gauthier, O., 1986, Two-dimensional nonlinear inversion of seismic waveforms: Numerical results: *Geophysics*, **51**, 1387–1403.
- Gholami, Y., R. Brossier, S. Operto, V. Prioux, A. Ribodetti, and J. Virieux, 2011, Two-dimensional acoustic anisotropic (VTI) full waveform inversion: The Valhall case study: *SEG Technical Program Expanded Abstracts*, **30**, 2543–2548.
- , 2013a, Which parameterization is suitable for acoustic vertical transverse isotropic full waveform inversion? Part 2: Synthetic and real data case studies from Valhall: *Geophysics*, **78**, R107–R124.
- Gholami, Y., R. Brossier, S. Operto, A. Ribodetti, and J. Virieux, 2013b, Which parameterization is suitable for acoustic vertical transverse isotropic full waveform inversion? Part 1: Sensitivity and trade-off analysis: *Geophysics*, **78**, R81–R105.
- Grechka, V., and I. Tsvankin, 1998, Feasibility of nonhyperbolic moveout inversion in transversely isotropic media: *Geophysics*, **63**, 957–969.
- , 2002, The joint nonhyperbolic moveout inversion of PP and PS data in VTI media: *Geophysics*, **67**, 1929–1932.
- Kamath, N., and I. Tsvankin, 2013, Full-waveform inversion of multicomponent data for horizontally layered VTI media: *Geophysics*, **78**, WC113–WC121.
- , 2016, Elastic full-waveform inversion for vti media: Methodology and sensitivity analysis: *Geophysics*, **81**, C53–C68.
- Kolb, P., F. Collino, and P. Lailly, 1986, Pre-stack inversion of a 1-D medium: *Proceedings of the IEEE*, **74**, 498–508.

- Lailly, P., 1983, The seismic inverse problem as a sequence of before stack migrations: Conference on Inverse Scattering: Theory and Application, Society for Industrial and Applied Mathematics, Philadelphia, PA, 206–220.
- Lee, H., J. M. Koo, D. Min, B. Kwon, and H. S. Yoo, 2010, Frequency-domain elastic full waveform inversion for VTI media: *Geophysical Journal International*, **183**, 884–904.
- Liu, Q., and J. Tromp, 2006, Finite-frequency kernels based on adjoint methods: *Bulletin of the Seismological Society of America*, **96**, 2383–2397.
- Mallick, S., and L. N. Frazer, 1990, Computation of synthetic seismograms for stratified azimuthally anisotropic media: *Journal of Geophysical Research*, **95**, PP. 8513–8526.
- Masmoudi, N., and T. Alkhalifah, 2016, A new parametrization for waveform inversion in acoustic orthorhombic media. *Geophysical Journal International*, accepted.
- Métivier, L., F. Bretaudeau, R. Brossier, S. Operto, and J. Virieux, 2014, Full waveform inversion and the truncated newton method: quantitative imaging of complex subsurface structures: *Geophysical Prospecting*, **62**, 1353–1375.
- Mora, P., 1987, Nonlinear two-dimensional elastic inversion of multioffset seismic data: *Geophysics*, **52**, 1211–1228.
- Munns, J., 1985, The Valhall field: a geological overview: *Marine and Petroleum Geology*, **2**, 23–43.
- Padhi, A., and S. Mallick, 2013, Accurate estimation of density from the inversion of multicomponent prestack seismic waveform data using a nondominated sorting genetic algorithm: *The Leading Edge*, **32**, 94–98.
- Plessix, R., 2006, A review of the adjointstate method for computing the gradient of a functional with geophysical applications: *Geophysical Journal International*, **167**, 495–503.
- Plessix, R., and Q. Cao, 2011, A parameterization study for surface seismic full waveform inversion in an acoustic vertical transversely isotropic medium: *Geophysical Journal International*, **185**, 539–556.
- Plessix, R.-E., G. Baeten, J. W. de Maag, M. Klaassen, Z. Rujie, and T. Zhifei, 2010, Application of acoustic full waveform inversion to a low-frequency large-offset land data set: *SEG Technical Program Expanded Abstracts*, **29**, 930–934.
- Plessix, R.-E., and H. Rynja, 2010, VTI full waveform inversion: a parameterization study with a narrow azimuth streamer data example: *SEG Technical Program Expanded Abstracts*, **29**, 962–966.

- Pratt, G., C. Shin, and Hicks, 1998, GaussNewton and full newton methods in frequencyspace seismic waveform inversion: *Geophysical Journal International*, **133**, 341–362.
- Pratt, R. G., 1999, Seismic waveform inversion in the frequency domain, Part 1: Theory and verification in a physical scale model: *Geophysics*, **64**, 888–901.
- Pratt, R. G., and R. M. Shipp, 1999, Seismic waveform inversion in the frequency domain, Part 2: Fault delineation in sediments using crosshole data: *Geophysics*, **64**, 902–914.
- Prieux, V., R. Brossier, Y. Gholami, S. Operto, J. Virieux, O. I. Barkved, and J. H. Kommedal, 2011, On the footprint of anisotropy on isotropic full waveform inversion: the Valhall case study: *Geophysical Journal International*, **187**, 1495–1515.
- Prieux, V., R. Brossier, S. Operto, and J. Virieux, 2013a, Multiparameter full waveform inversion of multicomponent ocean-bottom-cable data from the Valhall field. part 1: imaging compressional wave speed, density and attenuation: *Geophysical Journal International*, **194**, 1640–1664.
- , 2013b, Multiparameter full waveform inversion of multicomponent ocean-bottom-cable data from the Valhall field. part 2: imaging compressive-wave and shear-wave velocities: *Geophysical Journal International*, **194**, 1665–1681.
- Rüger, A., 1997, P-wave reflection coefficients for transversely isotropic models with vertical and horizontal axis of symmetry: *Geophysics*, **62**, 713–722.
- , 2002, Reflection coefficients and azimuthal AVO analysis in anisotropic media: *Society of Exploration Geophysicists*.
- Sears, T. J., P. J. Barton, and S. C. Singh, 2010, Elastic full waveform inversion of multicomponent ocean-bottom cable seismic data: Application to Alba Field, U.K. North sea: *Geophysics*, **75**, R109–R119.
- Sears, T. J., S. C. Singh, and P. J. Barton, 2008, Elastic full waveform inversion of multicomponent OBC seismic data: *Geophysical Prospecting*, **56**, 843–862.
- Seriff, A. J., and K. Sriram, 1991, P-SV reflection moveouts for transversely isotropic media with a vertical symmetry axis: *Geophysics*, **56**, 1271–1274.
- Shen, X., 2012, Early-arrival waveform inversion for near-surface velocity and anisotropic parameter: Parametrization study: *SEG Technical Program Expanded Abstracts*, **31**.
- Shin, C., and Y. H. Cha, 2008, Waveform inversion in the laplace domain: *Geophysical Journal International*, **173**, 922–931.

- Shin, C., and Y. Ho Cha, 2009, Waveform inversion in the LaplaceFourier domain: *Geophysical Journal International*, **177**, 1067–1079.
- Sirgue, L., and R. G. Pratt, 2004, Efficient waveform inversion and imaging: A strategy for selecting temporal frequencies: *Geophysics*, **69**, 231–248.
- Song, Z., and P. R. Williamson, 1995, Frequency-domain acoustic-wave modeling and inversion of crosshole data: Part 1 — 2.5-D modeling method: *Geophysics*, **60**, 784–795.
- Song, Z., P. R. Williamson, and R. G. Pratt, 1995, Frequency-domain acoustic-wave modeling and inversion of crosshole data: Part II — Inversion method, synthetic experiments and real-data results: *Geophysics*, **60**, 796–809.
- Strang, G., 1991, *Calculus*: Wellesley-Cambridge Press.
- Tarantola, A., 1984a, Inversion of seismic reflection data in the acoustic approximation: *Geophysics*, **49**, 1259–1266.
- , 1984b, Linearized inversion of seismic reflection data: *Geophysical Prospecting*, **32**, 998–1015.
- Thomsen, L., 1986, Weak elastic anisotropy: *Geophysics*, **51**, 1954–1966.
- Tsvankin, I., 1995, Body-wave radiation patterns and AVO in transversely isotropic media: *Geophysics*, **60**, 1409–1425.
- , 2012, *Seismic signatures and analysis of reflection data in anisotropic media*, 3rd ed.: Society of Exploration Geophysicists.
- Tsvankin, I., and L. Thomsen, 1995, Inversion of reflection traveltimes for transverse isotropy: *Geophysics*, **60**, 1095–1107.
- Vavryčuk, V., 2007, Asymptotic Green's function in homogeneous anisotropic viscoelastic media: *Proceedings of the Royal Society A: Mathematical, Physical and Engineering Science*, **463**, 2689–2707.
- Vigh, D., K. Jiao, D. Watts, and D. Sun, 2014, Elastic full-waveform inversion application using multicomponent measurements of seismic data collection: *Geophysics*, **79**, R63–R77.
- Virieux, J., and S. Operto, 2009, An overview of full-waveform inversion in exploration geophysics: *Geophysics*, **74**, WCC1–26.
- Wang, T., and J. Cheng, 2015, Elastic wave mode decoupling for full waveform inversion: *SEG Technical Program Expanded Abstracts 2015*, 1461–1466.

- Wang, X., and I. Tsvankin, 2009, Estimation of interval anisotropy parameters using velocity-independent layer stripping: *Geophysics*, **74**, WB117–WB127.
- Warner, M., A. Ratcliffe, T. Nangoo, J. Morgan, A. Umpleby, N. Shah, V. Vinje, I. tekl, L. Guasch, C. Win, G. Conroy, and A. Bertrand, 2013, Anisotropic 3D full-waveform inversion: *Geophysics*, **78**, R59–R80.
- Williamson, P. R., 1991, A guide to the limits of resolution imposed by scattering in ray tomography: *Geophysics*, **56**, 202–207.
- Wu, R., and M. Toksöz, 1987, Diffraction tomography and multisource holography applied to seismic imaging: *Geophysics*, **52**, 11–25.
- Wu, Z., and T. Alkhalifah, 2015, Simultaneous inversion of the background velocity and the perturbation in full-waveform inversion: *Geophysics*, **80**, R317–R329.
- Xu, S., D. Wang, F. Chen, G. Lambar, and Y. Zhang, 2012, Inversion on reflected seismic wave: SEG Technical Program Expanded Abstracts 2012, 1–7.
- Xu, X., and I. Tsvankin, 2008, Moveout-based geometrical-spreading correction for PS-waves in layered anisotropic media: *Journal of Geophysics and Engineering*, **5**, 195–202.
- Xu, X., I. Tsvankin, and A. Pech, 2005, Geometrical spreading of P-waves in horizontally layered, azimuthally anisotropic media: *Geophysics*, **70**, D43–D53.
- Zhou, W., R. Brossier, S. Operto, and J. Virieux, 2015, Full waveform inversion of diving and reflected waves for velocity model building with impedance inversion based on scale separation: *Geophysical Journal International*, **202**, 1535–1554.

APPENDIX A - GRADIENT COMPUTATION FOR VTI MEDIA USING THE
ADJOINT-STATE METHOD

As discussed in Plessix (2006) and Liu and Tromp (2006), the objective function in equation 3.1 should be minimized under the constraint that the modeled displacement $\mathbf{u}(\mathbf{x}_r, t)$ satisfies the wave equation. Here, we use the elastic wave equation for heterogeneous, arbitrarily anisotropic media:

$$\rho \frac{\partial^2 u_i}{\partial t^2} - \frac{\partial}{\partial x_j} \left(c_{ijkl} \frac{\partial u_k}{\partial x_l} \right) = f_i, \quad (\text{A.1})$$

where ρ is the density, c_{ijkl} are the components of the stiffness tensor, and \mathbf{f} is the body force per unit volume. All indices range from 1 to 3 and summation over repeated indices is implied. The displacement wavefield is subject to the initial conditions,

$$\mathbf{u}(\mathbf{x}, 0) = 0, \quad \frac{\partial \mathbf{u}(\mathbf{x}, 0)}{\partial t} = 0, \quad (\text{A.2})$$

and the radiation boundary condition,

$$\mathbf{u}(\mathbf{x}, t)|_{\mathbf{x} \rightarrow \infty} \rightarrow 0. \quad (\text{A.3})$$

The method of Lagrange multipliers (Strang, 1991) is used to define the Lagrangian Λ :

$$\Lambda = \frac{1}{2} \sum_r \int_0^T \|\mathbf{u}(\mathbf{x}_r, t) - \mathbf{d}(\mathbf{x}_r, t)\|^2 dt - \int_0^T \int_{\Omega} \lambda_i \left[\rho \frac{\partial^2 u_i}{\partial t^2} - \frac{\partial}{\partial x_j} \left(c_{ijkl} \frac{\partial u_k}{\partial x_l} \right) - f_i \right] dV dt, \quad (\text{A.4})$$

where $r = 1, 2 \dots N$ denotes the receivers, Ω is the integration domain (which includes the entire 3D space), $\partial\Omega$ is the surface of Ω , and $\boldsymbol{\lambda}(\mathbf{x}, t)$ is the vector Lagrange multiplier that needs to be determined. The objective is to find the stationary points of the Lagrangian, which is done by calculating the variation in Λ when \mathbf{u} , $\boldsymbol{\lambda}$, and c_{ijkl} are perturbed. After integration by parts and application of the Gauss divergence theorem, we obtain the change in the Lagrangian,

$$\begin{aligned}
\delta\Lambda = & \int_0^T \int_{\Omega} \sum_{r=1}^N \left(u_i(\mathbf{x}, t) - d_i(\mathbf{x}, t) \right) \delta(\mathbf{x} - \mathbf{x}_r) \delta u_i dV dt \\
& - \int_0^T \int_{\Omega} \delta c_{ijkl} \frac{\partial u_k}{\partial x_l} \frac{\partial \lambda_i}{\partial x_j} dV dt - \int_0^T \int_{\Omega} \left[\rho \frac{\partial^2 \lambda_i}{\partial t^2} - \frac{\partial}{\partial x_j} \left(c_{ijkl} \frac{\partial \lambda_k}{\partial x_l} \right) \right] \delta u_i dV dt \\
& - \int_0^T \int_{\Omega} \left[\rho \frac{\partial^2 \lambda_i}{\partial t^2} - \frac{\partial}{\partial x_j} \left(c_{ijkl} \frac{\partial \lambda_k}{\partial x_l} \right) - f_i \right] \delta \lambda_i dV dt \\
& - \int_{\Omega} \left[\rho \lambda_i \frac{\partial(\delta u_i)}{\partial t} - \rho \delta u_i \frac{\partial \lambda_i}{\partial t} \right] \Bigg|_0^T dV \\
& + \int_0^T \int_{\partial\Omega} \lambda_i \left[\delta c_{ijkl} \frac{\partial u_k}{\partial x_l} + c_{ijkl} \frac{\partial(\delta u_k)}{\partial x_l} \right] n_j dS dt - \int_0^T \int_{\partial\Omega} \delta u_i c_{ijkl} \frac{\partial \lambda_k}{\partial x_l} n_j dS dt, \quad (\text{A.5})
\end{aligned}$$

where \mathbf{n} is the vector normal to the surface $\partial\Omega$. Perturbing $\mathbf{u}(\mathbf{x}, t)$ in equations A.2 and A.3 yields the initial and boundary conditions for $\delta\mathbf{u}(\mathbf{x}, t)$:

$$\delta\mathbf{u}(\mathbf{x}, 0) = 0, \quad \frac{\partial \delta\mathbf{u}(\mathbf{x}, t)}{\partial t} = 0, \quad \delta\mathbf{u}(\mathbf{x}, t)|_{\mathbf{x} \rightarrow \infty} \rightarrow 0. \quad (\text{A.6})$$

The Lagrange multiplier $\boldsymbol{\lambda}$ is constrained by the “final” conditions (i.e., those at time T),

$$\boldsymbol{\lambda}(\mathbf{x}, T) = 0, \quad \frac{\partial \boldsymbol{\lambda}(\mathbf{x}, T)}{\partial t} = 0, \quad (\text{A.7})$$

and the boundary condition,

$$\boldsymbol{\lambda}(\mathbf{x}, t) |_{\mathbf{x} \rightarrow \infty} \rightarrow 0. \quad (\text{A.8})$$

Equation A.5 then reduces to

$$\begin{aligned}
\delta\Lambda = & \int_0^T \int_{\Omega} \left\{ \sum_{r=1}^N \left(u_i(\mathbf{x}, t) - d_i(\mathbf{x}, t) \right) \delta(\mathbf{x} - \mathbf{x}_r) - \left[\rho \frac{\partial^2 \lambda_i}{\partial t^2} - \frac{\partial}{\partial x_j} \left(c_{ijkl} \frac{\partial \lambda_k}{\partial x_l} \right) \right] \right\} \delta u_i dV dt \\
& - \int_0^T \int_{\Omega} \frac{\partial u_k}{\partial x_l} \frac{\partial \lambda_i}{\partial x_j} \delta c_{ijkl} dV dt \\
& - \int_0^T \int_{\Omega} \left[\rho \frac{\partial^2 \lambda_i}{\partial t^2} - \frac{\partial}{\partial x_j} \left(c_{ijkl} \frac{\partial \lambda_k}{\partial x_l} \right) - f_i \right] \delta \lambda_i dV dt . \tag{A.9}
\end{aligned}$$

The Lagrangian is stationary with respect to the variables \mathbf{u} , $\boldsymbol{\lambda}$, and c_{ijkl} when the coefficients of δu_i , $\delta \lambda_i$, and δc_{ijkl} in the integrands of equation A.9 go to zero. For a given model (i.e., fixed c_{ijkl}), setting the coefficient of $\delta \lambda_i$ to zero gives the state equation, which coincides with the elastic wave equation A.1. Setting the coefficient of δu_i to zero yields the adjoint-state equation:

$$\rho \frac{\partial^2 \lambda_i}{\partial t^2} - \frac{\partial}{\partial x_j} \left(c_{ijkl} \frac{\partial \lambda_k}{\partial x_l} \right) = \sum_{r=1}^N \left[u_i(\mathbf{x}_r, t) - d_i(\mathbf{x}_r, t) \right], \tag{A.10}$$

subject to the conditions at time T (equation A.7) and boundary conditions (equation A.8). Equations A.1 and then A.10 are solved to obtain the wavefields \mathbf{u} and $\boldsymbol{\lambda}$ respectively.

Substituting \mathbf{u} and $\boldsymbol{\lambda}$ into the coefficient of the term containing δc_{ijkl} in equation A.9 gives the variation in the Lagrangian with the stiffnesses. Since $\Lambda = \mathcal{F}$ when \mathbf{u} satisfies the wave equation (from equation A.4), the change in the objective function $\delta \mathcal{F}$ caused by perturbations of the stiffness coefficients is given by:

$$\delta \mathcal{F} = - \int_0^T \int_{\Omega} \frac{\partial u_i}{\partial x_j} \frac{\partial \lambda_k}{\partial x_l} \delta c_{ijkl} dV dt . \tag{A.11}$$

This is a general result for an anisotropic medium described by the complete stiffness tensor c_{ijkl} . Expressions for models with specific symmetries can be derived from equation A.11 by substituting the appropriate stiffness tensors or matrices.

Note that the boundary conditions for $\mathbf{u}(\mathbf{x}, t)$ and $\boldsymbol{\lambda}(\mathbf{x}, t)$ can be modified to include a free surface where the tractions due to \mathbf{u} and $\boldsymbol{\lambda}$ go to zero. However, the addition of the free surface causes complications in finite-difference modeling and produces surface multiples. Instead, we impose the radiation condition to create absorbing boundaries on all sides of the model.

To simulate the Lagrange-multiplier wavefield, it is convenient to define an ‘‘adjoint wavefield’’ ψ (Liu and Tromp, 2006):

$$\psi(\mathbf{x}, t) \equiv \boldsymbol{\lambda}(\mathbf{x}, T - t). \quad (\text{A.12})$$

The wavefield ψ satisfies the wave equation A.10 but with the source function reversed in time:

$$\rho \frac{\partial^2 \psi_i}{\partial t^2} - \frac{\partial}{\partial x_j} \left(c_{ijkl} \frac{\partial \psi_k}{\partial x_l} \right) = \sum_{r=1}^N \left[u_i(\mathbf{x}_r, T - t) - d_i(\mathbf{x}_r, T - t) \right]. \quad (\text{A.13})$$

The initial conditions for ψ (using equations A.7 and A.12) are as follows:

$$\psi(\mathbf{x}, 0) = 0, \quad \frac{\partial \psi(\mathbf{x}, 0)}{\partial t} = 0. \quad (\text{A.14})$$

The wavefield ψ also satisfies the radiation boundary condition:

$$\psi(\mathbf{x}, t)|_{\mathbf{x} \rightarrow \infty} \rightarrow 0. \quad (\text{A.15})$$

From equations A.11 and A.12, we can find the gradient of the objective function with respect to the stiffness coefficients:

$$\frac{\partial \mathcal{F}}{\partial c_{ijkl}} = - \int_0^T \frac{\partial u_i}{\partial x_j} \frac{\partial \psi_k}{\partial x_l} dt. \quad (\text{A.16})$$

If, instead of c_{ijkl} , the model is described by parameters m_n , the gradient of \mathcal{F} can be found from the chain rule:

$$\frac{\partial \mathcal{F}}{\partial m_n} = \sum_{ijkl} \frac{\partial \mathcal{F}}{\partial c_{ijkl}} \frac{\partial c_{ijkl}}{\partial m_n}. \quad (\text{A.17})$$

Here, we implement FWI for two sets of parameters. First, the model is parameterized in terms of the velocities V_{P0} , V_{S0} , V_{nmo} , and V_{hor} . The stiffness coefficients (written in the two-index notation) represent the following functions of the velocities (Tsvankin, 2012):

$$C_{11} = \rho V_{\text{hor}}^2, \quad (\text{A.18})$$

$$C_{33} = \rho V_{P0}^2, \quad (\text{A.19})$$

$$C_{13} = \rho \sqrt{(V_{P0}^2 - V_{S0}^2)(V_{\text{nmo}}^2 - V_{S0}^2)} - \rho V_{S0}^2, \quad (\text{A.20})$$

$$C_{55} = \rho V_{S0}^2. \quad (\text{A.21})$$

Using equations A.16, A.17, and A.18 – A.21, we obtain the derivatives of the objective function with respect to the velocities:

$$\frac{\partial \mathcal{F}}{\partial V_{P0}} = -2\rho V_{P0} \int_0^T \left[\frac{\partial \psi_3}{\partial x_3} \frac{\partial u_3}{\partial x_3} + \frac{f}{2} \left(\frac{\partial \psi_1}{\partial x_1} \frac{\partial u_3}{\partial x_3} + \frac{\partial \psi_3}{\partial x_3} \frac{\partial u_1}{\partial x_1} \right) \right] dt, \quad (\text{A.22})$$

$$\begin{aligned} \frac{\partial \mathcal{F}}{\partial V_{S0}} = 2\rho V_{S0} \int_0^T \left\{ \left[1 + \frac{f}{2} + \frac{1}{2f} \right] \left(\frac{\partial \psi_1}{\partial x_1} \frac{\partial u_3}{\partial x_3} + \frac{\partial \psi_3}{\partial x_3} \frac{\partial u_1}{\partial x_1} \right) \right. \\ \left. - \left(\frac{\partial \psi_1}{\partial x_3} + \frac{\partial \psi_3}{\partial x_1} \right) \left(\frac{\partial u_1}{\partial x_3} + \frac{\partial u_3}{\partial x_1} \right) \right\} dt, \end{aligned} \quad (\text{A.23})$$

$$\frac{\partial \mathcal{F}}{\partial V_{\text{nmo}}} = -\frac{\rho V_{\text{nmo}}}{f} \int_0^T \left(\frac{\partial \psi_1}{\partial x_1} \frac{\partial u_3}{\partial x_3} + \frac{\partial \psi_3}{\partial x_3} \frac{\partial u_1}{\partial x_1} \right) dt, \quad (\text{A.24})$$

$$\frac{\partial \mathcal{F}}{\partial V_{\text{hor}}} = -2\rho V_{\text{hor}} \int_0^T \frac{\partial \psi_1}{\partial x_1} \frac{\partial u_1}{\partial x_1} dt, \quad (\text{A.25})$$

where

$$f \equiv \sqrt{\frac{V_{\text{nmo}}^2 - V_{S0}^2}{V_{P0}^2 - V_{S0}^2}}. \quad (\text{A.26})$$

The second parameterization includes the following parameters (Shen, 2012):

$$m_1 = \ln \left(\frac{1}{V_{P0}^2} \right), \quad (\text{A.27})$$

$$m_2 = \ln \left(\frac{1}{V_{S0}^2} \right), \quad (\text{A.28})$$

$$m_3 = 1 + 2\epsilon, \quad (\text{A.29})$$

$$m_4 = 1 + 2\delta. \quad (\text{A.30})$$

After the stiffness coefficients are expressed in terms of m_1 , m_2 , m_3 , and m_4 , equations A.16 and A.17 yield:

$$\begin{aligned} \frac{\partial \mathcal{F}}{\partial m_1} = \rho V_{P0}^2 \int_0^T & \left[(1 + 2\epsilon) \frac{\partial \psi_1}{\partial x_1} \frac{\partial u_1}{\partial x_1} + \frac{\partial \psi_3}{\partial x_3} \frac{\partial u_3}{\partial x_3} \right. \\ & \left. + \left(\frac{1 + 2\delta}{2f} + \frac{f}{2} \right) \left(\frac{\partial \psi_3}{\partial x_3} \frac{\partial u_1}{\partial x_1} + \frac{\partial \psi_1}{\partial x_1} \frac{\partial u_3}{\partial x_3} \right) \right] dt, \end{aligned} \quad (\text{A.31})$$

$$\begin{aligned} \frac{\partial \mathcal{F}}{\partial m_2} = \rho V_{S0}^2 \int_0^T & \left[\left(\frac{\partial \psi_1}{\partial x_3} + \frac{\partial \psi_3}{\partial x_1} \right) \left(\frac{\partial u_1}{\partial x_3} + \frac{\partial u_3}{\partial x_1} \right) \right. \\ & \left. - \left(\frac{f}{2} + \frac{1}{2f} + 1 \right) \left(\frac{\partial \psi_3}{\partial x_3} \frac{\partial u_1}{\partial x_1} + \frac{\partial \psi_1}{\partial x_1} \frac{\partial u_3}{\partial x_3} \right) \right] dt, \end{aligned} \quad (\text{A.32})$$

$$\frac{\partial \mathcal{F}}{\partial m_3} = -\rho V_{P0}^2 \int_0^T \frac{\partial \psi_1}{\partial x_1} \frac{\partial u_1}{\partial x_1} dt, \quad (\text{A.33})$$

$$\frac{\partial \mathcal{F}}{\partial m_4} = -\frac{\rho V_{P0}^2}{2f} \int_0^T \left(\frac{\partial \psi_3}{\partial x_3} \frac{\partial u_1}{\partial x_1} + \frac{\partial \psi_1}{\partial x_1} \frac{\partial u_3}{\partial x_3} \right) dt. \quad (\text{A.34})$$

APPENDIX B - SENSITIVITY PATTERNS FOR ELASTIC FWI IN VTI MEDIA

The radiation pattern is obtained by expressing the scattered wavefield in the Born approximation using the asymptotic Green's function. Suppose the wavefield produced by a source at location

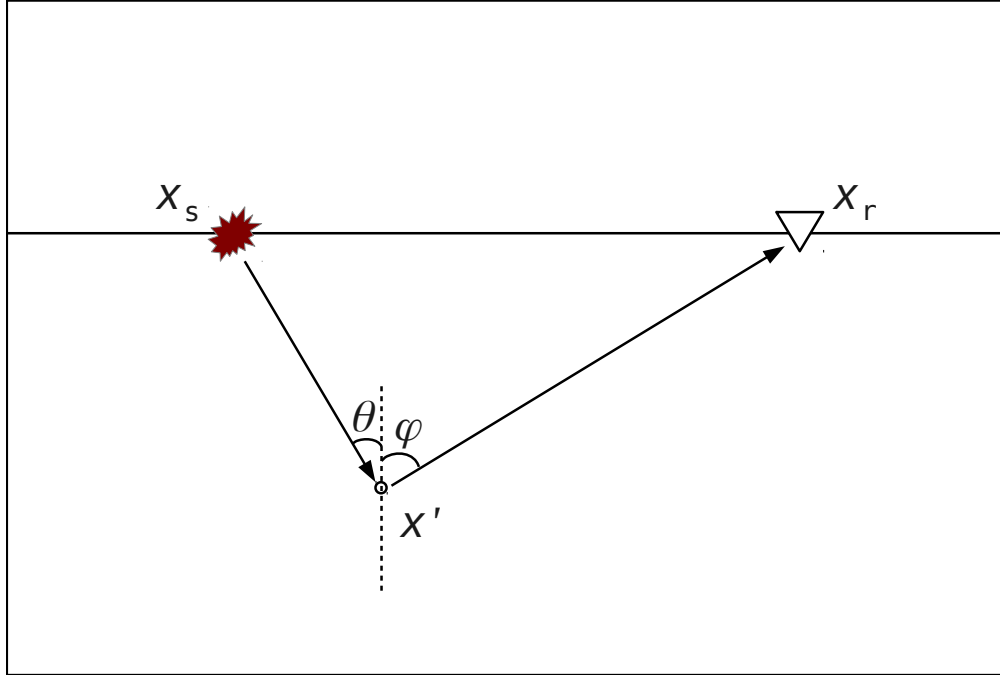


Figure B.1: Geometry of the scattering experiment. The source is located at \mathbf{x}_s , the scatterer at \mathbf{x}' , and the receiver at \mathbf{x}_r .

\mathbf{x}_s is scattered at \mathbf{x}' and recorded by a receiver at \mathbf{x}_r . A perturbation δc_{ijkl} in the stiffness coefficient c_{ijkl} at the scatterer \mathbf{x}' (Figure B.1) results in a perturbation δu_i in the wavefield. We replace the wavefield u_i in equation A.1 by $u_i = u_i^b + \delta u_i$ and the stiffnesses c_{ijkl} by $c_{ijkl} = c_{ijkl}^b + \delta c_{ijkl}$, where the superscript b refers to the background medium. Retaining only the terms linear in the perturbations in equation A.1 leads to the Born approximation:

$$\rho \frac{\partial^2 \delta u_i}{\partial t^2} - \frac{\partial}{\partial x_j} \left(c_{ijkl}^b \frac{\partial \delta u_k}{\partial x_l} \right) = \frac{\partial}{\partial x_j} \left(\delta c_{ijkl} \frac{\partial u_k^b}{\partial x_l} \right). \quad (\text{B.1})$$

The wave equation A.1 can be solved in the frequency domain in terms of the Green's function using the representation theorem:

$$u_n(\mathbf{x}_r, \omega) = \int_{V(\mathbf{x}')} h_i(\mathbf{x}', \omega) G_{ni}(\mathbf{x}_r, \mathbf{x}', \omega) dV(\mathbf{x}'), \quad (\text{B.2})$$

where $h_i(\mathbf{x}', \omega)$ is the force density at \mathbf{x}' , $G_{ni}(\mathbf{x}_r, \mathbf{x}', \omega)$ is the Green's function for the source at \mathbf{x}' and receiver at \mathbf{x}_r , and $V(\mathbf{x}')$ represents the volume that includes all sources. To solve equation B.1 for the scattered field, we replace $h_i(\mathbf{x}', \omega)$ in equation B.2 by the right-hand side (source term) of equation B.1:

$$\begin{aligned} \delta u_n(\mathbf{x}_r, \omega) &= \int_{V(\mathbf{x}')} \frac{\partial}{\partial x'_j} \left(\delta c_{ijkl} \frac{\partial u_k^b}{\partial x'_l} \right) G_{ni} dV(\mathbf{x}') \\ &= \int_{V(\mathbf{x}')} \left[\frac{\partial}{\partial x'_j} \left(\delta c_{ijkl} \frac{\partial u_k^b}{\partial x'_l} G_{ni} \right) - \delta c_{ijkl} \frac{\partial u_k^b}{\partial x'_l} \frac{\partial G_{ni}}{\partial x'_j} \right] dV(\mathbf{x}'). \end{aligned} \quad (\text{B.3})$$

Applying the divergence theorem to the first term in the integrand of equation B.3 yields:

$$\delta u_n(\mathbf{x}_r, \omega) = \int_{S(\mathbf{x}')} \delta c_{ijkl} \frac{\partial u_k^b}{\partial x'_l} G_{ni} \nu_j dS(\mathbf{x}') - \int_{V(\mathbf{x}')} \delta c_{ijkl} \frac{\partial u_k^b}{\partial x'_l} \frac{\partial G_{ni}}{\partial x'_j} dV(\mathbf{x}'), \quad (\text{B.4})$$

where $S(\mathbf{x}')$ is the surface of the volume $V(\mathbf{x}')$, and $\boldsymbol{\nu}$ is the normal to $S(\mathbf{x}')$ pointing outward. Expanding the volume $V(\mathbf{x}')$ to infinity and using the radiation boundary condition (equation A.3) reduces equation B.4 to

$$\delta u_n(\mathbf{x}_r, \omega) = - \int_{V(\mathbf{x}')} \delta c_{ijkl}(\mathbf{x}') \frac{\partial u_k^b(\mathbf{x}', \omega)}{\partial x'_l} \frac{\partial G_{ni}(\mathbf{x}_r, \mathbf{x}', \omega)}{\partial x'_j} dV(\mathbf{x}'). \quad (\text{B.5})$$

Here, the wavefield \mathbf{u}^b is computed in the background medium and is generated by the force at the source location \mathbf{x}_s . Hence, \mathbf{u}^b can be expressed in terms of the force applied at \mathbf{x}_s and the Green's function:

$$u_k^b(\mathbf{x}', \omega) = f_m(\mathbf{x}_s, \omega) G_{km}(\mathbf{x}', \mathbf{x}_s, \omega). \quad (\text{B.6})$$

Substituting equation B.6 into equation B.4 and using reciprocity,

$$G_{km}(\mathbf{x}', \mathbf{x}_s, \omega) = G_{mk}(\mathbf{x}_s, \mathbf{x}', \omega), \quad (\text{B.7})$$

we find:

$$\delta u_n(\mathbf{x}_r, \omega) = - \int_{V(\mathbf{x}')} f_m(\mathbf{x}_s, \omega) \delta c_{ijkl}(\mathbf{x}') \frac{\partial G_{mk}(\mathbf{x}_s, \mathbf{x}', \omega)}{\partial x'_l} \frac{\partial G_{ni}(\mathbf{x}_r, \mathbf{x}', \omega)}{\partial x'_j} dV(\mathbf{x}'), \quad (\text{B.8})$$

Next, we assume the background medium to be homogeneous (it can still be arbitrarily anisotropic). The Green's functions in equation B.8 can be replaced by their asymptotic (high-frequency) representation (Vavryčuk, 2007),

$$G_{mk} = g_m^s g_k^s \bar{G}^s, \quad (\text{B.9})$$

$$G_{ni} = g_n^r g_i^r \bar{G}^r, \quad (\text{B.10})$$

where the superscripts s and r denote the source and receiver wavefields, respectively, \mathbf{g} is the unit polarization vector, and

$$\bar{G}^s = \frac{1}{4\pi\rho V_{gr}^s R^s \sqrt{|K|}} \exp \left[i \frac{\pi}{2} \sigma_0 + i \omega \frac{\mathbf{p}^s}{v^s} \cdot (\mathbf{x}^s - \mathbf{x}') \right], \quad (\text{B.11})$$

$$\bar{G}^r = \frac{1}{4\pi\rho V_{gr}^r R^r \sqrt{|K|}} \exp \left[i \frac{\pi}{2} \sigma_0 + i \omega \frac{\mathbf{p}^r}{v^r} \cdot (\mathbf{x}^r - \mathbf{x}') \right]. \quad (\text{B.12})$$

Here, V_{gr} and R are the group velocity and distance along the ray (the rays connect the scatterer with the source and receiver), K is the Gaussian curvature of the slowness surface, σ_0 is a function of K (Vavryčuk, 2007), \mathbf{p} is the unit slowness vector, and v is the phase velocity.

In the WKBJ approximation (e.g., Aki and Richards, 2002), the spatial derivatives are evaluated only for the rapidly varying terms of the Greens's function (i.e., the exponents in equations B.11 and B.12). Substituting equations B.9–B.12 into equation B.8 yields the following expression for the perturbed wavefield:

$$\delta u_n(\mathbf{x}_r, \omega) = \int_{V(\mathbf{x}')} f_m(\mathbf{x}_s, \omega) \mathcal{A}(\omega) p_l^s p_j^r g_k^s g_i^r \delta c_{ijkl} dV(\mathbf{x}'), \quad (\text{B.13})$$

where

$$\mathcal{A}(\omega) = g_m^s g_n^r \bar{G}^s \bar{G}^r \frac{\omega^2}{v^s v^r}. \quad (\text{B.14})$$

The “radiation pattern” Ω for a model parameterized in terms of the stiffnesses is obtained as the amplitude of the kernel (Alkhalifah and Plessix, 2014) in equation B.13 (i.e., the coefficient multiplied with δc_{ijkl}):

$$\Omega = p_l^s p_j^r g_k^s g_i^r. \quad (\text{B.15})$$

This is a general expression for an arbitrarily anisotropic scatterer embedded in a homogeneous anisotropic background.

Next, we assume the background to be isotropic, and the scatterer to be defined by the stiffness coefficients corresponding to the P- and SV-waves in VTI media (i.e., C_{11} , C_{13} , C_{33} , and C_{55}). Equations A.18–A.21, allow us to calculate the total differential for each stiffness element C_{ij} with respect to the independent variables (V_{P0} , V_{S0} , V_{nm0} , and V_{hor}) and substitute them into equation B.13. We can thus obtain the perturbation for each velocity (V_{P0} , V_{S0} , V_{nm0} , and V_{hor}). Since the background medium is isotropic, the background velocities V_{nm0} , V_{hor} , and V_{P0} are equal, and the unit polarization vectors are parallel (P-waves) or perpendicular (SV-waves) to the corresponding group-velocity vector. For the P-wavefield, the 2D radiation patterns (for parameterization I) in the vertical plane take the form:

$$\Omega^P(V_{P0}) = 2 \rho V_{P0} [2 (p_3^s)^2 (p_3^r)^2 + (p_3^s)^2 (p_1^r)^2 + (p_1^s)^2 (p_3^r)^2], \quad (\text{B.16})$$

$$\Omega^P(V_{S0}) = 8 \rho V_{S0} [2 p_1^s p_3^s p_1^r p_3^r - (p_3^s)^2 (p_1^r)^2 - (p_1^s)^2 (p_3^r)^2], \quad (\text{B.17})$$

$$\Omega^P(V_{\text{nm0}}) = 2 \rho V_{P0} (p_3^s)^2 (p_1^r)^2 + (p_1^s)^2 (p_3^r)^2, \quad (\text{B.18})$$

$$\Omega^P(V_{\text{hor}}) = 4 \rho V_{P0} (p_1^s)^2 (p_1^r)^2. \quad (\text{B.19})$$

The patterns for the S-wavefield are:

$$\Omega^S(V_{P0}) = 0, \quad (\text{B.20})$$

$$\Omega^S(V_{S0}) = 4 \rho V_{S0} [(p_1^s p_1^r + p_3^s p_3^r)^2 - (p_1^s p_3^r - p_3^s p_1^r)^2], \quad (\text{B.21})$$

$$\Omega^S(V_{\text{nmo}}) = -4 \rho V_{P0} p_1^s p_3^s p_1^r p_3^r, \quad (\text{B.22})$$

$$\Omega^S(V_{\text{hor}}) = 4 \rho V_{P0} p_1^s p_3^s p_1^r p_3^r. \quad (\text{B.23})$$

For transmitted waves, the incident and scattering angles are the same, and the components of the unit slowness and polarization vectors for P-waves become:

$$p_s^1 = g_s^1 = -\sin \theta, \quad (\text{B.24})$$

$$p_s^3 = g_s^3 = \cos \theta, \quad (\text{B.25})$$

$$p_r^1 = g_r^1 = \sin \theta, \quad (\text{B.26})$$

$$p_r^3 = g_r^3 = -\cos \theta, \quad (\text{B.27})$$

where θ is the phase angle with the (vertical) symmetry axis. For SV-waves, the corresponding expressions are:

$$p_s^1 = -g_s^3 = -\sin \theta, \quad (\text{B.28})$$

$$p_s^3 = g_s^1 = \cos \theta, \quad (\text{B.29})$$

$$p_r^1 = g_r^3 = \sin \theta, \quad (\text{B.30})$$

$$p_r^3 = -g_r^1 = -\cos \theta. \quad (\text{B.31})$$

The final expressions for the P- and S-wave radiation patterns are given in the main text. The radiation patterns for parameterization II [$\ln(1/V_{P0}^2)$, $\ln 1/V_{S0}^2$, $1 + 2\epsilon$, and $1 + 2\delta$] are obtained in a similar manner.

APPENDIX C - GRADIENTS FOR DIFFERENT PARAMETERIZATIONS

The gradient of the objective function with respect to the stiffness coefficient c_{ijkl} is given in equation 4.2. Expressing the stiffnesses in terms of chosen model parameters m_n makes it possible to obtain the gradients with respect to m_n from equation 4.3. Kamath and Tsvankin (2016) derive the following gradients for VTI media with respect to the velocities V_{P0} , V_{S0} , V_{nmo} , and V_{hor} :

$$\frac{\partial \mathcal{F}}{\partial V_{P0}} = -2\rho V_{P0} \int_0^T \left[\frac{\partial \psi_3}{\partial x_3} \frac{\partial u_3}{\partial x_3} + \frac{f}{2} \left(\frac{\partial \psi_1}{\partial x_1} \frac{\partial u_3}{\partial x_3} + \frac{\partial \psi_3}{\partial x_3} \frac{\partial u_1}{\partial x_1} \right) \right] dt, \quad (\text{C.1})$$

$$\begin{aligned} \frac{\partial \mathcal{F}}{\partial V_{S0}} = 2\rho V_{S0} \int_0^T \left\{ \left[1 + \frac{f}{2} + \frac{1}{2f} \right] \left(\frac{\partial \psi_1}{\partial x_1} \frac{\partial u_3}{\partial x_3} + \frac{\partial \psi_3}{\partial x_3} \frac{\partial u_1}{\partial x_1} \right) \right. \\ \left. - \left(\frac{\partial \psi_1}{\partial x_3} + \frac{\partial \psi_3}{\partial x_1} \right) \left(\frac{\partial u_1}{\partial x_3} + \frac{\partial u_3}{\partial x_1} \right) \right\} dt, \end{aligned} \quad (\text{C.2})$$

$$\frac{\partial \mathcal{F}}{\partial V_{\text{nmo}}} = -\rho V_{\text{nmo}} \int_0^T \frac{1}{f} \left(\frac{\partial \psi_1}{\partial x_1} \frac{\partial u_3}{\partial x_3} + \frac{\partial \psi_3}{\partial x_3} \frac{\partial u_1}{\partial x_1} \right) dt, \quad (\text{C.3})$$

$$\frac{\partial \mathcal{F}}{\partial V_{\text{hor}}} = -2\rho V_{\text{hor}} \int_0^T \frac{\partial \psi_1}{\partial x_1} \frac{\partial u_1}{\partial x_1} dt, \quad (\text{C.4})$$

where

$$f \equiv \sqrt{\frac{V_{\text{nmo}}^2 - V_{S0}^2}{V_{P0}^2 - V_{S0}^2}}. \quad (\text{C.5})$$

The second parameterization is defined as follows:

$$m_1 = \frac{V_{\text{nmo}}^2}{V_{\text{nmo},i}^2}, \quad (\text{C.6})$$

$$m_2 = \frac{V_{S0}^2}{V_{S0,i}^2}, \quad (\text{C.7})$$

$$m_3 = 1 + 2\eta, \quad (\text{C.8})$$

$$m_4 = 1 + 2\delta, \quad (\text{C.9})$$

where the subscript i in equations C.6 and C.7 denotes the initial parameters. The gradients for parameterization II are:

$$\begin{aligned} \frac{\partial \mathcal{F}}{\partial m_1} = & -\rho V_{\text{nmo},i}^2 \int_0^T \left[(1 + 2\eta) \frac{\partial \psi_1}{\partial x_1} \frac{\partial u_1}{\partial x_1} + \frac{1}{1 + 2\delta} \frac{\partial \psi_3}{\partial x_3} \frac{\partial u_3}{\partial x_3} \right. \\ & \left. + \frac{1}{2} \left(\frac{f}{1 + 2\delta} + \frac{1}{2f} \right) \left(\frac{\partial \psi_3}{\partial x_3} \frac{\partial u_1}{\partial x_1} + \frac{\partial \psi_1}{\partial x_1} \frac{\partial u_3}{\partial x_3} \right) \right] dt, \end{aligned} \quad (\text{C.10})$$

$$\begin{aligned} \frac{\partial \mathcal{F}}{\partial m_2} = & -\rho V_{S0,i}^2 \int_0^T \left[\left(\frac{\partial \psi_1}{\partial x_3} + \frac{\partial \psi_3}{\partial x_1} \right) \left(\frac{\partial u_1}{\partial x_3} + \frac{\partial u_3}{\partial x_1} \right) \right. \\ & \left. - \left(\frac{f}{2} + \frac{1}{2f} + 1 \right) \left(\frac{\partial \psi_3}{\partial x_3} \frac{\partial u_1}{\partial x_1} + \frac{\partial \psi_1}{\partial x_1} \frac{\partial u_3}{\partial x_3} \right) \right] dt, \end{aligned} \quad (\text{C.11})$$

$$\frac{\partial \mathcal{F}}{\partial m_3} = -\rho V_{\text{nmo}}^2 \int_0^T \frac{\partial \psi_1}{\partial x_1} \frac{\partial u_1}{\partial x_1} dt, \quad (\text{C.12})$$

$$\frac{\partial \mathcal{F}}{\partial m_4} = \frac{\rho V_{\text{nmo}}^2}{(1 + 2\delta)^2} \int_0^T \left[\frac{\partial \psi_3}{\partial x_3} \frac{\partial u_3}{\partial x_3} + \frac{f}{2} \left(\frac{\partial \psi_3}{\partial x_3} \frac{\partial u_1}{\partial x_1} + \frac{\partial \psi_1}{\partial x_1} \frac{\partial u_3}{\partial x_3} \right) \right] dt. \quad (\text{C.13})$$

For parameterization III,

$$m_1 = \frac{V_{\text{hor}}^2}{V_{\text{hor},i}^2}, \quad (\text{C.14})$$

$$m_2 = \frac{V_{S0}^2}{V_{S0,i}^2}, \quad (\text{C.15})$$

$$m_3 = 1 + 2\eta, \quad (\text{C.16})$$

$$m_4 = 1 + 2\epsilon. \quad (\text{C.17})$$

The gradients of the objective function are:

$$\begin{aligned} \frac{\partial \mathcal{F}}{\partial m_1} = & -\rho V_{\text{hor},i}^2 \int_0^T \left[\frac{\partial \psi_1}{\partial x_1} \frac{\partial u_1}{\partial x_1} + \frac{1}{1+2\epsilon} \frac{\partial \psi_3}{\partial x_3} \frac{\partial u_3}{\partial x_3} \right. \\ & \left. + \frac{1}{2} \left(\frac{f}{1+2\epsilon} + \frac{1}{f(1+2\eta)} \right) \left(\frac{\partial \psi_3}{\partial x_3} \frac{\partial u_1}{\partial x_1} + \frac{\partial \psi_1}{\partial x_1} \frac{\partial u_3}{\partial x_3} \right) \right] dt, \end{aligned} \quad (\text{C.18})$$

$$\begin{aligned} \frac{\partial \mathcal{F}}{\partial m_2} = & -\rho V_{S0,i}^2 \int_0^T \left[\left(\frac{\partial \psi_1}{\partial x_3} + \frac{\partial \psi_3}{\partial x_1} \right) \left(\frac{\partial u_1}{\partial x_3} + \frac{\partial u_3}{\partial x_1} \right) \right. \\ & \left. - \left(\frac{f}{2} + \frac{1}{2f} + 1 \right) \left(\frac{\partial \psi_3}{\partial x_3} \frac{\partial u_1}{\partial x_1} + \frac{\partial \psi_1}{\partial x_1} \frac{\partial u_3}{\partial x_3} \right) \right] dt, \end{aligned} \quad (\text{C.19})$$

$$\frac{\partial \mathcal{F}}{\partial m_3} = \frac{\rho V_{\text{hor}}^2}{2f(1+2\eta)^2} \int_0^T \left(\frac{\partial \psi_3}{\partial x_3} \frac{\partial u_1}{\partial x_1} + \frac{\partial \psi_1}{\partial x_1} \frac{\partial u_3}{\partial x_3} \right) dt, \quad (\text{C.20})$$

$$\frac{\partial \mathcal{F}}{\partial m_4} = \frac{\rho V_{\text{hor}}^2}{(1+2\epsilon)^2} \int_0^T \left[\frac{\partial \psi_3}{\partial x_3} \frac{\partial u_3}{\partial x_3} + \frac{f}{2} \left(\frac{\partial \psi_3}{\partial x_3} \frac{\partial u_1}{\partial x_1} + \frac{\partial \psi_1}{\partial x_1} \frac{\partial u_3}{\partial x_3} \right) \right] dt. \quad (\text{C.21})$$

APPENDIX D - RADIATION PATTERNS FOR DIFFERENT PARAMETERIZATIONS

Kamath and Tsvankin (2016) derive radiation patterns for the stiffness coefficients of an anisotropic inclusion (scatterer) embedded in a homogeneous anisotropic background. To compute the radiation patterns for other model parameterizations considered here, the background is assumed to be isotropic. The P-wave radiation patterns (normalized by $2\rho V_{P0}$) for parameterization I are:

$$\Omega^P(V_{P0}) = \cos^2(\theta/2), \quad (\text{D.1})$$

$$\Omega^P(V_{S0}) = 2 \frac{V_{S0}}{V_{P0}} \sin^2 \theta, \quad (\text{D.2})$$

$$\Omega^P(V_{\text{nmo}}) = \frac{1}{4} \sin^2 \theta, \quad (\text{D.3})$$

$$\Omega^P(V_{\text{hor}}) = \sin^4(\theta/2), \quad (\text{D.4})$$

where θ is the opening angle. The patterns for the scattered SV-wave (normalized by $2\rho V_{S0}$) are:

$$\Omega^S(V_{P0}) = 0, \quad (\text{D.5})$$

$$\Omega^S(V_{S0}) = \cos 2\theta, \quad (\text{D.6})$$

$$\Omega^S(V_{\text{nmo}}) = \frac{V_{P0}}{4V_{S0}} \sin^2 \theta, \quad (\text{D.7})$$

$$\Omega^S(V_{\text{hor}}) = \frac{V_{P0}}{4V_{S0}} \sin^2 \theta, \quad (\text{D.8})$$

For parameterization II, the background P-wave NMO velocity V_{nmo} and the SV-wave vertical velocity V_{S0} in the background are assumed to be equal to the corresponding initial velocities, $V_{\text{nmo},i}$ and $V_{S0,i}$. Because the background is taken assumed to be isotropic, $V_{\text{nmo}} = V_{P0}$. The P-wave radiation pattern (normalized by ρV_{P0}^2) for this parameterization is:

$$\Omega^P \left(\frac{V_{\text{nmo}}^2}{V_{\text{nmo},i}^2} \right) = 1, \quad (\text{D.9})$$

$$\Omega^P \left(\frac{V_{S0}^2}{V_{S0,i}^2} \right) = 2 \left(\frac{V_{S0}}{V_{P0}} \right)^2 \sin^2 \theta, \quad (\text{D.10})$$

$$\Omega^P(1 + 2\eta) = \sin^4(\theta/2), \quad (\text{D.11})$$

$$\Omega^P(1 + 2\delta) = \cos^2(\theta/2). \quad (\text{D.12})$$

The patterns for the scattered SV-wave (normalized by ρV_{S0}^2) are:

$$\Omega^S \left(\frac{V_{\text{nmno}}^2}{V_{\text{nmno},i}^2} \right) = 0, \quad (\text{D.13})$$

$$\Omega^S \left(\frac{V_{S0}^2}{V_{S0,i}^2} \right) = \cos 2\theta, \quad (\text{D.14})$$

$$\Omega^S(1 + 2\eta) = \frac{V_{P0}^2}{4V_{S0}^2} \sin^2 \theta, \quad (\text{D.15})$$

$$\Omega^S(1 + 2\delta) = 0. \quad (\text{D.16})$$

The velocities V_{hor} and V_{S0} in parameterization III are again set equal to the corresponding initial values. In addition, the assumption of isotropic background makes V_{hor} equal to V_{P0} . The P-wave radiation patterns then take the form:

$$\Omega^P \left(\frac{V_{\text{hor}}^2}{V_{\text{hor},i}^2} \right) = 1, \quad (\text{D.17})$$

$$\Omega^P \left(\frac{V_{S0}^2}{V_{S0,i}^2} \right) = 2 \left(\frac{V_{S0}}{V_{P0}} \right)^2 \sin^2 \theta, \quad (\text{D.18})$$

$$\Omega^P(1 + 2\eta) = \frac{1}{4} \sin^2 \theta, \quad (\text{D.19})$$

$$\Omega^P(1 + 2\epsilon) = \cos^2(\theta/2). \quad (\text{D.20})$$

The patterns for the scattered SV-wave (normalized by ρV_{S0}^2) are:

$$\Omega^S \left(\frac{V_{\text{hor}}^2}{V_{\text{hor},i}^2} \right) = 0, \quad (\text{D.21})$$

$$\Omega^S \left(\frac{V_{S0}^2}{V_{S0,i}^2} \right) = \cos 2\theta, \quad (\text{D.22})$$

$$\Omega^S(1 + 2\eta) = \frac{V_{P0}^2}{4V_{S0}^2} \sin^2 \theta, \quad (\text{D.23})$$

$$\Omega^S(1 + 2\epsilon) = 0. \quad (\text{D.24})$$